

Georgia Tsirimokou • Costas Psychalinos
Ahmed Elwakil

Design of CMOS Analog Integrated Fractional-Order Circuits

Applications in Medicine and Biology

 Springer

Georgia Tsirimokou
Physics Department
Electronics Laboratory
University of Patras
Rio Patras, Greece

Costas Psychalinos
Physics Department
Electronics Laboratory
University of Patras
Rio Patras, Greece

Ahmed Elwakil
Department of Electrical
and Computer Engineering
University of Sharjah
Sharjah, United Arab Emirates

Nanoelectronics Integrated
Systems Center (NISC)
Nile University
Cairo, Egypt

ISSN 2191-8112 ISSN 2191-8120 (electronic)
SpringerBriefs in Electrical and Computer Engineering
ISBN 978-3-319-55632-1 ISBN 978-3-319-55633-8 (eBook)
DOI 10.1007/978-3-319-55633-8

Library of Congress Control Number: 2017935037

© The Author(s) 2017

This Springer imprint is published by Springer Nature
The registered company is Springer International Publishing AG
The registered company address is: Gewerbestrasse 11, 6330 Cham, Switzerland

Preface

It is known that many dynamic systems in our world can be better described by differential equations of a non-integer-order, i.e., they behave like non-integer-order (fractional-order) systems. Such systems can be found not only in electronics and signal processing, but also in thermodynamics, biology, chemistry, medicine, mechanics, control theory, nanotechnologies, finances, etc. Thus, fractional-order systems are an emerging area of multidisciplinary research labeled even as the “twenty-first century systems.” Electronic engineers are very interested in applying the concept of fractional calculus. It is motivated mainly by the interdisciplinary nature of this research and possibility to obtain qualitatively new circuit solutions that can provide characteristics not available at integer-order systems. For example, the capability for stepless control of the slope of frequency characteristics in fractional-order filters in comparison with the corresponding integer-order filters is an attractive feature. Fractional-order impedance circuits are also very promising in modeling electrical properties of biological materials, tissues, or cells. Oscillators of fractional-order provide possibility of obtaining higher oscillation frequencies compared to the integer-order counterparts with the same values of passive element parameters offering arbitrary phase shift between output signals.

This book deals with the design and realization of analog fractional-order circuits, which offer the following benefits: (i) capability for on-chip implementation, (ii) capability for low-voltage operation, and (iii) electronic adjustment of their characteristics. Applications of fractional-order circuits, including: a preprocessing stage suitable for the implementation of the Pan-Tompkins algorithm for detecting the QRS complexes of an electrocardiogram (ECG), a fully tunable implementation of the Cole-Cole model used for the modeling of biological tissues, and a simple non-impedance based measuring technique for super-capacitors. A part of the material presented in this book, originates from the work done by Georgia Tsirimokou for her Ph.D. at University of Patras, Greece. It includes details and measurement results for each research project, supported by Grant E.029 from the Research Committee of the University of Patras (Programme K. Karatheodori).

Rio Patras, Greece
Rio Patras, Greece
Sharjah, UAE
Cairo, Egypt

Georgia Tsirimokou
Costas Psychalinos
Ahmed Elwakil

Contents

1	Introduction	1
1.1	Fractional Calculus	1
1.2	Literature Overview	6
1.3	Book Objectives	8
	References	10
2	Procedure for Designing Fractional-Order Filters	13
2.1	Introduction	13
2.2	Fractional-Order Generalized Filters (Order α)	14
2.2.1	Fractional-Order Differentiator	14
2.2.2	Fractional-Order Integrator	15
2.3	Fractional-Order Generalized Filters (Order α)	16
2.3.1	Fractional-Order Low-Pass Filter (FLPF)	17
2.3.2	Fractional-Order High-Pass Filter (FHPF)	17
2.3.3	Fractional-Order Band-Pass Filter (FBPF)	18
2.3.4	Fractional-Order All-Pass Filter (FAPF)	19
2.3.5	Design Equations for Generalized Filters of Order α	20
2.4	Fractional-Order Generalized Filters (Order $1 + \alpha$)	22
2.4.1	Fractional-Order Low-Pass Filter (FLPF)	22
2.4.2	Fractional-Order High-Pass Filter (FHPF)	24
2.4.3	Fractional-Order Band-Pass Filter (FBPF)	25
2.4.4	Fractional-Order Band-Stop Filter (FBSF)	26
2.4.5	Design Equations for Generalized Filters of Order $1 + \alpha$	26
2.5	Fractional-Order Generalized Filters (Order $\alpha + \beta$)	28
2.5.1	Fractional-Order Low-Pass Filter (FLPF)	29
2.5.2	Fractional-Order High-Pass Filter (FHPF)	30
2.5.3	Fractional-Order Band-Pass Filter (FBPF)	30
2.5.4	Fractional-Order Band-Stop Filter (FBSF)	31

2.5.5	Design Equations for Generalized Filters of Order $\alpha + \beta$	32
2.6	Fractional-Order Filters of Order $n + \alpha$	35
2.6.1	Design Equations for Generalized Filters of Order $n + \alpha$	36
2.7	Summary	38
	References	39
3	Current-Mode Fractional-Order Filters	41
3.1	Introduction	41
3.2	Basic Building Blocks	41
3.3	Fractional-Order Filters with Large Time-Constant	46
3.4	Simulation and Comparison Results	49
3.4.1	First-Order Filter Using Current Mirrors with Large Time-Constants	49
3.4.2	Fractional-Order Circuits Using Current Mirrors with Large Time-Constants	50
3.5	Summary	53
	References	54
4	Voltage-Mode Fractional-Order Filters	55
4.1	Introduction	55
4.2	Basic Building Blocks	55
4.3	Fractional-Order Generalized Filters	56
4.4	Simulation Results	58
4.5	Summary	62
	References	62
5	Emulation of Fractional-Order Capacitors (CPEs) and Inductors (FOIs)	65
5.1	Introduction	65
5.2	Proposed Emulation Scheme for Voltage Excited CPE and FOI	66
5.3	Proposed Emulation Scheme for Current Excited CPE and FOI	71
5.4	Chip Fabrication and Experimental Results	72
5.4.1	Effects of Variation of the External Capacitors of the Chip	74
5.4.2	Effects of Variation of the Bias Current of the Chip	74
5.4.3	Effects of Variation of both the Bias Current (I_o) and External Capacitors (C_{ext}) of the Chip	74
5.5	Fractional-Order Resonators Using Emulated CPEs and FOIs	80
5.6	Summary	84
	References	85

6	Applications of Fractional-Order Circuits	87
6.1	Introduction	87
6.2	A Preprocessing Stage Suitable for Implementation of the Pan-Tompkins Algorithm	88
6.3	A fully Tunable Implementation of the Cole-Cole Model	96
6.4	Simple Non-impedance-Based Measuring Technique for Supercapacitors	100
6.5	Design and Evaluation of a Fractional-Order Oscillator	105
	References	111
7	Conclusions and Motivation for Future Work	113
7.1	Conclusions	113
7.2	Motivation for Future Work	114

Chapter 1

Introduction

1.1 Fractional Calculus

Fractional calculus is three centuries old as the conventional calculus and consist a super set of integer-order calculus, which has the potential to accomplish what integer-order calculus cannot. Its origins dating back to a correspondence from 1695 between Leibnitz and L'Hôpital, with L'Hôpital inquiring about Leibnitz notation for the n -th derivative of a function $d^n y/dx^n$, i.e. what would be the result if $n = 1/2$. The reply from Leibnitz, "It will lead to a paradox, a paradox from which one day useful consequences will be drawn, because there are no useless paradoxes", was the motivation for fractional calculus to be born. Fractional calculus does not mean the calculus of fractions, nor does it mean a fraction of any calculus differentiation, integration or calculus of variations. The fractional calculus is a name of theory of integrations and derivatives of arbitrary order, which unify and generalize the notation of integer-order differentiation and n -fold integration. The beauty of this subject is that fractional derivatives and integrals translate better the reality of nature! This feature is an efficient tool, offering the capability of having available a language of nature, which can be used to talk with.

Despite the fact that for the past three centuries this field was of interest to mathematicians, only the last few years did this appear in several applied fields of science such as materials theory, diffusion theory, engineering, biomedicine, economics, control theory, electromagnetic, robotics, and signal and image processing [1–6]. Over all these last years fractional order systems or systems containing fractional derivatives and integrals have been studied in engineering and science area. A vast number of model make use of the fractional-order derivatives that exist in the literature. However, there are many of these definitions in the literature nowadays, but few of them are commonly used, including Riemann-Liouville, Caputo, Weyl, Jumarie, Hadamard, Davison and Essex, Riesz, Erdelyi-Kober, and Coimbra. There are two main approaches for defining a fractional derivative.

The first considers differentiation and integration as limits of finite differences. The Grunwald-Letnikov definition follows this approach. The other approach generalizes a convolution type representation of repeated integration. The Riemann-Liouville and Caputo definitions employ this approach. Riemann-Liouville and Caputo fractional derivatives are fundamentally related to fractional integration operators and, hence, are the most popular.

The Caputo derivative is very useful when dealing with real-world problems, because it allows traditional initial and boundary conditions to be included in the formulation of the problem and, in addition, the derivative of a constant is zero [7]. As a result, the aforementioned definition will be used within this work, the expression of which is given as

$${}_0D_t^\alpha f(t) = \frac{1}{\Gamma(n-\alpha)} \int_0^t \frac{f^{(n)}(\tau)}{(t-\tau)^{\alpha+1-n}} d\tau \quad (1.1)$$

where $n-1 \leq \alpha \leq n$ and $\Gamma(\cdot)$ is the gamma function.

In the design and analysis of electronic circuits, the Laplace transform is a very useful tool, transforming the circuit from the time-domain into the frequency domain. With this transformation, the analysis of circuits can be algebraically conducted rather than by solving differential equations. Thus, applying the Laplace transform to (1.1) yields

$$\mathcal{L}\{{}_0D_t^\alpha f(t)\} = s^\alpha F(s) - \sum_{k=0}^{n-1} s^{\alpha-k-1} f(0)^{(k)} \quad (1.2)$$

where $f(0)$ is the initial condition.

The variable s^α is the fractional Laplacian operator, which allows for the design and analysis of systems using concepts from fractional calculus without having to solve time-domain complicated representations.

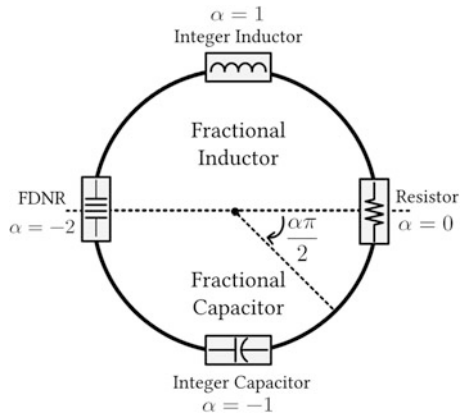
In the analog domain, such an operation using the aforementioned definitions can be called as *fractance device*, which is an electrical element and exhibits fractional-order impedance properties. The expression for impedance function of a fractance device is given by

$$Z(s) = \kappa s^\alpha = (\kappa\omega)^\alpha e^{j\frac{\alpha\pi}{2}} \quad (1.3)$$

where κ is a constant and α is a fractional-order.

Depending upon the values of α , the behavior of the element changes from inductor to capacitor. In the range $0 < \alpha < 2$, this element may generally be considered to represent a fractional-order inductor, while for the range $-2 < \alpha < 0$, it may be considered to represent a fractional-order capacitor. For the special case of $\alpha = 1$ this element represents an inductor while for $\alpha = -1$ it represents a capacitor.

Fig. 1.1 Classification diagram of fractional-order elements



At $\alpha = -2$, it represents the well-known frequency-dependent negative resistor (FDNR). A typical diagram for classifying these elements is depicted in Fig. 1.1.

However, there are no commercial available fractance devices for the physical realization of fractional-order circuits and systems. Therefore, until commercial fractance devices become available to physically realize circuits that make use of the advantages of s^α , integer-order approximations have to be used. There are many methods used to create an approximation of s^α that include continued fraction expansions (CFEs) as well as rational approximation methods [2]. These methods present a large array of approximations with varying accuracy, which depends on the order of the approximation. It is known that the continued fraction expansion for $(1+x)^\alpha$ is given as [8]

$$(1+x)^\alpha = \frac{1}{1-} \frac{\alpha x}{1+} \frac{(1+\alpha)x}{2+} \frac{(1-\alpha)x}{3+} \frac{(2+\alpha)x}{2+} \frac{(2-\alpha)x}{5+\dots} \quad (1.4)$$

The above expression converges in the finite complex s -plane, along with the negative real axis from $x = -\infty$ to $x = -1$. Substituting $x = s-1$ and taking up to 10 number of terms in Eq. (1.4), the rational approximations obtained for s^α are presented in Table 1.1. In order to obtain the rational approximation of $1/s^\alpha$, the expressions have to be simply inverted or the variable has to be set to $\alpha \rightarrow -\alpha$. Higher-order rational approximations can be obtained by increasing the number of terms in Eq. (1.4). Thus, the general form of the obtained rational approximation of the variable s^α around a specific frequency ω_0 is that given in (1.5)

$$(\tau s)^\alpha \cong \frac{\alpha_0(\tau s)^n + \alpha_1(\tau s)^{n-1} + \dots + \alpha_{n-1}(\tau s) + \alpha_n}{\alpha_n(\tau s)^n + \alpha_{n-1}(\tau s)^{n-1} + \dots + \alpha_1(\tau s) + \alpha_0} \quad (1.5)$$

where n is the order of the approximation and $(\omega_0 = 1/\tau)$ the center frequency where the approximation is performed.

Table 1.1 Rational approximation for $(\tau s)^\alpha$

No. of terms	Rational approximation for α	Design equations of coefficients
2	$\frac{\alpha_0(\tau s) + \alpha_1}{\alpha_1(\tau s) + \alpha_0}$	$\alpha_0 = (1 - \alpha)\alpha_1 = (1 + \alpha)$
4	$\frac{\alpha_0(\tau s)^2 + \alpha_1(\tau s) + \alpha_2}{\alpha_2(\tau s)^2 + \alpha_1(\tau s) + \alpha_0}$	$\alpha_0 = (\alpha^2 + 3\alpha + 2)$ $\alpha_1 = (8 - 2\alpha^2)$ $\alpha_2 = (\alpha^2 - 3\alpha + 2)$
6	$\frac{\alpha_0(\tau s)^3 + \alpha_1(\tau s)^2 + \alpha_2(\tau s) + \alpha_3}{\alpha_3(\tau s)^3 + \alpha_2(\tau s)^2 + \alpha_1(\tau s) + \alpha_0}$	$\alpha_0 = (\alpha^3 + 6\alpha^2 + 11\alpha + 6)$ $\alpha_1 = (-3\alpha^3 - 6\alpha^2 + 27\alpha + 54)$ $\alpha_2 = (3\alpha^3 - 6\alpha^2 - 27\alpha + 54)$ $\alpha_3 = (-\alpha^3 + 6\alpha^2 - 11\alpha + 6)$
8	$\frac{\alpha_0(\tau s)^4 + \alpha_1(\tau s)^3 + \alpha_2(\tau s)^2 + \alpha_3(\tau s) + \alpha_4}{\alpha_4(\tau s)^4 + \alpha_3(\tau s)^3 + \alpha_2(\tau s)^2 + \alpha_1(\tau s) + \alpha_0}$	$\alpha_0 = (\alpha^4 + 10\alpha^3 + 35\alpha^2 + 50\alpha + 24)$ $\alpha_1 = \left(\begin{array}{c} -4\alpha^4 - 20\alpha^3 + 40\alpha^2 \\ +320\alpha + 384 \end{array} \right)$ $\alpha_2 = (6\alpha^4 - 150\alpha^2 + 864)$ $\alpha_3 = \left(\begin{array}{c} -4\alpha^4 + 20\alpha^3 + 40\alpha^2 \\ -320\alpha + 384 \end{array} \right)$ $\alpha_4 = (\alpha^4 - 10\alpha^3 + 35\alpha^2 - 50\alpha + 24)$
10	$\frac{\alpha_0(\tau s)^5 + \alpha_1(\tau s)^4 + \alpha_2(\tau s)^3 + \alpha_3(\tau s)^2 + \alpha_4(\tau s) + \alpha_5}{\alpha_5(\tau s)^5 + \alpha_4(\tau s)^4 + \alpha_3(\tau s)^3 + \alpha_2(\tau s)^2 + \alpha_1(\tau s) + \alpha_0}$	$\alpha_0 = \left(\begin{array}{c} -\alpha^5 - 15\alpha^4 - 85\alpha^3 \\ -225\alpha^2 - 274\alpha - 120 \end{array} \right)$ $\alpha_1 = \left(\begin{array}{c} 5\alpha^5 + 45\alpha^4 + 5\alpha^3 \\ -1005\alpha^2 - 3250\alpha - 3000 \end{array} \right)$ $\alpha_2 = \left(\begin{array}{c} -10\alpha^5 - 30\alpha^4 + 410\alpha^3 \\ +1230\alpha^2 - 4000\alpha - 12000 \end{array} \right)$ $\alpha_3 = \left(\begin{array}{c} 10\alpha^5 - 30\alpha^4 - 410\alpha^3 \\ +1230\alpha^2 + 4000\alpha - 12000 \end{array} \right)$ $\alpha_4 = \left(\begin{array}{c} -5\alpha^5 + 45\alpha^4 - 5\alpha^3 \\ -1005\alpha^2 + 3250\alpha - 3000 \end{array} \right)$ $\alpha_5 = \left(\begin{array}{c} \alpha^5 - 15\alpha^4 + 85\alpha^3 \\ -225\alpha^2 + 274\alpha - 120 \end{array} \right)$

In terms of circuit complexity and magnitude and phase accuracy, the second-order approximation of variable s^α is an efficient tool for implementing fractional-order circuits. The corresponding expression for approximating variable $(\tau s)^\alpha$ is also given by (1.6) as

$$\begin{aligned}
(\tau s)^\alpha &\cong \frac{(\alpha^2 + 3\alpha + 2)(\tau s)^2 + (8 - 2\alpha^2)(\tau s) + (\alpha^2 - 3\alpha + 2)}{(\alpha^2 - 3\alpha + 2)(\tau s)^2 + (8 - 2\alpha^2)(\tau s) + (\alpha^2 + 3\alpha + 2)} \\
&= \frac{\alpha_0(\tau s)^2 + \alpha_1(\tau s) + \alpha_2}{\alpha_2(\tau s)^2 + \alpha_1(\tau s) + \alpha_0}
\end{aligned} \tag{1.6}$$

where the design equations of coefficients α_i ($i = 0,1,2$) are already defined as

$$\begin{aligned}
\alpha_0 &= (\alpha^2 + 3\alpha + 2) \\
\alpha_1 &= (8 - 2\alpha^2) \\
\alpha_2 &= (\alpha^2 - 3\alpha + 2)
\end{aligned} \tag{1.7}$$

Another approach for obtaining the second-order approximation for s^α is using the continued fraction expansions [9], [10] of the two functions

$$(1 + \tau s)^\alpha \cong \frac{2 + (1 + 2\alpha)(\tau s)}{2 + (1 - 2\alpha)(\tau s)} \tag{1.8}$$

$$\left(1 - \frac{1}{\tau s + 1}\right)^\alpha \cong \frac{(\tau s) + (1 - \alpha)/2}{(\tau s) + (1 + \alpha)/2} \tag{1.9}$$

where (1.8) is the approximation for high frequencies $\omega \gg 1$, and (1.9) the approximation for $\omega \ll 1$.

Noting that the product $(1 + \tau s)^\alpha \cdot \left(1 - \frac{1}{\tau s + 1}\right)^\alpha = (\tau s)^\alpha$, a second-order approximation can therefore be written as shown is (1.10).

$$\begin{aligned}
(\tau s)^\alpha &\cong \frac{2(1 + \alpha)(\tau s)^2 + (5 - \alpha^2)(\tau s) + 2(1 - \alpha)}{2(1 - \alpha)(\tau s)^2 + (5 - \alpha^2)(\tau s) + 2(1 + \alpha)} \\
&= \frac{\alpha_0(\tau s)^2 + \alpha_1(\tau s) + \alpha_2}{\alpha_2(\tau s)^2 + \alpha_1(\tau s) + \alpha_0}
\end{aligned} \tag{1.10}$$

where the design equations of coefficients α_i ($i = 0, 1, 2$) are defined as

$$\begin{aligned}
\alpha_0 &= 2(1 + \alpha) \\
\alpha_1 &= (5 - \alpha^2) \\
\alpha_2 &= 2(1 - \alpha)
\end{aligned} \tag{1.11}$$

Although there are additional methods for obtaining the rational approximations of the variable s^α , such as Carlson's, Matsuda's, and Oustaloup's methods, according to [11], the CFE is an attractive choice in terms of phase and gain error. Thus, the aforementioned procedure of the second-order approximation of the CFE will be adopted in the framework of this work.

1.2 Literature Overview

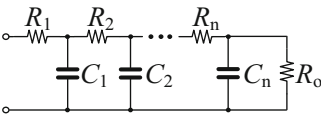
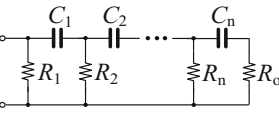
Integrators and differentiators are very useful building blocks for performing signal conditioning in biomedical applications. They are employed for realizing filters, oscillators, and impedance emulators, and in control systems. Fractional-order digital implementations of such circuits have been already published in the literature [12–16]. Significant research effort is going on to develop fractional-order capacitors, also known as constant phase elements (CPEs) as stand-alone two-terminal devices. For example, CPEs have been developed by utilizing electrolytic process [17], fractal structures on silicon [18], by dipping a capacitive type polymer-coated probe in a polarizable medium [19–21], and most recently in [22] using graphene. All the aforementioned solutions are not commercially available and, also, suffer from the benefit of on-line adjustability. Existing techniques for emulating a CPE mostly rely on passive RC trees, the components of which can be obtained by several suitable methods such as the continued fraction expansion [23–26]. Following this approach, a number of fractional-order circuits have been published in the literature [2, 27–34], where various kinds of RC network topologies have been utilized. Another important element for performing fractional-order signal processing is the fractional-order inductor (FOI), which could be easily performed through the combination of a fractional-order capacitor and a generalized impedance converter (GIC) [35]. A summary of design equations for deriving RC networks is given in Table 1.2a, 1.2b, where the Foster and Cauer networks have been utilized. The derived expressions have been obtained taking into account that the impedance/admittance of a CPE using the CFE will be

Table 1.2a A systematic presentation for realizing fractional-order capacitors using RC networks (Foster I, and Foster II)

Network type	Foster I	Foster II
Circuit topology		
Impedance/admittance	$Z(s) = R_0 + \sum_{i=1}^n \frac{1}{s + \frac{1}{R_i C_i}}$	$\frac{Y(s)}{s} = \frac{1}{R_0} + \sum_{i=1}^n \frac{\frac{R_i}{s}}{s + \frac{1}{R_i C_i}}$
General form of partial fraction expansion of (1.12)	$Z(s) = k + \sum_{i=1}^n \frac{r_i}{s - p_i}$	$\frac{Y(s)}{s} = \frac{k}{s} + \sum_{i=1}^n \frac{r_i}{s - p_i}$
Design equations for calculating values R_i , C_i^a	$R_0 = k, C_i = \frac{1}{r_i}, R_i = \frac{1}{C_i p_i }$	$R_0 = \frac{1}{k}, C_i = \frac{1}{r_i}, C_i = \frac{1}{R_i p_i }$

^a k and r_i are constant terms, p_i are the poles of impedance

Table 1.2b A systematic presentation for realizing fractional-order capacitors using RC networks (Cauer I, and Cauer II)

Network type	Cauer I	Cauer II
Circuit topology		
Impedance/admittance	$Z(s) = R_1 + \frac{1}{C_1 s + R_2 + \frac{1}{R_n + C_n s + R_0}}$	$Z(s) = \frac{1}{\frac{1}{R_1} + \frac{1}{C_1 s + R_2 + \frac{1}{R_n + C_n s + R_0}}}$
General form of partial fraction expansion of (1.12)	$Z(s) = q_{r1} + \frac{1}{q_{c1}s + q_{r2} + \frac{1}{q_{rn} + q_{cn}s + q_{r0}}}$	$Z(s) = \frac{1}{q_{r1} + \frac{1}{\frac{s}{q_{c1}} + q_{r2} + \frac{1}{q_{rn} + \frac{q_{cn}}{s} + q_{r0}}}}$
Design equations for calculating values R_i, C_i^a	$R_i = q_{ri} \quad (i = 0, \dots, n)$ $C_j = q_{cj} \quad (j = 1, \dots, n)$	$R_i = 1/q_{ri} \quad (i = 0, \dots, n)$ $C_j = 1/q_{cj} \quad (j = 1, \dots, n)$

^acoefficients q_{ri} ($i = 0, \dots, n$), q_{cj} ($j = 1, \dots, n$) are that obtained from the CFE

$$Z(s) = \frac{1}{C\omega_o} \cdot \frac{\alpha_n s^n + \alpha_{n-1} \omega_o s^{n-1} + \dots + \alpha_1 \omega_o^{n-1} s + \alpha_0 \omega_o^n}{\alpha_0 s^n + \alpha_1 \omega_o s^{n-1} + \dots + \alpha_{n-1} \omega_o^{n-1} s + \alpha_n \omega_o^n} \quad (1.12a)$$

$$Y(s) = C\omega_o \cdot \frac{\alpha_0 s^n + \alpha_1 \omega_o s^{n-1} + \dots + \alpha_{n-1} \omega_o^{n-1} s + \alpha_n \omega_o^n}{\alpha_n s^n + \alpha_{n-1} \omega_o s^{n-1} + \dots + \alpha_1 \omega_o^{n-1} s + \alpha_0 \omega_o^n} \quad (1.12b)$$

Nevertheless, these realizations are problematic when it is desired to change the characteristics of the designed emulator, since all the values of the passive components of the tree have to be changed. Thus, only a fixed approximation for a specific element valid over a center prespecified bandwidth with acceptable magnitude and phase errors is offered. Another significant research effort that has gained a growing research interest is the utilization of fractional-order calculus in filter design. Implementation of fractional-order filters in fully digital form [36–39] offers the advantages of easy design, reliability, programmability, and better noise rejection in comparison with the corresponding analog realizations.

On the other hand, the digital implementation suffers from the high power consumption associated with the required analog-to-digital (A/D) converter.

Analog realizations of fractional-order filters have been already introduced in discrete component form in [12], [21], [28], [32–34], [40–43]. The used active elements were operational amplifiers (op-amps), second-generation current conveyors (CCII), and current feedback operational amplifiers (CFOAs). Because of the employment of passive resistors, an additional automatic tuning circuitry is required for compensating the deviations from the desired frequency response.

Another important drawback is the absence of programmability, making these structures not capable of fulfilling the demand for realizing programmable analog filters. All the above designs offer one type of filter function, and therefore the existence of filter topologies which are capable for implementing various types of filter functions without modifying their core is very important from the design flexibility point of view.

1.3 Book Objectives

The contribution made in this book is that the utilization of the second-order approximation of CFE in order to present a systematic way for describing the design equations of fractional-order generalized transfer functions, offered the capability of designing the following analog integrated implementations for the first time in the literature:

- Fractional-order differentiator/integrator topologies, which offer the following benefits:
 - Capability of being realized using the same topology
 - The frequency characteristics as well as the fractional order α are able to be easily electronically tuned
 - Fully integratable topologies
 - Resistorless realizations
 - Only grounded capacitors are employed
 - Operation in a low-voltage environment
- Fractional-order generalized filters, offering the following characteristics:
 - Capability of realizing different families of filters (i.e., Butterworth, Chebychev, etc.) using the same topology
 - Capability of realizing different types of filters classified through the bandform frequency response (i.e., lowpass, highpass, bandpass, etc.) using the same topology
 - All the above frequency characteristics as well as the fractional order are able to be easily electronically tuned offering design flexibility and programmability
 - Resistorless realizations
 - Only grounded capacitors are employed
 - Operation in a low-voltage environment
- Fully integrated fractional-order (capacitor and inductor) emulators, offering the following attractive benefits:
 - Electronic tuning of the impedance magnitude
 - Electronic tuning of the fractional order
 - Electronic tuning of the bandwidth of operation
 - Resistorless realizations

- Only grounded capacitors are employed
- Operation in a low-voltage environment

The main active cells that are employed are current mirrors, nonlinear transconductance cells (known as S , C cells), and operational transconductance amplifiers (OTAs). As a result, the designer has only to choose the appropriate values of the dc bias currents in order to realize the desired transfer function, and therefore the proposed schemes offer attractive features.

- Also, some interesting applications of the aforementioned designs will be presented, where reasonable characteristics are offered making them attractive candidates for realizing high performance fractional-order systems.
- Finally, simple circuit implementation setups are introduced for characterizing fractional-order elements.

Consequently, the rest of the text of this book is organized as follows:

In Chap. 2, a systematic way of realizing fractional-order differentiator/integrator topologies, as well as fractional-order generalized filters, is introduced. More specifically, fractional-order filters of order α (low-pass, high-pass, band-pass, all-pass), $1 + \alpha$ (low-pass, high-pass, band-pass, band-stop), $\alpha + \beta$ (low-pass, high-pass, band-pass, band-stop), and $n + \alpha$ are presented, where n and α, β are the integer and fractional parts, respectively. The theoretical mathematical background, as well as the design equations obtained using the second-order approximation of CFE, is given in detail. As a result, the appropriate selection of active building blocks that could be used for realizing these topologies is depended on the designer demand.

In Chap. 3, the realization of fractional-order topologies using the current-mode technique is presented. Current-mirror blocks are utilized for performing fractional-order topologies. The realization of fractional-order filters of order $1 + \alpha$ with programmable characteristics are presented, the behavior of which has been evaluated through simulation results. Moreover, fractional-order blocks, including differentiators and lossy and lossless integrators are presented, which are able to be realized using the same structure topology. Filters of order $1 + \alpha$ are also given where current mirror building blocks are utilized for realizing the aforementioned circuits. The performance of the proposed topologies has been evaluated through simulation and comparison results using the Analog Design Environment of the Cadence software.

In Chap. 4, the realization of fractional-order topologies using the voltage mode technique is presented. The basic building block that has been employed for this purpose is an OTA, As a result, fractional-order filters of order α , and $\alpha + \beta$, are realized, where the filter schemes are generalized in the sense that they offer various types of filter functions. The performance of the proposed topologies has been evaluated through simulation and comparison results using the Analog Design Environment of the Cadence software, which proof that they offer reasonable characteristics.

In Chap. 5, a systematic procedure in an algorithmic way for realizing fractional-order capacitor and inductor emulators are introduced for the first time in the

literature. Taking into account the offered benefits of the second-order approximation of the CFE, as well as the utilization of OTAs as active elements, the order, impedance, and bandwidth of operation are able to be electronically tuned through appropriate bias currents. The utilization of the already studied methods for emulating fractional-order capacitors and inductors will be used for fabricating these elements for the first time in the literature. The proposed designs are fabricated in AMS 0.35 μm C35B4C3 CMOS technology, the right operation of which has been verified through experimental results. As design examples, the performance of an $L_{\beta}C_{\alpha}$ parallel resonator as well as a fractional band pass filter of order $\alpha + \beta$ are presented, which proofs that the fabricated designs offer attractive benefits and are able to be utilized in high performance systems.

In Chap. 6, an attractive fractional-order topology capable for handling noisy ECGs is introduced. The realization of this system is performed using the Sinh-Domain technique. The performance of the proposed blocks has been evaluated through the Analog Design Environment of the Cadence software. Taking into account that the characterization of fractional-order elements is in general a difficult, not straight forward, and cost-effective procedure, simple experimental setups for characterizing fractional-order capacitors and supercapacitors are introduced. In addition, fractional-order capacitors are employed in order to emulate biological tissues using the well-known Cole-Cole model. Finally, the design and evaluation of a fractional-order oscillator is realized proving the necessity of fractional calculus especially when compared with the conventional way.

References

1. Ortigueira, M.: An introduction to the fractional continuous-time linear systems: the 21st century systems. *IEEE Circuits Syst. Mag.* **8**(3), 19–26 (2008)
2. Podlubny, I., Petras, I., Vinagre, B., O’Leary, P., Dorcak, L.: Analogue realizations of fractional-order controllers. *Nonlinear Dyn.* **29**(1), 281–296 (2002)
3. Haba, T., Loum, G., Zoueu, J., Ablart, G.: Use of a component with fractional impedance in the realization of an analogical regulator of order $\frac{1}{2}$. *J. Appl. Sci.* **8**(1), 59–67 (2008)
4. Tenreiro-Machado, J.A., Jesus, I.S., Galhano, A., Cunha, J.B.: Fractional order electromagnetics. *Signal Process.* **86**(10), 2637–2644 (2006)
5. Miguel, F., Lima, M., Tenreiro-Machado, J.A., Crisostomo, M.: Experimental signal analysis of robot impacts in a fractional calculus perspective. *J. Adv. Comput. Intell. Intell. Informatics.* **11**(9), 1079–1085 (2007)
6. Ferreira, N.F., Duarte, F., Lima, M., Marcos, M., Machado, J.T.: Application of fractional calculus in the dynamical analysis and control of mechanical manipulators. *Fractional Calculus Appl. Anal.* **11**(1), 91–113 (2008)
7. Caputo, M.: Linear models of dissipation whose Q is almost frequency independent, part II. *Geophys. J. Int.* **13**(5), 529–539 (1967)
8. Khovanskii, A.N.: *The Application of Continued Fractions and Their Generalizations to Problems in Approximation Theory.* Noordhoff, Groningen (1963)
9. Chen, Y., Vinagre, B., Podlubny, I.: Continued fraction expansion approaches to discretizing fractional order derivatives – an expository review. *Nonlinear Dyn.* **38**(1), 155–170 (2004)

10. Chen, Y., Moore, K.: Discretization schemes for fractional-order differentiators and integrators. *IEEE Trans. Circuits Syst. I.* **49**(3), 363–367 (2002)
11. Krishna, B., Reddy, K.: Active and passive realizations of fractance device of order 1/2. *Act. Passive Electron. Compon.* 2008, Article ID 369421, 5 pages (2008)
12. Abdelliche, F., Charef, A.: R-peak detection Using a complex fractional wavelet. In: *Proceedings of the IEEE International Conference on Electrical and Electronics Engineering*, pp. 267–270 (2009)
13. Abdelliche, F., Charef, A., Talbi, M., Benmalek, M.: A fractional wavelet for QRS detection. *IEEE Inf. Commun. Technol.* **1**(2), 1186–1189 (2006)
14. Ferdi, Y., Hebeuval, J., Charef, A., Boucheham, B.: R wave detection using fractional digital differentiation. *ITBMRBM.* **24**(5–6), 273–280 (2003)
15. Goutas, A., Ferdi, Y., Herbeuval, J.P., Boudraa, M., Boucheham, B.: Digital fractional order differentiation-based algorithm for P and T-waves detection and delineation. *Int. Arab. J. Inf. Technol.* **26**(2), 127–132 (2005)
16. Benmalek, M., Charef, A.: Digital fractional order operators for R-wave detection in electrocardiogram signal. *IET Signal Proc.* **3**(5), 381–391 (2009)
17. Jesus, I.S., Machado, J.A.: Development of fractional order capacitors based on electrolytic process. *Nonlinear Dyn.* **56**(1), 45–55 (2009)
18. Haba, T.C., Ablart, G., Camps, T., Olivie, F.: Influence of the electrical parameters on the input impedance of a fractal structure realized on silicon. *Chaos, Solitons Fractals.* **24**(2), 479–490 (2005)
19. Biswas, K., Sen, S., Dutta, P.: Realization of a constant phase element and its performance study in a differentiator circuit. *IEEE Trans. Circuits Syst. II Express Briefs.* **53**(9), 802–806 (2006)
20. Mondal, D., Biswas, K.: Performance study of fractional order integrator using single component fractional order elements. *IET Circuits Devices Syst.* **5**(4), 334–342 (2011)
21. Krishna, M.S., Das, S., Biswas, K., Goswami, B.: Fabrication of a fractional - order capacitor with desired specifications: a study on process identification and characterization. *IEEE Trans. Electron Devices.* **58**(11), 4067–4073 (2011)
22. Elshurafa, A.M., Almadhoun, M.N., Salama, K.N., Alshareef, H.N.: Microscale electrostatic fractional capacitors using reduced graphene oxide percolated polymer composites. *Appl. Phys. Lett.* **102**(23), 232901–232904 (2013)
23. Carlson, G.E., Halijak, C.A.: Approximation of fractional capacitors $(1/s)^{(1/n)}$ by a regular Newton process. *IEEE Trans. Circuit Theory.* **11**(2), 210–213 (1964)
24. Steiglitz, K.: An RC impedance approximation to $s^{-1/2}$. *IEEE Trans. Circuits Syst.* **11**(1), 160–161 (1964)
25. Roy, S.C.D.: On the realization of a constant-argument immittance or fractional operator. *IEEE Trans. Circuits Syst.* **14**(3), 264–274 (1967)
26. Valsa, J., Vlach, J.: RC models of a constant phase element. *Int. J. Circuit Theory Appl.* **41**(1), 59–67 (2013)
27. Ali, A., Radwan, A., Soliman, A.: Fractional order Butterworth filter: active and passive realizations. *IEEE J. Emerging Sel. Top. Circuits Syst.* **3**(3), 346–354 (2013)
28. Freeborn, T.J., Maundy, B.J., Elwakil, A.S.: Approximated fractional-order Chebyshev lowpass filters. *Math. Probl. Eng.* **2015**, 1 (2015)
29. Freeborn, T.J., Elwakil, A.S., Maundy, B.J.: Approximating fractional-order inverse Chebyshev lowpass filters. *Circuits Syst. Signal Process.* **35**(6), 1973–1982 (2016)
30. Maundy, B.J., Elwakil, A.S., Gift, S.: On the realization of multiphase oscillators using fractional-order allpass filters. *Circuits Systems and Signal Processing.* **31**(1), 3–17 (2012)
31. Radwan, A., Soliman, A., Elwakil, A.: First-order filters generalized to the fractional domain. *J. Circuits Syst. Comput.* **17**(1), 55–66 (2008)
32. Radwan, A., Elwakil, A., Soliman, A.: On the generalization of second-order filters to the fractional-order domain. *J. Circuits Syst. Comput.* **18**(2), 361–386 (2009)

33. Radwan, A., Salama, K.: Fractional-order RC and RL circuits. *Circuits Systems and Signal Processing*. **31**, 1901–1915 (2012)
34. Tripathy, M., Mondal, D., Biswas, K., Sen, S.: Experimental studies on realization of fractional inductors and fractional-order bandpass filters. *International Journal of Circuit Theory and Applications*. **43**(9), 1183–1196 (2015)
35. Psychalinos, C., Pal, K., Vlassis, S.: A floating generalized impedance converter with current feedback amplifiers. *Int. J. Electron. Commun.* **62**, 81–85 (2008)
36. Chen, Y.Q., Moore, K.L.: Discretization schemes for fractional-order differentiators and integrators. *IEEE Trans. Circuits Syst. I, Fundam Theory Appl.* **49**(3), 363–367 (2002)
37. Tseng, C.C., Lee, S.L.: Design of fractional order digital differentiator using radial basis function. *IEEE Trans. Circuits Syst. I, Regul. Pap.* **57**(7), 1708–1718 (2010)
38. Das, S., Pan, I.: Fractional-order signal processing: introductory concepts and applications. *Springer Briefs in Applied Sciences and Technology*, Chapter, vol. 2, pp. 13–30 (2012)
39. Freeborn, T.J., Maundy, B.J., Elwakil, A.S.: Field programmable analogue array implementation of fractional step filters. *IET Circuits Devices Syst.* **4**(6), 514–524 (2010)
40. Maundy, B.J., Elwakil, A.S., Freeborn, T.J.: On the practical realization of higher-order filters with fractional stepping. *Signal Process.* **91**(3), 484–491 (2011)
41. Ahmadi, P., Maundy, B.J., Elwakil, A.S., Belostotski, L.: High-quality factor asymmetric-slope band-pass filters: a fractionalorder capacitor approach. *IET Circuits Devices and Systems*. **6**(3), 187–197 (2012)
42. Soltan, A., Radwan, A., Soliman, A.: Fractional-order filter with two fractional elements of dependant orders. *Microelectron. J.* **43**(11), 818–827 (2012)
43. Freeborn, T.J., Maundy, B.J., Elwakil, A.S.: Towards the realization of fractional step filters. In: *Proceedings of the IEEE International Symposium on Circuits and Systems (ISCAS)*, pp. 1037–1040 (2010)

Chapter 2

Procedure for Designing Fractional-Order Filters

2.1 Introduction

Fractional-order differentiation and integration topologies offer attractive features in various interdisciplinary applications. A typical application is the substitution of conventional integer order parts of a system with the fractional-order parts, respectively, where the existence of derivation/integration has a decisive position, and offers important benefits. Also, they are able to be used in order to realize one of the most important circuits in fractional-order theory, which is the fractal device. On the other hand, fractional-order filters, offer more precise control of the attenuation gradient, which is an efficient feature in biomedical engineering. Fractional-order filters, differentiators, and integrators, will be presented in a systematic way that describes the most important features of these structures; realizing such circuits through the utilization of a general form enabling the capability of realizing different kind of circuits by the same topology, which is very important from the flexibility point of view. All the above will be performed through the utilization of the second-order CFE, which is an efficient tool, in terms of accuracy and circuit complexity, and has been described in Chap. 1 in detail. As a consequence, the main benefit of this procedure is that having available the design equations, which are expressed through integer-order functions, the capability of realizing these types of functions utilizing different ways of circuit design could be achieved.

2.2 Fractional-Order Generalized Filters (Order α)

Integrators and differentiators are very useful building blocks for performing signal conditioning in biomedical applications. Also, they are employed for realizing oscillators, impedance emulators, and in control systems. Fractional-order digital implementations of such circuits have been already published in the literature [1–5].

The utilization of the second-order expressions of CFE is an appropriate tool for realizing fractional-order differentiators and integrators in order to approximate the variable $(\tau s)^\alpha$ using the formula given in (2.1). In case that $\alpha = 1$, this transfer function represents a differentiator, while for $\alpha = -1$ an integrator. In the range $(0 < \alpha < 1)$, this element may generally be considered to represent a fractional-order differentiator, while in the range $(-1 < \alpha < 0)$, a fractional-order integrator.

$$(\tau s)^\alpha = \frac{\alpha_0(\tau s)^2 + \alpha_1(\tau s) + \alpha_2}{\alpha_2(\tau s)^2 + \alpha_1(\tau s) + \alpha_0} \quad (2.1)$$

2.2.1 Fractional-Order Differentiator

The transfer function, as well as the magnitude response of an integer-order differentiator is given by the formula $H(s) = \tau s$, and $H(\omega) = \omega/\omega_0$, respectively. The unity gain frequency is $\omega_0 = 1/\tau$, where τ is the corresponding time-constant. In addition the phase response is constant and equal to $\pi/2$. Thus, the transfer function of a fractional-order differentiator will be given by (2.2) as

$$H(s) = (\tau s)^\alpha \quad (2.2)$$

where $(0 < \alpha < 1)$ is the order of the differentiator. The magnitude response is given as $H(\omega) = (\omega/\omega_0)^\alpha$, from which is obvious that the unity gain frequency has the same expression as in the case of its integer-order counterpart. Also, in this case the phase response is constant but equal to $\alpha\pi/2$ predicting the total reliance of phase from the fractional-order α [6].

Comparing the above expressions of magnitude responses of fractional and integer-order differentiator, it is obvious that at the same frequency the fractional-order differentiator realizes a gain smaller than that achieved by its integer-order counterpart. As a result, with the substitution of (2.1) into (2.2), the transfer function of fractional-order differentiator is expressed as shown in (2.3), where α_i ($i = 0, 1, 2$) is given by (1.6) or (1.10). Their values depend on the type of the approximation that has been utilized.

$$H_{\text{diff}}(s) = \frac{\left(\frac{\alpha_0}{\alpha_2}\right)s^2 + \left(\frac{\alpha_1}{\alpha_2}\right)\frac{1}{\tau}s + \frac{1}{\tau^2}}{s^2 + \left(\frac{\alpha_1}{\alpha_2}\right)\frac{1}{\tau}s + \left(\frac{\alpha_0}{\alpha_2}\right)\frac{1}{\tau^2}} \quad (2.3)$$

2.2.2 Fractional-Order Integrator

The transfer function of a fractional-order lossless integrator could be written as shown in (2.4), while the magnitude response is given as $H(\omega) = (\omega_o/\omega)^\alpha$, where $\omega_o = 1/\tau$ is the unity gain frequency of the integrator. Its phase response will be a constant equal to $-\alpha\pi/2$.

$$H(s) = \frac{1}{(\tau s)^\alpha} \quad (2.4)$$

The corresponding expressions of its integer-order counterpart with the same unity gain frequency will be $H(\omega) = \omega_o/\omega$ and $-\pi/2$, respectively. By using the same order of approximation as in the case of fractional-order differentiator, the transfer function in (2.4) could be approximated as it is demonstrated in (2.5), where α_i ($i = 0,1,2$) is given by (1.6) or (1.10).

$$H_{\text{int}}(s) = \frac{\left(\frac{\alpha_2}{\alpha_0}\right)s^2 + \left(\frac{\alpha_1}{\alpha_0}\right)\frac{1}{\tau}s + \frac{1}{\tau^2}}{s^2 + \left(\frac{\alpha_1}{\alpha_0}\right)\frac{1}{\tau}s + \left(\frac{\alpha_2}{\alpha_0}\right)\frac{1}{\tau^2}} \quad (2.5)$$

Taking into account that the transfer function in (2.3) and (2.5) have an integer-order form, they could be easily performed either by the typical functional block diagram (FBD) of the follow-the-leader-feedback (FLF) topology depicted in Fig. 2.1a, or the inverse-follow-the-leader, multi-feedback (IFLF) topology given in Fig. 2.1b, where the notation (xG_i) implies a scaled replica of the corresponding output. The transfer function is that in (2.6). Comparing (2.3) and (2.5) with (2.6)

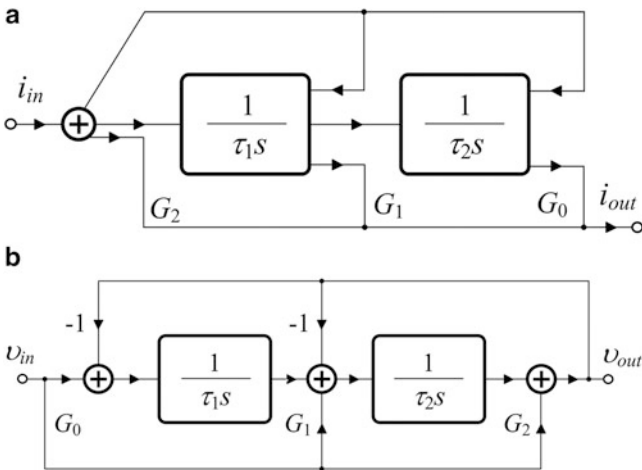


Fig. 2.1 FBD for realizing fractional-order differentiator/integrator of order α using (a) FLF current-mode topology, (b) IFLF voltage-mode topology

Table 2.1 Design expressions of time-constants τ_i for approximating fractional-order differentiator, lossless integrator with unity gain frequency ($\omega_o = 1/\tau$)

Transfer function	τ_1	τ_2
$H(s) = (\tau s)^\alpha$	$\left(\frac{\alpha_2}{\alpha_1}\right) \cdot \tau$	$\left(\frac{\alpha_1}{\alpha_0}\right) \cdot \tau$
$H(s) = \frac{1}{(\tau s)^\alpha}$	$\left(\frac{\alpha_0}{\alpha_1}\right) \cdot \tau$	$\left(\frac{\alpha_1}{\alpha_2}\right) \cdot \tau$

Table 2.2 Design expressions of gain factors G_i for approximating fractional-order differentiator, lossless integrator with unity gain frequency ($\omega_o = 1/\tau$)

Transfer function	G_2	G_1	G_0
$H(s) = (\tau s)^\alpha$	$\left(\frac{\alpha_0}{\alpha_2}\right)$	1	$\left(\frac{\alpha_2}{\alpha_0}\right)$
$H(s) = \frac{1}{(\tau s)^\alpha}$	$\left(\frac{\alpha_2}{\alpha_0}\right)$	1	$\left(\frac{\alpha_0}{\alpha_2}\right)$

the derived expressions of time-constants τ_i and gain factors G_i ($i = 0,1,2$) are as summarized in Tables 2.1, and 2.2, respectively.

$$H(s) = \frac{G_2 s^2 + \frac{G_1}{\tau_1} s + \frac{G_0}{\tau_1 \tau_2}}{s^2 + \frac{1}{\tau_1} s + \frac{1}{\tau_1 \tau_2}} \quad (2.6)$$

2.3 Fractional-Order Generalized Filters (Order α)

Fractional-order filters of order α where ($0 < \alpha < 1$) will be presented and some of the most critical frequencies have been derived in order to be fully characterized. From the stability point of view, this system is stable if and only if $\alpha > 0$ and $\alpha < 2$, while it will oscillate if and only if $\alpha > 0$ and $\alpha = 2$; otherwise it is unstable. The derived frequency responses of filters of order α exhibit a stopband attenuation proportionate to the fractional-order α , which offers a more precise control of the attenuation gradient compared to the attenuation offered in the case of integer-order filters of order n , which is $-6 \cdot n$ dB/oct [6–19].

Thus, low-pass, high-pass, band-pass, and all-pass filters of order α will be presented. Also, using a general topology, all the aforementioned type of filters could be realized, using the same core. The most important critical frequencies that will be studied are the following:

- ω_p is the frequency at which the magnitude response has a maximum or a minimum and is obtained by solving the equation $\frac{d}{d\omega} |H(j\omega)|_{\omega=\omega_p} = 0$
- ω_h is the half-power frequency at which $|H(j\omega)|_{\omega=\omega_h} = |H(j\omega)|_{\omega=\omega_p} / \sqrt{2}$
- ω_{rp} is the right-phase frequency at which the phase $\angle H(j\omega) = \pm \pi/2$

It should be mentioned that ω_{rp} exists only if $\alpha > 1$.

2.3.1 Fractional-Order Low-Pass Filter (FLPF)

The transfer function of a FLPF is that in (2.7), where κ is the low-frequency gain and $\omega_o \equiv 1/\tau$ the pole frequency. The magnitude and phase response are given by (2.8). The critical frequencies are summarized in Table 2.3, where the magnitude and phase values are also given. Using (2.8), the expressions for the ω_h and the corresponding phase are these in (2.9).

$$H(s) = \kappa \frac{\omega_o^\alpha}{s^\alpha + \omega_o^\alpha} = \kappa \frac{1}{(\tau s)^\alpha + 1} \quad (2.7)$$

$$|H(j\omega)| = \frac{\kappa}{\sqrt{\left(\frac{\omega}{\omega_o}\right)^{2\alpha} + 2\left(\frac{\omega}{\omega_o}\right)^\alpha \cos\left(\frac{\alpha\pi}{2}\right) + 1}} \quad (2.8a)$$

$$\angle H(j\omega) = \angle \kappa - \tan^{-1} \left(\frac{\left(\frac{\omega}{\omega_o}\right)^\alpha \sin\left(\frac{\alpha\pi}{2}\right)}{\left(\frac{\omega}{\omega_o}\right)^\alpha \cos\left(\frac{\alpha\pi}{2}\right) + 1} \right) \quad (2.8b)$$

In addition, the peak and right-phase frequency are found as $\omega_p = \omega_o[-\cos(\alpha\pi/2)]^{1/\alpha}$, and $\omega_{\text{rp}} = \omega_o[-\cos(\alpha\pi/2)]^{1/\alpha}$. The stopband attenuation gradient of the fractional-order low-pass filter order α is equal to $-6 \cdot \alpha$ dB/oct.

$$\omega_h = \omega_o \left[\sqrt{1 + \cos^2\left(\frac{\alpha\pi}{2}\right)} - \cos\left(\frac{\alpha\pi}{2}\right) \right]^{1/\alpha} \quad (2.9a)$$

$$\angle H(j\omega)_{\omega=\omega_h} = \angle \kappa - \tan^{-1} \left(\frac{\sin\left(\frac{\alpha\pi}{2}\right)}{2\cos\left(\frac{\alpha\pi}{2}\right) + \sqrt{1 + \cos^2\left(\frac{\alpha\pi}{2}\right)}} \right) \quad (2.9b)$$

2.3.2 Fractional-Order High-Pass Filter (FHPF)

The transfer function of a FHPF with high-frequency gain κ and pole frequency $\omega_o \equiv 1/\tau$ is that in (2.10). The magnitude response and phase response are given by (2.11), while all the critical frequencies are summarized in Table 2.4.

Table 2.3 Magnitude and phase values at important frequencies for the FLPF

ω	$ H(j\omega) $	$\angle H(j\omega)$
$\rightarrow 0$	κ	$\angle \kappa$
ω_o	$\frac{\kappa}{2 \cos \frac{\alpha\pi}{4}}$	$\angle \kappa - \alpha\pi/4$
$\rightarrow \infty$	0	$\angle \kappa - \alpha\pi/2$
ω_h	$\kappa \cdot \frac{1}{\sqrt{2}}$	$\angle \kappa - \tan^{-1} \left(\frac{\sin\left(\frac{\alpha\pi}{2}\right)}{2\cos\left(\frac{\alpha\pi}{2}\right) + \sqrt{1 + \cos^2\left(\frac{\alpha\pi}{2}\right)}} \right)$

Table 2.4 Magnitude and phase values at important frequencies for the FHPF

ω	$ H(j\omega) $	$\angle H(j\omega)$
$\rightarrow 0$	0	$\angle \kappa + \alpha\pi/2$
ω_o	$\frac{\kappa}{2 \cos(\frac{\alpha\pi}{4})}$	$\angle \kappa + \alpha\pi/4$
$\rightarrow \infty$	κ	$\angle \kappa$
ω_h	$\kappa \cdot \frac{1}{\sqrt{2}}$	$\angle \kappa + \frac{\alpha\pi}{2} - \tan^{-1} \left(\frac{\sin(\frac{\alpha\pi}{2})}{\sqrt{1 + \cos^2(\frac{\alpha\pi}{2})}} \right)$

$$H(s) = \kappa \frac{\omega_o^\alpha s^\alpha}{s^\alpha + \omega_o^\alpha} = \kappa \frac{(\tau s)^\alpha}{(\tau s)^\alpha + 1} \quad (2.10)$$

$$|H(j\omega)| = \frac{\kappa \left(\frac{\omega}{\omega_o}\right)^\alpha}{\sqrt{\left(\frac{\omega}{\omega_o}\right)^{2\alpha} + 2\left(\frac{\omega}{\omega_o}\right)^\alpha \cos\left(\frac{\alpha\pi}{2}\right) + 1}} \quad (2.11a)$$

$$\angle H(j\omega) = \angle \kappa + \alpha\pi/2 - \tan^{-1} \left(\frac{\left(\frac{\omega}{\omega_o}\right)^\alpha \sin\left(\frac{\alpha\pi}{2}\right)}{\left(\frac{\omega}{\omega_o}\right)^\alpha \cos\left(\frac{\alpha\pi}{2}\right) + 1} \right) \quad (2.11b)$$

The corresponding expressions for the ω_h and phase at this frequency are given by (2.12). In addition, the peak, and right-phase frequency are found as $\omega_p = \omega_o [-\cos(\alpha\pi/2)]^{1/\alpha}$, and $\omega_{rp} = \omega_o [-\cos(\alpha\pi/2)]^{1/\alpha}$. From these expressions it is seen that both ω_p and ω_{rp} exist only if $\alpha > 1$. Also, the stopband attenuation gradient of the fractional-order high-pass filter of order α is equal to $+6\alpha$ dB/oct.

$$\omega_h = \omega_o \left[\sqrt{1 + \cos^2\left(\frac{\alpha\pi}{2}\right)} + \cos\left(\frac{\alpha\pi}{2}\right) \right]^{1/\alpha} \quad (2.12a)$$

$$\angle H(j\omega)_{\omega=\omega_h} = \angle \kappa + \frac{\alpha\pi}{2} - \tan^{-1} \left(\frac{\sin\left(\frac{\alpha\pi}{2}\right)}{\sqrt{1 + \cos^2\left(\frac{\alpha\pi}{2}\right)}} \right) \quad (2.12b)$$

2.3.3 Fractional-Order Band-Pass Filter (FBPF)

The transfer function of a FBPF with peak-frequency gain κ and pole frequency $\omega_o \equiv 1/\tau$ is that in (2.13), where the magnitude and phase is as shown in (2.14a) and (2.14b), respectively. In order to obtain a FBPF response, the condition $\alpha > \beta$ should be fulfilled. All the critical frequencies are summarized in Table 2.5.

Table 2.5 Magnitude and phase values at important frequencies for the FBPF

ω	$ H(j\omega) $	$\angle H(j\omega)$
$\rightarrow 0$	0	$\angle \kappa + \beta\pi/2$
$\omega_p = \omega_o$	$\frac{\omega_o^\beta}{2 \cos(\frac{\alpha\pi}{4})}$	$\angle \kappa + [(2\beta - \alpha)\pi]/4$
$\rightarrow \infty$	$\omega_o^\alpha \omega^{\beta-\alpha}$	$\angle \kappa + [(\beta - \alpha)\pi]/2$

$$H(s) = \kappa \frac{\omega_o^\alpha s^\beta}{s^\alpha + \omega_o^\alpha} = \kappa \frac{(\tau s)^\beta}{(\tau s)^\alpha + 1} \quad (2.13)$$

$$|H(j\omega)| = \frac{\kappa \left(\frac{\omega}{\omega_o}\right)^\beta}{\sqrt{\left(\frac{\omega}{\omega_o}\right)^{2\alpha} + 2\left(\frac{\omega}{\omega_o}\right)^\alpha \cos\left(\frac{\alpha\pi}{2}\right) + 1}} \quad (2.14a)$$

$$\angle H(j\omega) = \angle \kappa + \beta\pi/2 - \tan^{-1} \left(\frac{\left(\frac{\omega}{\omega_o}\right)^\alpha \sin\left(\frac{\alpha\pi}{2}\right)}{\left(\frac{\omega}{\omega_o}\right)^\alpha \cos\left(\frac{\alpha\pi}{2}\right) + 1} \right) \quad (2.14b)$$

The peak frequency (ω_p), calculated from the condition $\frac{d}{d\omega}|H(j\omega)|_{\omega=\omega_p} = 0$, is given by (2.15). In the case that $\alpha = 2\beta$, then $\omega_p = \omega_o$. Obviously, for $\alpha = \beta$, the transfer function in (2.13) is modified and corresponds to the already known FHFP.

$$\omega_p = \omega_o \left\{ \frac{\cos\left(\frac{\alpha\pi}{2}\right) \left[(2\beta - \alpha) + \sqrt{\alpha^2 + 4\beta(\alpha - \beta)\tan^2\left(\frac{\alpha\pi}{2}\right)} \right]}{2(\alpha - \beta)} \right\}^{1/\alpha} \quad (2.15)$$

All the critical frequencies are summarized in Table 2.5, where the magnitude and phase values are also given. It should be mentioned that the stopband attenuation gradient at the upper frequencies is $-6 \cdot (\alpha - \beta)$ dB/oct, while for the lower frequencies is $+6 \beta$ dB/oct, offering the capability of realizing a low- Q band pass filter with different slopes of the stopband attenuations. In case that $\alpha = 2\beta$, the slope is then equal to -6β dB/oct, and $+6 \beta$ dB/oct, respectively.

2.3.4 Fractional-Order All-Pass Filter (FAPF)

A FAPF with gain κ and pole frequency $\omega_o \equiv 1/\tau$ is described through the transfer function given by (2.16)

$$H(s) = \kappa \frac{s^\alpha - \omega_o^\alpha}{s^\alpha + \omega_o^\alpha} = \kappa \frac{(\tau s)^\alpha - 1}{(\tau s)^\alpha + 1} \quad (2.16)$$

Table 2.6 Magnitude and phase values at important frequencies for the FAPF

ω	$ H(j\omega) $	$\angle H(j\omega)$
$\rightarrow 0$	0	$\angle \kappa + \pi$
$\omega_p = \omega_o$	$\kappa \cdot \tan\left(\frac{\alpha\pi}{4}\right)$	$\angle \kappa + \pi/2$
ω_h	κ	$\angle \kappa$

Its frequency behavior is described by (2.17)

$$|H(j\omega)| = \kappa \sqrt{\frac{\left(\frac{\omega}{\omega_o}\right)^{2\alpha} - 2\left(\frac{\omega}{\omega_o}\right)^\alpha \cos\left(\frac{\alpha\pi}{2}\right) + 1}{\left(\frac{\omega}{\omega_o}\right)^{2\alpha} + 2\left(\frac{\omega}{\omega_o}\right)^\alpha \cos\left(\frac{\alpha\pi}{2}\right) + 1}} \quad (2.17a)$$

It can be easily seen here that $\omega_p = \omega_{rp} = \omega_o$, as well as that at this frequency a minima occurs if $\alpha < 1$ and a maxima occurs if $\alpha > 1$ while the magnitude remains flat when $\alpha = 1$ (i.e., classical integer-order all-pass filter). All the critical frequencies are summarized in Table 2.6 where the magnitude and phase values are also given.

$$\begin{aligned} \angle H(j\omega) = \angle \kappa \\ - \tan^{-1} \left(\frac{\left(\frac{\omega}{\omega_o}\right)^\alpha \sin\left(\frac{\alpha\pi}{2}\right)}{\left(\frac{\omega}{\omega_o}\right)^\alpha \cos\left(\frac{\alpha\pi}{2}\right) - 1} \right) - \tan^{-1} \left(\frac{\left(\frac{\omega}{\omega_o}\right)^\alpha \sin\left(\frac{\alpha\pi}{2}\right)}{\left(\frac{\omega}{\omega_o}\right)^\alpha \cos\left(\frac{\alpha\pi}{2}\right) + 1} \right) \end{aligned} \quad (2.17b)$$

2.3.5 Design Equations for Generalized Filters of Order α

Taking into account that the transfer functions of all the aforementioned fractional-order filters are expressed through the variables $(\tau s)^\alpha$ and/or $(\tau s)^\beta$, and the fact that they are not realizable, they should be approximated by appropriate expressions. Using the second-order expressions of the CFE given by (2.1) and substituting into (2.7), (2.10), (2.13), and (2.16), the derived transfer functions are given in (2.18).

The coefficient α_i corresponds to the approximation of variable $(\tau s)^\alpha$, while b_i to the variable $(\tau s)^\beta$. Comparing the transfer functions of the FLPF and FHPPF, the numerator in $H_{HP}(s)$ is easily derived through the substitution: $\alpha_0 \leftrightarrow \alpha_2$ in the numerator of $H_{LP}(s)$.

Inspecting the transfer functions of FLPF, FHPPF, and FAPF it is concluded that all of them have the same form. Consequently, they could be realized by the same topology just by changing the coefficient values. A suitable solution for this purpose has been already given in Fig. 2.1, where the realized transfer function is that given in (2.6).

$$H_{\alpha}^{\text{LP}}(s) = \frac{\kappa}{\alpha_0 + \alpha_2} \cdot \frac{\alpha_2 s^2 + \alpha_1 \frac{1}{\tau} s + \alpha_0 \frac{1}{\tau^2}}{s^2 + \left(\frac{2\alpha_1}{\alpha_0 + \alpha_2}\right) \frac{1}{\tau} s + \frac{1}{\tau^2}} \quad (2.18a)$$

$$H_{\alpha}^{\text{HP}}(s) = \frac{\kappa}{\alpha_0 + \alpha_2} \cdot \frac{\alpha_0 s^2 + \alpha_1 \frac{1}{\tau} s + \alpha_2 \frac{1}{\tau^2}}{s^2 + \left(\frac{2\alpha_1}{\alpha_0 + \alpha_2}\right) \frac{1}{\tau} s + \frac{1}{\tau^2}} \quad (2.18b)$$

$$H_{\alpha}^{\text{AP}}(s) = \kappa \frac{\alpha_0 - \alpha_2}{\alpha_0 + \alpha_2} \cdot \frac{s^2 - \frac{1}{\tau^2}}{s^2 + \left(\frac{2\alpha_1}{\alpha_0 + \alpha_2}\right) \frac{1}{\tau} s + \frac{1}{\tau^2}} \quad (2.18c)$$

$$H_{\alpha}^{\text{BP}}(s) = \frac{\kappa}{\alpha_0 + \alpha_2} \cdot \frac{\alpha_2 s^2 + \alpha_1 \frac{1}{\tau} s + \alpha_0 \frac{1}{\tau^2}}{s^2 + \left(\frac{2\alpha_1}{\alpha_0 + \alpha_2}\right) \frac{1}{\tau} s + \frac{1}{\tau^2}} \cdot \frac{1}{b_2} \cdot \frac{b_0 s^2 + b_1 \frac{1}{\tau} s + b_2 \frac{1}{\tau^2}}{s^2 + \left(\frac{b_1}{b_2}\right) \frac{1}{\tau} s + \frac{b_0}{b_2} \frac{1}{\tau^2}} \quad (2.18d)$$

Comparing the coefficients of (2.6) with those of FLPF, FHPF, and FAPF in (2.18), it is derived that the design equations about the time-constants of fractional-order low-pass, high-pass, and all-pass filters of order α are those in (2.19). The corresponding design equations for the scaling factors G_i ($i = 0, 1, 2$) are summarized in Table 2.7.

$$\tau_1 = \frac{\alpha_0 + \alpha_2}{2\alpha_1} \cdot \tau \quad (2.19a)$$

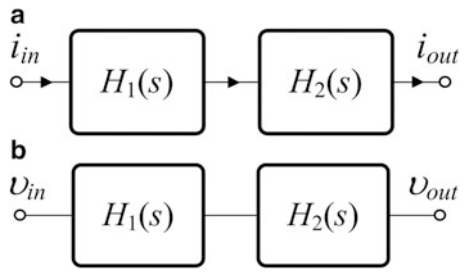
$$\tau_2 = \frac{2\alpha_1}{\alpha_2 + \alpha_0} \cdot \tau \quad (2.19b)$$

With regards to the FBPF realization, a possible solution is the FBD in Fig. 2.2, where $H_1(s)$ and $H_2(s)$ are mentioned filter blocks as that in Fig. 2.1, which realize the transfer function in (2.6). The expressions for time-constants τ_{ij} , where ($i = 1, 2$) is the number of time-constants of each state, and ($j = 1, 2$) is the number of state, are given by (2.20). The time-constants of the first stage τ_{i1} have the same values as in (2.19). The corresponding design equation for the scaling factors G_{ij} ($i = 0, 1, 2$ and $j = 1, 2$) of both stages are also summarized in Table 2.7.

Table 2.7 Values of scaling factors G_{ij} for realizing FLPF, FHPF, FAPF, and FBPF of order α in Figs 2.1, and 2.2

Filter		G_2	G_1	G_0
FLPF		$\kappa \cdot \frac{\alpha_2}{\alpha_2 + \alpha_0}$	$\frac{\kappa}{2}$	$\kappa \cdot \frac{\alpha_0}{\alpha_2 + \alpha_0}$
FHPF		$\kappa \cdot \frac{\alpha_0}{\alpha_2 + \alpha_0}$	$\frac{\kappa}{2}$	$\kappa \cdot \frac{\alpha_2}{\alpha_0 + \alpha_2}$
FAPF		$\kappa \cdot \frac{\alpha_0 - \alpha_2}{\alpha_2 + \alpha_0}$	0	$-\kappa \cdot \frac{\alpha_0 - \alpha_2}{\alpha_2 + \alpha_0}$
FBPF	($j = 1$)	$\kappa \cdot \frac{\alpha_2}{\alpha_2 + \alpha_0}$	$\frac{\kappa}{2}$	$\kappa \cdot \frac{\alpha_0}{\alpha_2 + \alpha_0}$
	($j = 2$)	$\frac{b_0}{b_2}$	1	$\frac{b_2}{b_0}$

Fig. 2.2 FBD for realizing FBPF of order α using (a) current mode topology, (b) voltage mode topology



$$\tau_{11} = \frac{\alpha_0 + \alpha_2}{2\alpha_1} \cdot \tau, \quad \tau_{12} = \frac{b_2}{b_1} \cdot \tau \quad (2.20a)$$

$$\tau_{21} = \frac{2\alpha_1}{\alpha_2 + \alpha_0} \cdot \tau, \quad \tau_{22} = \frac{b_1}{b_0} \cdot \tau \quad (2.20b)$$

2.4 Fractional-Order Generalized Filters (Order $1 + \alpha$)

Although, fractional-order filters constitute a small portion of fractional-order calculus, they have gained a growing research interest offering important features especially on behavior of the attenuation gradient. The stopband attenuation of integer order filters has been limited to increments based on the order n , but using the fractional Laplacian operator attenuations between these integer steps can be achieved creating fractional step filter of order $(n + \alpha)$, where α is the fractional step between integer orders n and $n + 1$ and is therefore limited to $(0 < \alpha < 1)$. The derived frequency responses of filters of order $1 + \alpha$ exhibit a stopband attenuation equal to $-6 \cdot (1 + \alpha)$ dB/oct, which offer a more precise control of the attenuation gradient compared to the attenuation offered in the case of integer-order filters of order n , which is $-6 \cdot n$ dB/oct [6–19]. In this section, low-pass, high-pass, band-pass, and band-stop filters of order $1 + \alpha$ are presented, and some of the most critical frequencies (ω_p , ω_h) are also given in order to be fully characterized. Finally, using the CFE method, the derived design equations results into a general topology, from which all the aforementioned type of filters could be realized.

2.4.1 Fractional-Order Low-Pass Filter (FLPF)

According to the analysis provided in [8], the direct realization of a fractional filter of the order $n + \alpha$ is stable in the case that $n + \alpha < 2$. Therefore, only fractional filters of the order $1 + \alpha$ offer realizations without stability problem. The transfer function of a $1 + \alpha$ -order fractional low-pass filter is given by

$$H(s) = \frac{\kappa_1}{s^{1+\alpha} + \kappa_2} \quad (2.21)$$

where the low-frequency gain is equal to κ_1/κ_2 , and the -3 dB frequency is given by (2.22)

$$\omega_{-3\text{dB}} = \left[\kappa_2 \left(\sqrt{1 + \cos^2 \frac{(1+\alpha)\pi}{2}} \right) - \cos \frac{(1+\alpha)\pi}{2} \right]^{\frac{1}{1+\alpha}} \quad (2.22)$$

The obtained frequency responses suffer from the presence of an undesired peaking equal to $\kappa_1/\kappa_2[(\sin(1+\alpha)\pi/2)]$ at the frequency $\omega_p = [-\kappa_2 \cos(1+\alpha)\pi/2]^{-(1+\alpha)}$. In order to overcome this problem, the modified transfer function given by (2.23), which intends to approximate the all-pole Butterworth response, is introduced, where an extra term equal to $\kappa_3 s^\alpha$ has been added in the denominator of the transfer function in (2.21). The transfer function of a FLPF with low-frequency gain κ_1/κ_2 and pole frequency $\omega_o = 1/\tau$ is that in (2.23)

$$H(s) = \frac{\kappa_1}{(\tau s)^{1+\alpha} + \kappa_3 (\tau s)^\alpha + \kappa_2} \quad (2.23)$$

The factors κ_i ($i = 1, 2, 3$) are calculated by appropriate expressions, in order to minimize the error in the frequency response [9]. Such expressions are recalled in (2.24).

$$\begin{aligned} \kappa_1 &= 1 \\ \kappa_2 &= 0.2937\alpha + 0.71216 \\ \kappa_3 &= 1.068\alpha^2 + 0.161\alpha + 0.3324 \end{aligned} \quad (2.24)$$

The magnitude response and phase response are given by (2.25) as

$$|H(j\omega)| = \frac{\kappa_1}{\sqrt{\left(\frac{\omega}{\omega_o}\right)^{2(1+\alpha)} - 2\kappa_2 \left(\frac{\omega}{\omega_o}\right)^{1+\alpha} \sin\left(\frac{\alpha\pi}{2}\right) + \kappa_3^2 \left(\frac{\omega}{\omega_o}\right)^{2\alpha} + 2\kappa_2\kappa_3 \left(\frac{\omega}{\omega_o}\right)^\alpha \cos\left(\frac{\alpha\pi}{2}\right) + \kappa_2^2}} \quad (2.25a)$$

$$\angle H(j\omega) = \angle \kappa_1 - \tan^{-1} \left(\frac{\left(\frac{\omega}{\omega_o}\right)^{1+\alpha} \cos\left(\frac{\alpha\pi}{2}\right) + \kappa_3 \left(\frac{\omega}{\omega_o}\right)^\alpha \sin\left(\frac{\alpha\pi}{2}\right)}{-\left(\frac{\omega}{\omega_o}\right)^{1+\alpha} \sin\left(\frac{\alpha\pi}{2}\right) + \kappa_3 \left(\frac{\omega}{\omega_o}\right)^\alpha \cos\left(\frac{\alpha\pi}{2}\right) + \kappa_2} \right) \quad (2.25b)$$

The peak frequency (ω_p) is calculated solving the following equation:

$$\begin{aligned} 2(1+\alpha) \left(\frac{\omega_p}{\omega_o}\right)^{2+\alpha} - 2\kappa_2(1+\alpha) \left(\frac{\omega_p}{\omega_o}\right) \sin\left(\frac{\alpha\pi}{2}\right) \\ + 2\alpha\kappa_3^2 \left(\frac{\omega_p}{\omega_o}\right)^\alpha + 2\alpha\kappa_2\kappa_3 \cos\left(\frac{\alpha\pi}{2}\right) = 0 \end{aligned} \quad (2.26)$$

which is derived from (2.25) under the condition $\frac{d}{d\omega}|H(j\omega)|_{\omega=\omega_p} = 0$.

The half-power (-3 dB) frequency (ω_h), defined as the frequency where there is a 0.707 drop of the passband gain, is calculated solving the following equation:

$$\begin{aligned} \left(\frac{\omega_h}{\omega_o}\right)^{2(1+\alpha)} - 2\kappa_2\left(\frac{\omega_h}{\omega_o}\right)^{1+\alpha} \sin\left(\frac{\alpha\pi}{2}\right) + \kappa_3^2\left(\frac{\omega_h}{\omega_o}\right)^{2\alpha} \\ + 2\kappa_2\kappa_3\left(\frac{\omega_h}{\omega_o}\right)^\alpha \cos\left(\frac{\alpha\pi}{2}\right) - \kappa_2^2 = 0 \end{aligned} \quad (2.27)$$

Also, the stopband attenuation gradient of the $1 + \alpha$ fractional-order low-pass filter is equal to $-6 \cdot (1 + \alpha)$ dB/oct.

2.4.2 Fractional-Order High-Pass Filter (FHPF)

The transfer function of a FHPF is given by (2.28)

$$H(s) = \frac{\kappa_1 s^{1+\alpha}}{(\tau s)^{1+\alpha} + \kappa_3 (\tau s)^\alpha + \kappa_2} \quad (2.28)$$

The magnitude response and phase response are given by (2.29).

$$|H(j\omega)| = \frac{\kappa_1 \left(\frac{\omega}{\omega_o}\right)^{1+\alpha}}{\sqrt{\left(\frac{\omega}{\omega_o}\right)^{2(1+\alpha)} - 2\kappa_2\left(\frac{\omega}{\omega_o}\right)^{1+\alpha} \sin\left(\frac{\alpha\pi}{2}\right) + \kappa_3^2\left(\frac{\omega}{\omega_o}\right)^{2\alpha} + 2\kappa_2\kappa_3\left(\frac{\omega}{\omega_o}\right)^\alpha \cos\left(\frac{\alpha\pi}{2}\right) + \kappa_2^2}} \quad (2.29a)$$

$$\begin{aligned} \angle H(j\omega) = \angle \kappa_1 + \frac{(1 + \alpha)\pi}{2} \\ - \tan^{-1} \left(\frac{\left(\frac{\omega}{\omega_o}\right)^{1+\alpha} \cos\left(\frac{\alpha\pi}{2}\right) + \kappa_3\left(\frac{\omega}{\omega_o}\right)^\alpha \sin\left(\frac{\alpha\pi}{2}\right)}{-\left(\frac{\omega}{\omega_o}\right)^{1+\alpha} \sin\left(\frac{\alpha\pi}{2}\right) + \kappa_3\left(\frac{\omega}{\omega_o}\right)^\alpha \cos\left(\frac{\alpha\pi}{2}\right) + \kappa_2} \right) \end{aligned} \quad (2.29b)$$

The peak frequency (ω_p) is calculated solving the equation given in (2.30), which is derived from (2.29) under the condition $\frac{d}{d\omega}|H(j\omega)|_{\omega=\omega_p} = 0$.

$$\begin{aligned} \kappa_2(1 + \alpha)\left(\frac{\omega_p}{\omega_o}\right)^{1+\alpha} \sin\left(\frac{\alpha\pi}{2}\right) - \kappa_3^2\left(\frac{\omega_p}{\omega_o}\right)^{2\alpha} \\ - (2 + \alpha)\kappa_2\kappa_3\left(\frac{\omega_p}{\omega_o}\right)^\alpha \cos\left(\frac{\alpha\pi}{2}\right) - (1 + \alpha)\kappa_2^2 = 0 \end{aligned} \quad (2.30)$$

The half-power (-3 dB) frequency (ω_h), defined as the frequency where there is a 0.707 drop of the passband gain, is calculated solving the equation given in (2.31).

Also, the stopband attenuation gradient of the fractional-order high-pass filter order $1 + \alpha$ is equal to $+6 \cdot (1 + \alpha)$ dB/oct.

$$\begin{aligned} & \left(\frac{\omega_h}{\omega_o}\right)^{2(1+\alpha)} + 2\kappa_2 \left(\frac{\omega_h}{\omega_o}\right)^{1+\alpha} \sin\left(\frac{\alpha\pi}{2}\right) - \kappa_3^2 \left(\frac{\omega_h}{\omega_o}\right)^{2\alpha} \\ & - 2\kappa_2\kappa_3 \left(\frac{\omega_h}{\omega_o}\right)^\alpha \cos\left(\frac{\alpha\pi}{2}\right) - \kappa_2^2 = 0 \end{aligned} \quad (2.31)$$

2.4.3 Fractional-Order Band-Pass Filter (FBPF)

The transfer function of a FBPF is given by (2.32)

$$H(s) = \kappa_1 \frac{\kappa_3 (\tau s)^a}{(\tau s)^{1+a} + \kappa_3 (\tau s)^a + \kappa_2} \quad (2.32)$$

Using (2.32), the magnitude and phase response are given as

$$|H(j\omega)| = \frac{\kappa_1 \kappa_3 \left(\frac{\omega}{\omega_o}\right)^\alpha}{\sqrt{\left(\frac{\omega}{\omega_o}\right)^{2(1+\alpha)} - 2\kappa_2 \left(\frac{\omega}{\omega_o}\right)^{1+\alpha} \sin\left(\frac{\alpha\pi}{2}\right) + \kappa_3^2 \left(\frac{\omega}{\omega_o}\right)^{2\alpha} + 2\kappa_2\kappa_3 \left(\frac{\omega}{\omega_o}\right)^\alpha \cos\left(\frac{\alpha\pi}{2}\right) + \kappa_2^2}} \quad (2.33a)$$

$$\begin{aligned} \angle H(j\omega) &= \angle \kappa_1 \kappa_3 + \frac{\alpha\pi}{2} \\ & - \tan^{-1} \left(\frac{\left(\frac{\omega}{\omega_o}\right)^{1+\alpha} \cos\left(\frac{\alpha\pi}{2}\right) + \kappa_3 \left(\frac{\omega}{\omega_o}\right)^\alpha \sin\left(\frac{\alpha\pi}{2}\right)}{-\left(\frac{\omega}{\omega_o}\right)^{1+\alpha} \sin\left(\frac{\alpha\pi}{2}\right) + \kappa_3 \left(\frac{\omega}{\omega_o}\right)^\alpha \cos\left(\frac{\alpha\pi}{2}\right) + \kappa_2} \right) \end{aligned} \quad (2.33b)$$

The peak frequency (ω_p) is calculated solving the equation given in (2.34), which is derived from (2.33a) under the condition $\frac{d}{d\omega} |H(j\omega)|_{\omega=\omega_p} = 0$.

$$\begin{aligned} & \left(\frac{\omega_p}{\omega_o}\right)^{2(1+\alpha)} - (1 - \alpha)\kappa_2 \left(\frac{\omega_p}{\omega_o}\right)^{1+\alpha} \sin\left(\frac{\alpha\pi}{2}\right) \\ & - \alpha\kappa_2\kappa_3 \left(\frac{\omega_p}{\omega_o}\right)^\alpha \cos\left(\frac{\alpha\pi}{2}\right) - \alpha\kappa_2^2 = 0 \end{aligned} \quad (2.34)$$

The half-power (-3 dB) frequencies (ω_{h1} , ω_{h2}) are defined as the frequencies where there is a 0.707 drop of the passband gain. The quality factor of the filter (Q) is calculated solving the following equation:

$$Q = \frac{\omega_p}{\omega_{h2} - \omega_{h1}} \quad (2.35)$$

where ω_{h2} and ω_{h1} are the upper and lower half-power frequencies, respectively.

Also, the stopband attenuation gradient at the upper frequencies is -6 dB/oct, while for the lower frequencies is $+6\cdot\alpha$ dB/oct, offering the capability of realizing a FBPF with the stopband attenuation being varied at the lower frequencies.

2.4.4 Fractional-Order Band-Stop Filter (FBSF)

A FBSF has the transfer function given by (2.36)

$$H(s) = \kappa_1 \frac{(\tau s)^{1+\alpha} + \kappa_2}{(\tau s)^{1+\alpha} + \kappa_3 (\tau s)^\alpha + \kappa_2} \quad (2.36)$$

The magnitude response and phase response are given by (2.37), while the peak frequency (ω_p) is calculated from (2.37) under the condition $\frac{d}{d\omega}|H(j\omega)|_{\omega=\omega_p} = 0$. The half-power (-3 dB) frequencies (ω_h) are calculated from the condition that at these frequencies there is a 0.707 drop of the passband gain.

$$|H(j\omega)| = \kappa_1 \sqrt{\frac{\left(\frac{\omega}{\omega_0}\right)^{2(1+\alpha)} - 2\kappa_2\left(\frac{\omega}{\omega_0}\right)^{1+\alpha} \sin\left(\frac{\alpha\pi}{2}\right) + \kappa_2^2}{\left(\frac{\omega}{\omega_0}\right)^{2(1+\alpha)} - 2\kappa_2\left(\frac{\omega}{\omega_0}\right)^{1+\alpha} \sin\left(\frac{\alpha\pi}{2}\right) + \kappa_3^2\left(\frac{\omega}{\omega_0}\right)^{2\alpha} + 2\kappa_2\kappa_3\left(\frac{\omega}{\omega_0}\right)^\alpha \cos\left(\frac{\alpha\pi}{2}\right) + \kappa_2^2}} \quad (2.37a)$$

$$\begin{aligned} \angle H(j\omega) = & \angle \kappa_1 + \tan^{-1} \left(\frac{\left(\frac{\omega}{\omega_0}\right)^{1+\alpha} \sin\left(\frac{\alpha\pi}{2}\right)}{-\left(\frac{\omega}{\omega_0}\right)^{1+\alpha} \cos\left(\frac{\alpha\pi}{2}\right) + \kappa_2} \right) \\ & - \tan^{-1} \left(\frac{\left(\frac{\omega}{\omega_0}\right)^{1+\alpha} \cos\left(\frac{\alpha\pi}{2}\right) + \kappa_3\left(\frac{\omega}{\omega_0}\right)^\alpha \sin\left(\frac{\alpha\pi}{2}\right)}{-\left(\frac{\omega}{\omega_0}\right)^{1+\alpha} \sin\left(\frac{\alpha\pi}{2}\right) + \kappa_3\left(\frac{\omega}{\omega_0}\right)^\alpha \cos\left(\frac{\alpha\pi}{2}\right) + \kappa_2} \right) \end{aligned} \quad (2.37b)$$

The quality factor of the filter is calculated according to the formula:

$$Q = \frac{\omega_p}{\omega_{h2} - \omega_{h1}} \quad (2.38)$$

where ω_{h2} and ω_{h1} are the upper and lower half-power frequencies, respectively.

2.4.5 Design Equations for Generalized Filters of Order $1 + \alpha$

The realization of the fractional-order filters of order $1 + \alpha$ has been achieved in a similar way as in the previous section, where the approximation of variable $(\tau s)^\alpha$

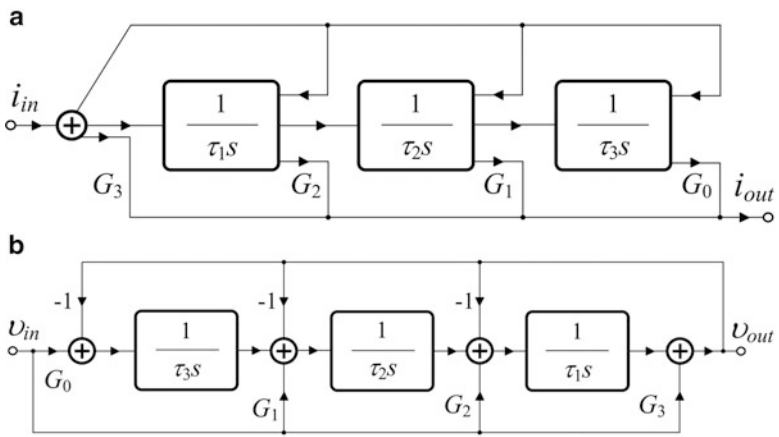


Fig. 2.3 FBD for realizing FLPF, FHPF, FBPF, and FBSF of order $1 + \alpha$ using (a) current mode topology, (b) voltage mode topology

has been performed through the utilization of the second-order expressions of the CFE given by (2.1) and substitution into (2.23), (2.28), (2.32), and (2.36). As a result, the derived transfer functions are that in (2.39).

Inspecting the transfer functions of FLPF, FHPF, FBPF, and FBSF, it is concluded that all of them have the same form. Consequently they could be realized by the same topology just by changing the coefficient values. A suitable solution for this purpose is depicted in Fig. 2.3, where a typical (FLF) topology and an (IFLF) topology are given in Fig. 2.3a and Fig. 2.3b, respectively. The realized transfer function is that given in (2.40).

$$H_{1+\alpha}^{\text{LP}}(s) = \frac{\kappa_1}{\alpha_0} \cdot \frac{\alpha_2 \frac{1}{\tau} s^2 + \alpha_1 \frac{1}{\tau^2} s + \alpha_0 \frac{1}{\tau^3}}{\left[s^3 + \left(\frac{\alpha_1 + \kappa_2 \alpha_2 + \kappa_3 \alpha_0}{\alpha_0} \right) \frac{1}{\tau} s^2 + \left(\frac{\alpha_2 + \kappa_2 \alpha_1 + \kappa_3 \alpha_1}{\alpha_0} \right) \frac{1}{\tau^2} s + \left(\frac{\kappa_3 \alpha_2 + \kappa_2 \alpha_0}{\alpha_0} \right) \frac{1}{\tau^3} \right]} \quad (2.39a)$$

$$H_{1+\alpha}^{\text{HP}}(s) = \frac{\kappa_1}{\alpha_0} \cdot \frac{\alpha_0 s^3 + \alpha_1 s^2 + \alpha_2 s}{\left[s^3 + \left(\frac{\alpha_1 + \kappa_2 \alpha_2 + \kappa_3 \alpha_0}{\alpha_0} \right) \frac{1}{\tau} s^2 + \left(\frac{\alpha_2 + \kappa_2 \alpha_1 + \kappa_3 \alpha_1}{\alpha_0} \right) \frac{1}{\tau^2} s + \left(\frac{\kappa_3 \alpha_2 + \kappa_2 \alpha_0}{\alpha_0} \right) \frac{1}{\tau^3} \right]} \quad (2.39b)$$

$$H_{1+\alpha}^{\text{BP}}(s) = \frac{\kappa_1 \kappa_3}{\alpha_0} \cdot \frac{\alpha_0 \frac{1}{\tau} s^2 + \alpha_1 \frac{1}{\tau^2} s + \alpha_2 \frac{1}{\tau^3}}{\left[s^3 + \left(\frac{\alpha_1 + \kappa_2 \alpha_2 + \kappa_3 \alpha_0}{\alpha_0} \right) \frac{1}{\tau} s^2 + \left(\frac{\alpha_2 + \kappa_2 \alpha_1 + \kappa_3 \alpha_1}{\alpha_0} \right) \frac{1}{\tau^2} s + \left(\frac{\kappa_3 \alpha_2 + \kappa_2 \alpha_0}{\alpha_0} \right) \frac{1}{\tau^3} \right]} \quad (2.39c)$$

Table 2.8 Values of scaling factors G_i ($i = 0, \dots, 3$) for realizing fractional low-pass, high-pass, band-pass, and band-stop filter in Fig. 2.3 of order $1 + \alpha$

Filter	G_3	G_2	G_1	G_0
FLPF	0	$\frac{\kappa_1 \alpha_2}{\kappa_2 \alpha_2 + \kappa_3 \alpha_0 + \alpha_1}$	$\frac{\kappa_1 \alpha_1}{\alpha_2 + (\kappa_2 + \kappa_3) \alpha_1}$	$\frac{\kappa_1 \alpha_0}{\kappa_2 \alpha_0 + \kappa_3 \alpha_2}$
FHPF	κ_1	$\frac{\kappa_1 \alpha_1}{\kappa_2 \alpha_2 + \kappa_3 \alpha_0 + \alpha_1}$	$\frac{\kappa_1 \alpha_2}{\alpha_2 + (\kappa_2 + \kappa_3) \alpha_1}$	0
FBPF	0	$\frac{\kappa_1 \kappa_3 \alpha_0}{\kappa_2 \alpha_2 + \kappa_3 \alpha_0 + \alpha_1}$	$\frac{\kappa_1 \kappa_3 \alpha_1}{\alpha_2 + (\kappa_2 + \kappa_3) \alpha_1}$	$\frac{\kappa_1 \kappa_3 \alpha_2}{\kappa_2 \alpha_0 + \kappa_3 \alpha_2}$
FBSF	κ_1	$\frac{\kappa_1 (\alpha_1 + \kappa_2 \alpha_2)}{\kappa_2 \alpha_2 + \kappa_3 \alpha_0 + \alpha_1}$	$\frac{\kappa_1 (\alpha_2 + \kappa_2 \alpha_1)}{\alpha_2 + (\kappa_2 + \kappa_3) \alpha_1}$	$\frac{\kappa_1 \kappa_2 \alpha_0}{\kappa_3 \alpha_2 + \kappa_2 \alpha_0}$

$$H_{1+\alpha}^{BS}(s) = \frac{\kappa_1}{\alpha_0} \cdot \frac{\alpha_0 s^3 + (\alpha_1 + \kappa_2 \alpha_2) \frac{1}{\tau} s^2 + (\alpha_2 + \kappa_2 \alpha_1) \frac{1}{\tau^2} s + (\kappa_2 \alpha_0) \frac{1}{\tau}}{\left[s^3 + \left(\frac{\alpha_1 + \kappa_2 \alpha_2 + \kappa_3 \alpha_0}{\alpha_0} \right) \frac{1}{\tau} s^2 + \left(\frac{\alpha_2 + \kappa_2 \alpha_1 + \kappa_3 \alpha_1}{\alpha_0} \right) \frac{1}{\tau^2} s + \left(\frac{\kappa_3 \alpha_2 + \kappa_2 \alpha_0}{\alpha_0} \right) \frac{1}{\tau^3} \right]} \quad (2.39d)$$

$$H(s) = \frac{G_3 s^3 + \frac{G_2}{\tau_1} s^2 + \frac{G_1}{\tau_1 \tau_2} s + \frac{G_0}{\tau_1 \tau_2 \tau_3}}{s^3 + \frac{1}{\tau_1} s^2 + \frac{1}{\tau_1 \tau_2} s + \frac{1}{\tau_1 \tau_2 \tau_3}} \quad (2.40)$$

Comparing the coefficients of (2.40) with these of FLPF, FHPF, and FBSF it is derived that the design equations about the time-constants τ_i ($i = 1, 2, 3$) of all the filters are given in (2.41).

$$\tau_1 = \frac{\alpha_0}{\kappa_2 \alpha_2 + \kappa_3 \alpha_0 + \alpha_1} \cdot \tau \quad (2.41a)$$

$$\tau_2 = \frac{\kappa_2 \alpha_2 + \kappa_3 \alpha_0 + \alpha_1}{\kappa_2 \alpha_1 + \kappa_3 \alpha_1 + \alpha_2} \cdot \tau \quad (2.41b)$$

$$\tau_3 = \frac{\kappa_2 \alpha_1 + \kappa_3 \alpha_1 + \alpha_2}{\kappa_2 \alpha_0 + \kappa_3 \alpha_2} \cdot \tau \quad (2.41c)$$

The corresponding design equations for the scaling factors G_i ($i = 0, \dots, 3$) are summarized in Table 2.8.

2.5 Fractional-Order Generalized Filters (Order $\alpha + \beta$)

The utilization of two different orders α and β , where $\alpha + \beta < 2$ and $\alpha, \beta > 0$ provides one more degree of freedom, which is able to vary, in order to realize fractional order filters of order $\alpha + \beta$. Such kind of filters exhibit a stopband attenuation which is proportionate to the fractional-order α, β . In this section,

FLPF, FHPF, FBPF, and FBSF of order $\alpha + \beta$ are presented, and some of the most critical frequencies have been derived in order to be fully characterized.

The most important critical frequencies that will be presented are the following:

- ω_p is the frequency at which the magnitude response has a maximum or a minimum and is obtained by solving the equation $\frac{d}{d\omega} |H(j\omega)|_{\omega=\omega_p} = 0$
- ω_h is the half-power frequency at which the power drops to half the passband power, i.e., $|H(j\omega)|_{\omega=\omega_h} = |H(j\omega)|_{\omega=\omega_p} / \sqrt{2}$

Also, using a general topology, all the aforementioned type of filters could be realized and this is very important from the flexibility point of view.

2.5.1 Fractional-Order Low-Pass Filter (FLPF)

The transfer function of the FLPF of order $\alpha + \beta$ is given by Eq. (2.42)

$$H(s) = \frac{\kappa_1}{(\tau s)^{\alpha+\beta} + \kappa_3(\tau s)^\beta + \kappa_2} \quad (2.42)$$

The magnitude response and phase response are given by (2.43). The half-power (-3 dB) frequency (ω_h), defined as the frequency where there is a 0.707 drop of the passband gain, is calculated solving the equation given by (2.44), which is derived taking into account that the maximum gain of the filter is κ_1/κ_2 . Also, the stopband attenuation gradient of the fractional-order low-pass filter of order $\alpha + \beta$ is equal to $-6 \cdot (\alpha + \beta)$ dB/oct.

$$|H(j\omega)| = \frac{\kappa_1}{\sqrt{\left(\left(\frac{\omega}{\omega_o}\right)^{2(\alpha+\beta)} + \kappa_3^2 \left(\frac{\omega}{\omega_o}\right)^{2\beta} + \kappa_2^2 + 2\kappa_3 \left(\frac{\omega}{\omega_o}\right)^{\alpha+2\beta} \cos\left(\frac{\alpha\pi}{2}\right) + 2\kappa_2 \left(\frac{\omega}{\omega_o}\right)^{\alpha+\beta} \cos\left[\frac{(\alpha+\beta)\pi}{2}\right] + 2\kappa_2\kappa_3 \left(\frac{\omega}{\omega_o}\right)^\beta \cos\left(\frac{\beta\pi}{2}\right)\right)}} \quad (2.43a)$$

$$\angle H(j\omega) = \angle \kappa_1 - \tan^{-1} \left(\frac{\left(\frac{\omega}{\omega_o}\right)^{\alpha+\beta} \sin\left[\frac{(\alpha+\beta)\pi}{2}\right] + \kappa_3 \left(\frac{\omega}{\omega_o}\right)^\beta \sin\left(\frac{\beta\pi}{2}\right)}{\left(\frac{\omega}{\omega_o}\right)^{\alpha+\beta} \cos\left[\frac{(\alpha+\beta)\pi}{2}\right] + \kappa_3 \left(\frac{\omega}{\omega_o}\right)^\beta \cos\left(\frac{\beta\pi}{2}\right) + \kappa_2} \right) \quad (2.43b)$$

$$\left(\frac{\omega_h}{\omega_o}\right)^{2(\alpha+\beta)} + 2\kappa_3 \left(\frac{\omega_h}{\omega_o}\right)^{\alpha+2\beta} \cos\left(\frac{\alpha\pi}{2}\right) + 2\kappa_2 \left(\frac{\omega_h}{\omega_o}\right)^{\alpha+\beta} \cos\left[\frac{(\alpha+\beta)\pi}{2}\right] + \kappa_3^2 \left(\frac{\omega_h}{\omega_o}\right)^{2\beta} + 2\kappa_2\kappa_3 \left(\frac{\omega_h}{\omega_o}\right)^\beta \cos\left(\frac{\beta\pi}{2}\right) - \kappa_2^2 = 0 \quad (2.44)$$

2.5.2 Fractional-Order High-Pass Filter (FHPF)

The transfer function of a HLPF with maximum gain equal to κ_1/κ_2 is that in (2.45)

$$H(s) = \frac{\kappa_1 (\tau s)^{\alpha+\beta}}{(\tau s)^{\alpha+\beta} + \kappa_3 (\tau s)^\beta + \kappa_2} \quad (2.45)$$

The magnitude response and phase response are given by (2.46) as

$$|H(j\omega)| = \frac{\kappa_1 \left(\frac{\omega}{\omega_o}\right)^{\alpha+\beta}}{\sqrt{\left(\frac{\omega}{\omega_o}\right)^{2(\alpha+\beta)} + \kappa_3^2 \left(\frac{\omega}{\omega_o}\right)^{2\beta} + \kappa_2^2 + 2\kappa_3 \left(\frac{\omega}{\omega_o}\right)^{\alpha+2\beta} \cos\left(\frac{\alpha\pi}{2}\right) + 2\kappa_2 \left(\frac{\omega}{\omega_o}\right)^{\alpha+\beta} \cos\left[\frac{(\alpha+\beta)\pi}{2}\right] + 2\kappa_2\kappa_3 \left(\frac{\omega}{\omega_o}\right)^\beta \cos\left(\frac{\beta\pi}{2}\right)}} \quad (2.46a)$$

$$\angle H(j\omega) = \angle \kappa_1 + \frac{(\alpha+\beta)\pi}{2} - \tan^{-1} \left(\frac{\left(\frac{\omega}{\omega_o}\right)^{\alpha+\beta} \sin\left[\frac{(\alpha+\beta)\pi}{2}\right] + \kappa_3 \left(\frac{\omega}{\omega_o}\right)^\beta \sin\left(\frac{\beta\pi}{2}\right)}{\left(\frac{\omega}{\omega_o}\right)^{\alpha+\beta} \cos\left[\frac{(\alpha+\beta)\pi}{2}\right] + \kappa_3 \left(\frac{\omega}{\omega_o}\right)^\beta \cos\left(\frac{\beta\pi}{2}\right) + \kappa_2} \right) \quad (2.46b)$$

The half-power (-3 dB) frequency (ω_h), defined as the frequency where there is a 0.707 drop of the passband gain, is calculated solving the equation given in (2.47). Also, the stopband attenuation gradient of the fractional-order high-pass filter of order $\alpha + \beta$ is equal to $6 \cdot (\alpha + \beta)$ dB/oct.

$$\begin{aligned} & \left(\frac{\omega_h}{\omega_o}\right)^{2(\alpha+\beta)} - 2\kappa_3 \left(\frac{\omega_h}{\omega_o}\right)^{\alpha+2\beta} \cos\left(\frac{\alpha\pi}{2}\right) - 2\kappa_2 \left(\frac{\omega_h}{\omega_o}\right)^{\alpha+\beta} \cos\left[\frac{(\alpha+\beta)\pi}{2}\right] \\ & - \kappa_3^2 \left(\frac{\omega_h}{\omega_o}\right)^{2\beta} - 2\kappa_2\kappa_3 \left(\frac{\omega_h}{\omega_o}\right)^\beta \cos\left(\frac{\beta\pi}{2}\right) - \kappa_2^2 = 0 \end{aligned} \quad (2.47)$$

2.5.3 Fractional-Order Band-Pass Filter (FBPF)

The transfer function of a FBPF is

$$H(s) = \kappa_1 \frac{\kappa_3 (\tau s)^\beta}{(\tau s)^{\alpha+\beta} + \kappa_3 (\tau s)^\beta + \kappa_2} \quad (2.48)$$

Using (2.48), the magnitude and phase response is expressed through the following equations:

$$|H(j\omega)| = \frac{\kappa_1 \kappa_3 \left(\frac{\omega}{\omega_0}\right)^\beta}{\sqrt{\left(\frac{\omega}{\omega_0}\right)^{2(\alpha+\beta)} + \kappa_3^2 \left(\frac{\omega}{\omega_0}\right)^{2\beta} + \kappa_2^2 + 2\kappa_3 \left(\frac{\omega}{\omega_0}\right)^{\alpha+2\beta} \cos\left(\frac{\alpha\pi}{2}\right) + 2\kappa_2 \left(\frac{\omega}{\omega_0}\right)^{\alpha+\beta} \cos\left[\frac{(\alpha+\beta)\pi}{2}\right] + 2\kappa_2 \kappa_3 \left(\frac{\omega}{\omega_0}\right)^\beta \cos\left(\frac{\beta\pi}{2}\right)}} \quad (2.49a)$$

$$\angle H(j\omega) = \angle \kappa_1 \kappa_3 + \frac{\beta\pi}{2} - \tan^{-1} \left(\frac{\left(\frac{\omega}{\omega_0}\right)^{\alpha+\beta} \sin\left[\frac{(\alpha+\beta)\pi}{2}\right] + \kappa_3 \left(\frac{\omega}{\omega_0}\right)^\beta \sin\left(\frac{\beta\pi}{2}\right)}{\left(\frac{\omega}{\omega_0}\right)^{\alpha+\beta} \cos\left[\frac{(\alpha+\beta)\pi}{2}\right] + \kappa_3 \left(\frac{\omega}{\omega_0}\right)^\beta \cos\left(\frac{\beta\pi}{2}\right) + \kappa_2} \right) \quad (2.49b)$$

The peak frequency (ω_p) is calculated solving the equation given in (2.49), which is derived from (2.48) with the condition: $\frac{d}{d\omega}|H(j\omega)|_{\omega=\omega_p} = 0$.

$$\alpha \left(\frac{\omega_p}{\omega_0}\right)^{2(\alpha+\beta)} + \alpha \kappa_3 \left(\frac{\omega_p}{\omega_0}\right)^{\alpha+2\beta} \cos\left(\frac{\alpha\pi}{2}\right) + (\alpha - \beta) \kappa_2 \left(\frac{\omega_p}{\omega_0}\right)^{\alpha+\beta} \cos\left[\frac{(\alpha+\beta)\pi}{2}\right] - \beta \kappa_2 \kappa_3 \left(\frac{\omega_p}{\omega_0}\right)^\beta \cos\left(\frac{\beta\pi}{2}\right) - \beta \kappa_2^2 = 0 \quad (2.50)$$

The quality factor of the filter is calculated according to the formula:

$$Q = \frac{\omega_p}{\omega_{h2} - \omega_{h1}} \quad (2.51)$$

where ω_{h2} and ω_{h1} are the upper and lower half-power frequencies, respectively.

Also, the stopband attenuation gradient at the upper frequencies is -6α dB/oct, while for the lower frequencies is $+6\beta$ dB/oct, offering the capability of realizing a FBPF with the stopband attenuation being varied in both frequency regions.

2.5.4 Fractional-Order Band-Stop Filter (FBSF)

A FBSF has the transfer function given by (2.52).

$$H(s) = \kappa_1 \frac{(\tau s)^{\alpha+\beta} + \kappa_2}{(\tau s)^{\alpha+\beta} + \kappa_3 (\tau s)^\beta + \kappa_2} \quad (2.52)$$

$$|H(j\omega)| = \kappa_1 \sqrt{\frac{\left(\frac{\omega}{\omega_0}\right)^{2(\alpha+\beta)} + 2\kappa_2\left(\frac{\omega}{\omega_0}\right)^{\alpha+\beta} \cos\left[\frac{(\alpha+\beta)\pi}{2}\right] + \kappa_2^2}{\left(\frac{\omega}{\omega_0}\right)^{2(\alpha+\beta)} + \kappa_3^2\left(\frac{\omega}{\omega_0}\right)^{2\beta} + \kappa_2^2 + 2\kappa_3\left(\frac{\omega}{\omega_0}\right)^{\alpha+2\beta} \cos\left(\frac{\alpha\pi}{2}\right)} + 2\kappa_2\left(\frac{\omega}{\omega_0}\right)^{\alpha+\beta} \cos\left[\frac{(\alpha+\beta)\pi}{2}\right] + 2\kappa_2\kappa_3\left(\frac{\omega}{\omega_0}\right)^\beta \cos\left(\frac{\beta\pi}{2}\right)} \quad (2.53a)$$

$$\begin{aligned} \angle H(j\omega) = & \angle \kappa_1 - \tan^{-1} \left(\frac{\left(\frac{\omega}{\omega_0}\right)^{\alpha+\beta} \sin\left[\frac{(\alpha+\beta)\pi}{2}\right]}{\left(\frac{\omega}{\omega_0}\right)^{\alpha+\beta} \cos\left[\frac{(\alpha+\beta)\pi}{2}\right] + \kappa_2} \right) \\ & - \tan^{-1} \left(\frac{\left(\frac{\omega}{\omega_0}\right)^{\alpha+\beta} \sin\left[\frac{(\alpha+\beta)\pi}{2}\right] + \kappa_3\left(\frac{\omega}{\omega_0}\right)^\beta \sin\left(\frac{\beta\pi}{2}\right)}{\left(\frac{\omega}{\omega_0}\right)^{\alpha+\beta} \cos\left[\frac{(\alpha+\beta)\pi}{2}\right] + \kappa_3\left(\frac{\omega}{\omega_0}\right)^\beta \cos\left(\frac{\beta\pi}{2}\right) + \kappa_2} \right) \end{aligned} \quad (2.53b)$$

The magnitude response and phase response are given by (2.53), while the peak frequency (ω_p) is calculated from (2.53) under the condition $\frac{d}{d\omega}|H(j\omega)|_{\omega=\omega_p} = 0$. The half-power (-3 dB) frequencies (ω_h) are calculated using the fact that at these frequencies there is a 0.707 drop of the passband gain which is equal to κ_1 . The quality factor of the filter is calculated from (2.51).

2.5.5 Design Equations for Generalized Filters of Order $\alpha + \beta$

Utilizing the second-order expression of the CFE given by (2.1) and substituting into (2.42), (2.45), (2.48), and (2.52) the derived transfer function for FLPF, FHFP, FBPF, and FBSF is the following:

$$H_{\alpha+\beta}(s) = \frac{\kappa_1}{D_4} \cdot \frac{N_4 s^4 + N_3 \frac{1}{\tau} s^3 + N_2 \frac{1}{\tau^2} s^2 + N_1 \frac{1}{\tau} s + N_0 \frac{1}{\tau^4}}{\left[s^4 + \left(\frac{D_3}{D_4}\right) \frac{1}{\tau} s^3 + \left(\frac{D_2}{D_4}\right) \frac{1}{\tau^2} s^2 + \left(\frac{D_1}{D_4}\right) \frac{1}{\tau} s + \frac{D_0}{D_4 \tau^4} \right]} \quad (2.54)$$

where the coefficients of the denominator D_i and nominator N_i ($i = 1, \dots, 4$) have been defined in (2.55), and Table 2.9, respectively.

$$\begin{aligned} D_0 &\equiv \alpha_2 b_2 + \kappa_3 \alpha_0 b_2 + \kappa_2 \alpha_0 b_0 \\ D_1 &\equiv \alpha_1 b_2 + \alpha_2 b_1 + \kappa_3 \alpha_1 b_2 + \kappa_3 \alpha_0 b_1 + \kappa_2 \alpha_1 b_0 + \kappa_2 \alpha_0 b_1 \\ D_2 &\equiv \alpha_0 b_2 + \alpha_0 b_1 + \alpha_2 b_0 + \kappa_3 \alpha_2 b_2 + \kappa_3 \alpha_1 b_1 + \kappa_3 \alpha_0 b_0 \\ &\quad + \kappa_2 \alpha_2 b_0 + \kappa_2 \alpha_1 b_1 + \kappa_2 \alpha_0 b_2 \\ D_3 &\equiv \alpha_0 b_1 + \alpha_1 b_0 + \kappa_3 \alpha_2 b_1 + \kappa_3 \alpha_1 b_0 + \kappa_2 \alpha_2 b_1 + \kappa_2 \alpha_1 b_2 \\ D_4 &\equiv \alpha_0 b_0 + \kappa_3 \alpha_2 b_0 + \kappa_2 \alpha_2 b_2 \end{aligned} \quad (2.55)$$

Table 2.9 Values of the coefficients of the nominator N_i ($i = 1, \dots, 4$) in (2.54) for realizing FLPF, FHFPF, FBPF, and FBSF of order $\alpha + \beta$

Filter	N_4	N_3	N_2	N_1	N_0
FLPF	$\alpha_2 b_2$	$\alpha_2 b_1 + \alpha_1 b_2$	$\alpha_2 b_0 + \alpha_1 b_1 + \alpha_0 b_2$	$\alpha_1 b_0 + \alpha_0 b_1$	$\alpha_0 b_0$
FHFPF	$\alpha_0 b_0$	$\alpha_1 b_0 + \alpha_0 b_1$	$\alpha_0 b_2 + \alpha_1 b_1 + \alpha_2 b_0$	$\alpha_1 b_2 + \alpha_2 b_1$	$\alpha_2 b_2$
FBPF	$\kappa_3 \alpha_2 b_0$	$\kappa_3 (\alpha_2 b_1 + \alpha_1 b_0)$	$\kappa_3 (\alpha_2 b_2 + \alpha_1 b_1 + \alpha_0 b_0)$	$\kappa_3 (\alpha_1 b_2 + \alpha_0 b_1)$	$\kappa_3 \alpha_0 b_2$
FBSF	$\alpha_2 b_0 + \kappa_2 \alpha_2 b_0$	$\alpha_0 b_1 + \alpha_1 b_0$ $+ \kappa_2 \alpha_2 b_1 + \kappa_2 \alpha_1 b_2$	$\alpha_0 b_2 + \alpha_1 b_1$ $+ \alpha_2 b_0 + \kappa_2 \alpha_2 b_0$ $+ \kappa_2 \alpha_1 b_1 + \kappa_2 \alpha_0 b_2$	$\alpha_1 b_2 + \alpha_2 b_1$ $+ \kappa_2 \alpha_1 b_0 + \kappa_2 \alpha_0 b_1$	$\alpha_2 b_2 + \kappa_2 \alpha_0 b_0$

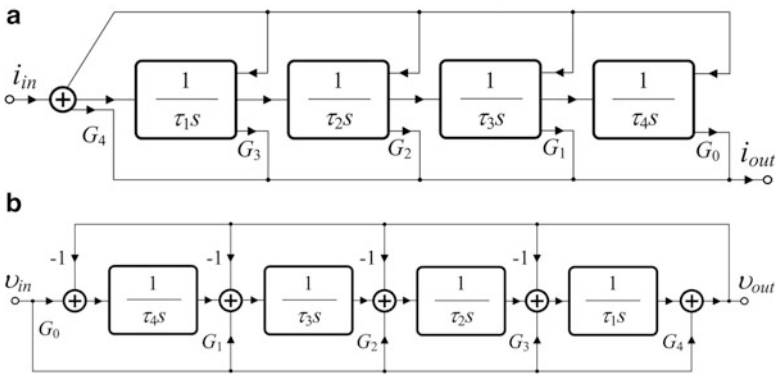


Fig. 2.4 FBD for realizing fractional FLPF, FHPF, FBPF, and FBSF of order $\alpha + \beta$ using (a) current mode topology, (b) voltage mode topology

Comparing the transfer functions of the FLPF and FHPF, it is easily derived that the numerator in $H_{HP}(s)$ is derived through the substitution $\alpha_0 \leftrightarrow \alpha_2$ and $b_0 \leftrightarrow b_2$ in the numerator of $H_{LP}(s)$. In a similar way, the numerator in $H_{BP}(s)$ is derived through the substitution $b_0 \leftrightarrow b_2$ in the numerator of $H_{LP}(s)$ multiplied by the factor κ_3 . Inspecting the transfer function given in (2.54), it is easily concluded that all of them were expressed by the same form, and consequently they could be realized by the same topology just by changing the coefficient values.

A suitable solution for this purpose is depicted in Fig. 2.4, where a typical FBD of a FLF topology and an IFLF topology are given in Fig. 2.4a and Fig. 2.4b, respectively. The realized transfer function is that given in (2.56).

Comparing the coefficients of (2.54) with those in (2.56), it is derived that the design equations about the time-constants τ_j ($j = 1, \dots, 4$) of all the filters and the corresponding design equation for the scaling factor G_i ($i = 0, \dots, 4$) are given in (2.57) and (2.58), respectively.

$$H(s) = \frac{G_4 s^4 + \frac{G_3}{\tau_1} s^3 + \frac{G_2}{\tau_1 \tau_2} s^2 + \frac{G_1}{\tau_1 \tau_2 \tau_3} s + \frac{G_0}{\tau_1 \tau_2 \tau_3 \tau_4}}{s^4 + \frac{1}{\tau_1} s^3 + \frac{1}{\tau_1 \tau_2} s^2 + \frac{1}{\tau_1 \tau_2 \tau_3} s + \frac{1}{\tau_1 \tau_2 \tau_3 \tau_4}} \quad (2.56)$$

$$\tau_j = \frac{D_{5-j}}{D_{4-j}} \cdot \tau \quad (2.57)$$

$$G_i = \kappa_1 \frac{N_i}{D_i} \quad (2.58)$$

where the values of the coefficients N_i are those given in Table 2.9, and depend on the desired filter function.

2.6 Fractional-Order Filters of Order $n + \alpha$

The procedure for realizing a high-order fractional filter of order $n + \alpha$ will be studied, where n is the integer-order of the filter and corresponds to values $n \geq 2$, and α is the order of the fractional part of the filter where $(0 < \alpha < 1)$. Such kind of filters exhibits stopband attenuation equal to $-6 \cdot (n + \alpha)$ dB/oct. The attenuation offered in the case of integer-order filters of order n , which is $-6 \cdot n$ dB/oct. Thus, low-pass, high-pass, band-pass, and band-stop filters of order $n + \alpha$ are presented, and two different design procedures are followed in order to realize these kinds of filters. According to [8, 9], the realization of a fractional-order filter of order $n + \alpha$ with Butterworth characteristics could be performed through the utilization of the polynomial ratio given by (2.59)

$$H_{n+\alpha}(s) = \frac{H_{1+\alpha}(s)}{B_{n-1}(s)} \quad (2.59)$$

where $H_{1+\alpha}(s)$ is the transfer function given by (2.23), (2.28), (2.32), (2.36) for realizing a FLPF, FHPF, FBPF, and FBSF, respectively, and $B_{n-1}(s)$ is the corresponding Butterworth polynomial of order $n-1$.

Some of these polynomials are the following:

$$\begin{aligned} B_1(s) &= s + 1 \\ B_2(s) &= s^2 + \sqrt{2}s + 1 \\ B_3(s) &= (s + 1)(s^2 + s + 1) \\ B_4(s) &= (s^2 + 0.7654s + 1)(s^2 + 1.8478s + 1) \\ B_5(s) &= (s + 1)(s^2 + 0.618s + 1)(s^2 + 1.618s + 1) \end{aligned} \quad (2.60)$$

The gain response of the $(n + \alpha)$ filter is that given in (2.61)

$$|H_{n+\alpha}(\omega)| = \frac{1}{\sqrt{\left[1 + \left(\frac{\omega}{\omega_o}\right)^{2(1+\alpha)}\right] \cdot \left[1 + \left(\frac{\omega}{\omega_o}\right)^{2(n-1)}\right]}} \quad (2.61)$$

Performing a routine algebraic procedure it is derived from (2.61) that

$$\left(\frac{\omega_h}{\omega_o}\right)^{2(n+\alpha)} + \left(\frac{\omega_h}{\omega_o}\right)^{2(n-1)} + \left(\frac{\omega_h}{\omega_o}\right)^{2(1+\alpha)} - 1 = 0 \quad (2.62)$$

2.6.1 Design Equations for Generalized Filters of Order $n + \alpha$

Utilizing the second-order expression of the CFE given by (2.1) and using the expressions in (2.39), then from (2.59) it is obtained that the general forms of the transfer functions will be the following:

$$H_{n+\alpha}^{\text{LP}}(s) = \frac{\kappa_1}{\alpha_0} \cdot \frac{\alpha_2 \frac{1}{\tau^n} s^2 + \alpha_1 \frac{1}{\tau^{n+1}} s + \alpha_0 \frac{1}{\tau^{n+2}}}{\left[s^{n+2} + \beta_{n+1} \frac{1}{\tau} s^{n+1} + \dots + \beta_1 \frac{1}{\tau^{n+1}} s + \beta_0 \frac{1}{\tau^{n+2}} \right]} \quad (2.63a)$$

$$H_{n+\alpha}^{\text{HP}}(s) = \frac{\kappa_1}{\alpha_0} \cdot \frac{\alpha_0 \frac{1}{\tau^{n-1}} s^3 + \alpha_1 \frac{1}{\tau^n} s^2 + \alpha_2 \frac{1}{\tau^{n+1}} s}{\left[s^{n+2} + \beta_{n+1} \frac{1}{\tau} s^{n+1} + \dots + \beta_1 \frac{1}{\tau^{n+1}} s + \beta_0 \frac{1}{\tau^{n+2}} \right]} \quad (2.63b)$$

$$H_{n+\alpha}^{\text{BP}}(s) = \frac{\kappa_1 \kappa_3}{\alpha_0} \cdot \frac{\alpha_0 \frac{1}{\tau^n} s^2 + \alpha_1 \frac{1}{\tau^{n+1}} s + \alpha_2 \frac{1}{\tau^{n+2}}}{\left[s^{n+2} + \beta_{n+1} \frac{1}{\tau} s^{n+1} + \dots + \beta_1 \frac{1}{\tau^{n+1}} s + \beta_0 \frac{1}{\tau^{n+2}} \right]} \quad (2.63c)$$

$$H_{n+\alpha}^{\text{BS}}(s) = \frac{\kappa_1}{\alpha_0} \cdot \frac{\alpha_0 \frac{1}{\tau^{n-1}} s^3 + (\alpha_1 + \kappa_2 \alpha_2) \frac{1}{\tau^n} s^2 + (\alpha_2 + \kappa_2 \alpha_1) \frac{1}{\tau^{n+1}} s + \kappa_2 \alpha_0 \frac{1}{\tau^{n+2}}}{\left[s^{n+2} + \beta_{n+1} \frac{1}{\tau} s^{n+1} + \dots + \beta_1 \frac{1}{\tau^{n+1}} s + \beta_0 \frac{1}{\tau^{n+2}} \right]} \quad (2.63d)$$

where β_κ ($\kappa = 0, 1, \dots, n+1$) is a function of α_i , which is a result of multiplication of the denominator of $H_{1+\alpha}(s)$ in (2.39) and the coefficients of $B_{n-1}(s)$.

Inspecting the transfer functions of FLPF, FHFPF, FBPF, and FBSF, it is concluded that all of them have the same form. Consequently they could be realized by the same topology just by changing the coefficient values. A suitable solution for this purpose is depicted in Fig. 2.5, where a typical FBD of a FLF topology and an IFLF topology are given in Fig. 2.5a and Fig. 2.5b, respectively.

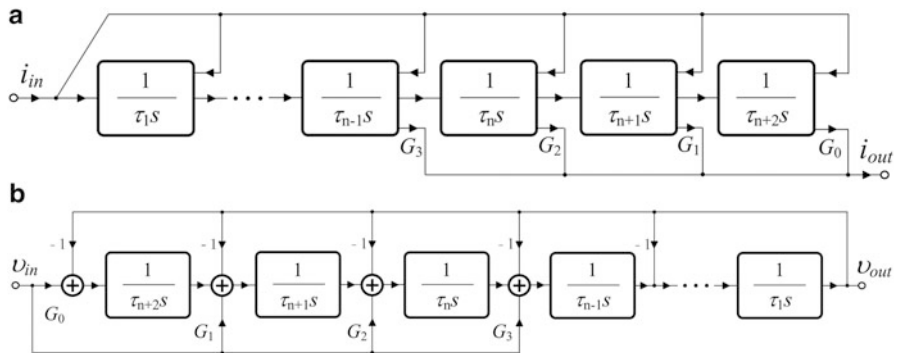


Fig. 2.5 FBD for realizing FLPF, FHFPF, FBPF, and FBSF of order $n + \alpha$ using $B_{n-1}(s)$ Butterworth polynomials (a) current mode topology, (b) voltage mode topology

Table 2.10 Values of scaling factors G_i for realizing FLPF, FHPF, FBPF, and FBSF in Fig. 2.5 of order $n + \alpha$

Filter	G_3	G_2	G_1	G_0
FLPF	0	$\frac{\kappa_1 \alpha_2}{\alpha_0 \beta_2}$	$\frac{\kappa_1 \alpha_1}{\alpha_0 \beta_1}$	$\frac{\kappa_1}{\beta_0}$
FHPF	κ_1	$\frac{\kappa_1 \alpha_1}{\alpha_0 \beta_2}$	$\frac{\kappa_1 \alpha_2}{\alpha_0 \beta_1}$	0
FBPF	0	$\frac{\kappa_1 \kappa_3}{\beta_2}$	$\frac{\kappa_1 \kappa_3 \alpha_1}{\alpha_0 \beta_1}$	$\frac{\kappa_1 \kappa_3 \alpha_2}{\alpha_0 \beta_0}$
FBSF	$\frac{\kappa_1}{\beta_3}$	$\frac{\kappa_1 (\alpha_1 + \kappa_2 \alpha_2)}{\alpha_0 \beta_2}$	$\frac{\kappa_1 (\alpha_2 + \kappa_2 \alpha_1)}{\alpha_0 \beta_1}$	$\frac{\kappa_1 \kappa_2}{\beta_0}$

The realized transfer function is that given in (2.64). Comparing the coefficients of (2.64) with these of FLPF, FHPF, and FBSF it is derived that, under the assumption that $\beta_{n+2} = 1$, the design equations about the time-constants τ_j ($j = 1, 2, \dots, n + 2$) of all the filters are given in (2.65). The corresponding design equations for the scaling factors G_i ($i = 0, \dots, 3$) are summarized in Table 2.10.

$$H_{n+\alpha}(s) = \frac{\frac{G_3}{\tau_1 \cdots \tau_{n-1}} s^3 + \frac{G_2}{\tau_1 \cdots \tau_n} s^2 + \frac{G_1}{\tau_1 \cdots \tau_{n+1}} s + \frac{G_0}{\tau_1 \cdots \tau_{n+2}}}{s^{n+2} + \frac{1}{\tau_1} s^{n+1} + \frac{1}{\tau_1 \tau_2} s^n + \cdots + \frac{1}{\tau_1 \tau_2 \cdots \tau_{n+2}}} \quad (2.64)$$

$$\tau_j = \frac{\beta_{n+3-j}}{\beta_{n+2-j}} \cdot \tau \quad (2.65)$$

In case time-constants are to be expressed as a function of the desired half-power frequency (ω_h), then the above equation could be modified as

$$\tau_j = \frac{\beta_{n+3-j}}{\beta_{n+2-j}} \cdot \left(\frac{\omega_h}{\omega_o} \right) \quad (2.66)$$

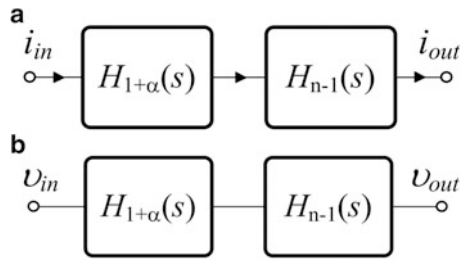
Taking into account the fact that all the aforementioned procedure is somewhat complicated due to the algebraic calculation of the coefficients β_κ especially in case of high-order filters. Thus, an alternative solution for realizing high-order fractional filters is through the cascade connection of $1 + \alpha$ and $n-1$ order filters, which is expressed in the following equation as

$$H_{n+\alpha}(s) = H_{1+\alpha}(s) \cdot H_{n-1}(s) \quad (2.67)$$

where $H_{n-1}(s) = 1/B_{n-1}(s)$ is the transfer function of the $n-1$ order Butterworth filter, the derivation of which is a trivial procedure.

A suitable topology for this purpose is depicted in Fig. 2.6, from which is obvious that having available the topology of an $1 + \alpha$ order filter and an integer-order filter of an $n-1$ order filter, it is readily obtained that one additional step is required for realizing an $n + \alpha$ order fractional filter.

Fig. 2.6 FBD for realizing FLPF, FHPF, FBPF, and FBSF of order $n + \alpha$ using $(n-1)$ Butterworth filter **(a)** current-mode topology, **(b)** voltage-mode topology



The gain response of the filter is that given in (2.68), where ω_{o1} and ω_{o2} are the -3 dB frequencies of the $1 + \alpha$ and $n-1$ order filters, respectively.

$$|H_{n+\alpha}(\omega)| = \frac{1}{\sqrt{1 + \left(\frac{\omega}{\omega_{o1}}\right)^{2(1+\alpha)}}} \cdot \frac{1}{\sqrt{1 + \left(\frac{\omega}{\omega_{o2}}\right)^{2(n-1)}}} \quad (2.68)$$

Performing a routine algebraic procedure it is derived from (2.68) that

$$\left(\frac{\omega_h}{\omega_{o1}}\right)^{2(1+\alpha)} \cdot \left(\frac{\omega_h}{\omega_{o2}}\right)^{2(n-1)} + \left(\frac{\omega_h}{\omega_{o2}}\right)^{2(n-1)} + \left(\frac{\omega_h}{\omega_{o1}}\right)^{2(1+\alpha)} - 1 = 0 \quad (2.69)$$

Taking into account that ω_{o1} and ω_{o2} are selected to be the same and equal to ω_o , then (2.69) is simplified to (2.62).

2.7 Summary

Fractional-order differentiation/integrator blocks and fractional order generalized filters have been realized in this section, through the utilization of the CFE, which enables the opportunity of realizing all the aforementioned topologies through integer-order counterparts which is a trivial procedure. Each category has been performed by using a general form, offering the capability of implementing various types of transfer functions without modifying their core, which is very important from the design flexibility point of view. Having available all this procedure, then it is easy to realize every kind of the aforementioned fractional-order circuits using the suitable or desirable way of implementing the integer-order counterparts (i.e., integrators), which thereafter depends on the designer choice. They could be realized either using a current mode procedure using for example current-mirrors, or a voltage mode using OTAs. Some of these implementations will be described and realized in detail in the next sessions.

References

1. Abdelliche, F., Charef, A.: R-peak detection Using a complex fractional wavelet. In: Proceedings of the IEEE International Conference on Electrical and Electronics Engineering (ELECO), pp. 267–270 (2009)
2. Abdelliche, F., Charef, A., Talbi, M., Benmalek, M.: A fractional wave-let for QRS detection. *IEEE Inf. Commun. Technol.* **1**(2), 1186–1189 (2006)
3. Ferdi, Y., Hebeval, J., Charef, A., Boucheham, B.: R wave detection using fractional digital differentiation. *ITBMRBM.* **24**(5–6), 273–280 (2003)
4. Goutas, A., Ferdi, Y., Herbeval, J.P., Boudraa, M., Boucheham, B.: Digital fractional order differentiation-based algorithm for P and T-waves detection and delineation. *Int. Arab. J. Inf. Technol.* **26**(2), 127–132 (2005)
5. Benmalek, M., Charef, A.: Digital fractional order operators for R-wave detection in electrocardiogram signal. *IET Signal Process.* **3**(5), 381–391 (2009)
6. Radwan, A., Soliman, A., Elwakil, A.: First-order filters generalized to the fractional domain. *J. Circuits Syst. Comput.* **17**(1), 55–66 (2008)
7. Tsirimokou, G., Psychalinos, C.: Ultra-low voltage fractional-order differentiator and integrator topologies: an application for handling noisy ECGs. *Analog Integr. Circ. Sig. Process.* **81**(2), 393–405 (2014)
8. Maundy, B., Elwakil, A., Freeborn, T.: On the practical realization of higher-order filters with fractional stepping. *Signal Process.* **91**(3), 484–491 (2011)
9. Freeborn, T., Maundy, B., Elwakil, A.: Field programmable analogue array implementation of fractional step filters. *IET Circuits Devices Syst.* **4**(6), 514–524 (2010)
10. Ortigueira, M.: An introduction to the fractional continuous-time linear systems: the 21st century systems. *IEEE Circuits Syst. Mag.* **8**(3), 19–26 (2008)
11. Elwakil, A.: Fractional-order circuits and systems: an emerging interdisciplinary research area. *IEEE Circuits Syst. Mag.* **10**(4), 40–50 (2010)
12. Biswas, K., Sen, S., Dutta, P.: Realization of a constant phase element and its performance study in a differentiator circuit. *IEEE Trans. Circuits Syst. II Express Briefs.* **53**(9), 802–806 (2006)
13. Krishna, B., Reddy, K.: Active and passive realization of fractance device of order $\frac{1}{2}$. *Act. Passive Electron. Compon.* **2008**, Article ID 369421 (2008)
14. Radwan, A., Elwakil, A., Soliman, A.: On the generalization of second-order filters to the fractional-order domain. *J. Circuits Syst. Comput.* **18**(2), 361–386 (2009)
15. Freeborn, T., Maundy, B., Elwakil, A.: Towards the realization of fractional step filters. In: Proceedings of IEEE International Symposium on Circuits and Systems (ISCAS), pp. 1037–1040 (2010)
16. Mondal, D., Biswas, K.: Performance study of fractional order integra-tor using single-component fractional order element. *IET Circuits Devices Syst.* **5**(4), 334–342 (2011)
17. Radwan, A., Salama, K.: Fractional-order RC and RL circuits. *Circuits Syst. Signal Process.* **31**(6), 1901–1915 (2012)
18. Ahmadi, P., Maundy, B., Elwakil, A., Belostotski, L.: High-quality fac-tor asymmetric-slope band-pass filters: a fractional-order capacitor approach. *IET Circuits Devices Syst.* **6**(3), 187–197 (2012)
19. Ali, A., Radwan, A., Soliman, A.: Fractional order Butterworth filter: active and passive realizations. *IEEE J. Emerging Sel. Top. Circuits Syst.* **3**(3), 346–354 (2013)

Chapter 3

Current-Mode Fractional-Order Filters

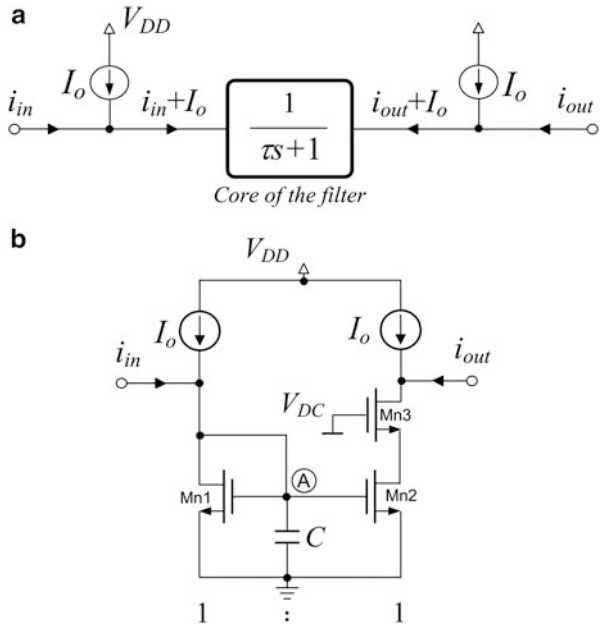
3.1 Introduction

The design of analog integrated circuits which are able to operate in a low-voltage environment is an imperative need that has been extremely increased. The aforementioned feature constitutes a difficult procedure especially when the IC designs should be able to operate not only in a low-voltage environment, but also providing high performance under these conditions. This could be easily achieved by using the current-mode technique, which have the benefit of overcoming the gain-bandwidth product limitation, and that the intermediate nodes have low impedance. Thus, small variations of current correspond to small variations of voltages. Current-mode circuits constitute the complementary of voltage-mode circuits, where the input-output and intermediate signals are currents. Also, the majority of these topologies are very simple structures offering the advantage of extremely reduced circuit complexity.

3.2 Basic Building Blocks

Current-mirrors constitute attractive building blocks which under special conditions are appropriate for biomedical applications. Taking into account that biological signals lie in low frequency range, the realization of circuits with large-time constants is necessary for this type of systems. Due to the fact that the time-constants are given by the expression $\tau = C/g_m$, where g_m is the small-signal transconductance of the input MOS transistor which is depended on the level of the bias current I_o . The large time-constants could be achieved by increasing the value of capacitance [1–3] and/or reducing the value of g_m through an appropriate adjustment of the bias current.

Fig. 3.1 Typical first-order filter using current-mirror
(a) FBD representation and
(b) typical circuitry



As it has been already mentioned, the reduction of transconductance could be achieved through a reduction of the related dc bias current I_o . Taking into account the class-A nature of the current-mirror filters, the level of the input current should be smaller than that of the bias current (i.e., $i_{in} \leq I_o$). Therefore, this solution dramatically limits the range of the input currents, which could be successfully handled by the filter. Thus, an alternative solution for realizing large time-constants is the employment of appropriate linear compression and expansion of the input and output currents, respectively.

A typical FBD of a current-mode first-order low-pass filter is as shown in Fig. 3.1a, with the corresponding current-mirror realization depicted in Fig. 3.1b [4]. The transfer function is that given by (3.1)

$$\frac{i_{out}}{i_{in}} = \frac{1}{\tau \cdot s + 1} \quad (3.1)$$

where τ is the time-constant, given by

$$\tau = \frac{C}{g_{m,Mn1}} \quad (3.2)$$

where $g_{m,Mn1}$ is the small-signal transconductance parameter of M_{n1} .

Assuming that MOS transistors operate in the subthreshold region, the expression of time-constant is the following:

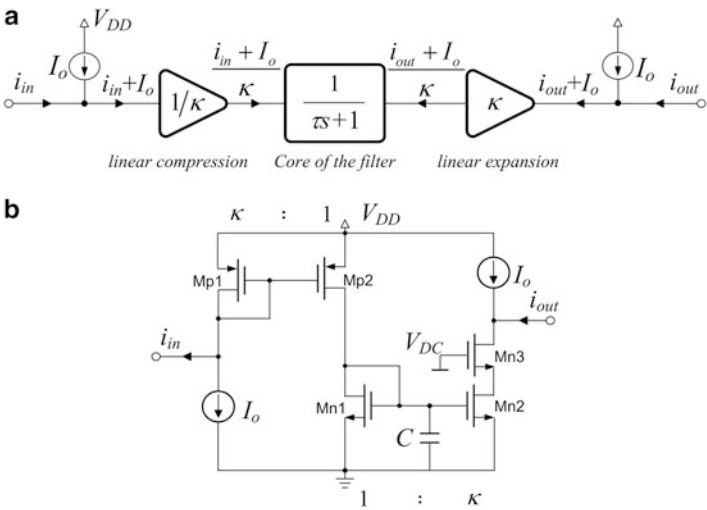


Fig. 3.3 Lossy integrator with large-time constant realization capability (a) FBD representation and (b) current-mirror realization

$(i_{in} + I_o/\kappa)$. Thus, a linear compression of the instantaneous value of the input current is performed.

Therefore, according to (3.3), the realized value of time-constant is increased by a factor κ . The aspect ratio of M_{n2} is also scaled by a factor κ as shown in Fig. 3.3 in order to achieve a low-frequency gain equal to one, and perform the linear expansion of the output current. As a result, the realized time-constant is given by

$$\tau = \kappa \cdot \frac{CnV_T}{I_o} \quad (3.4)$$

An important benefit that should be also mentioned is the fact that the achieved scaling factor does not affect the level of the maximum current that could be handled by the filter and this is very important from the design flexibility point of view.

Taking into account that the realization of large-time constant has been achieved just by adding two transistors, the total power dissipation will be increased from its initial value $2V_{DD}I_o$ to $[2 + (1/\kappa)]V_{DD}I_o$, while the solution derived using the extra block in Fig. 3.2 leads to a configuration with an extra number of five transistors and a total power dissipation $(3 + \kappa)V_{DD}I_o$. As a result, the proposed solution is the most attractive in terms of circuit complexity and power dissipation.

The topology of the corresponding lossless integrator is given in Fig. 3.4, where the realized transfer function is given by (3.5), while the time-constant is still given by the expression in (3.4)

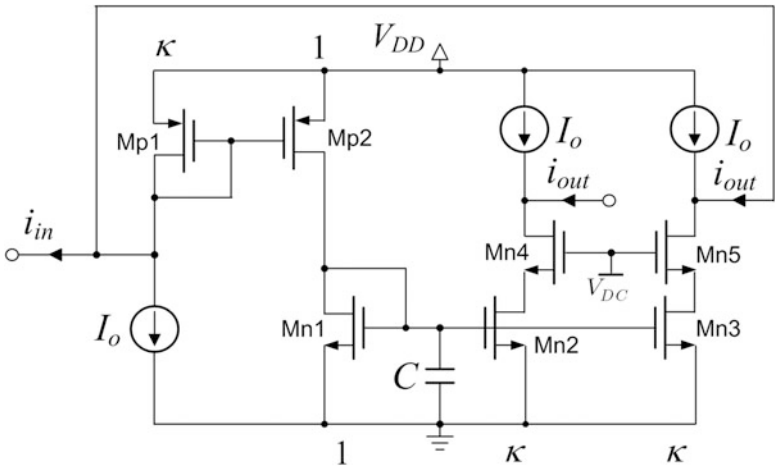
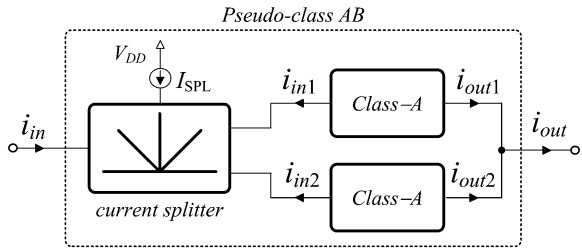


Fig. 3.4 Lossless integrator with large time-constant realized using current mirrors

Fig. 3.5 A pseudo-class AB system realization



$$\frac{i_{out}}{i_{in}} = \frac{1}{\tau \cdot s} \quad (3.5)$$

Finally, the only restriction that should be fulfilled using the proposed technique is the fact that the amplitude range of the input signal should be $i_{in} \leq I_o$, and this is originated from the inherent class-A nature of the integrator. In order to overcome this drawback, a pseudo-class AB could be constructed using the FBD in Fig. 3.5, which is constructed from two identical class-A paths, which are fed by the always-positive output currents of current splitter.

The realization of the current splitter in a transistor level is depicted in Fig. 3.6, where the expressions for its output currents are given by

$$i_{in1} = \frac{i_{in} + \sqrt{i_{in}^2 + 4I_B^2}}{2} \quad (3.6)$$

$$i_{in2} = \frac{-i_{in} + \sqrt{i_{in}^2 + 4I_B^2}}{2} \quad (3.7)$$

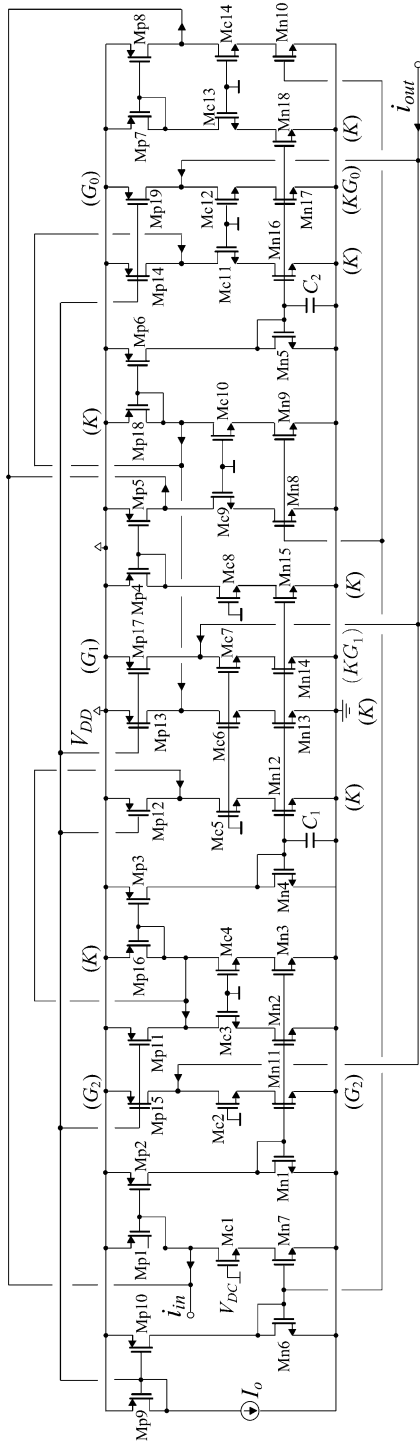


Fig. 3.7 Realization of fractional-order differentiator, lossless and lossy integrator of order α , using current-mirrors with large time-constants

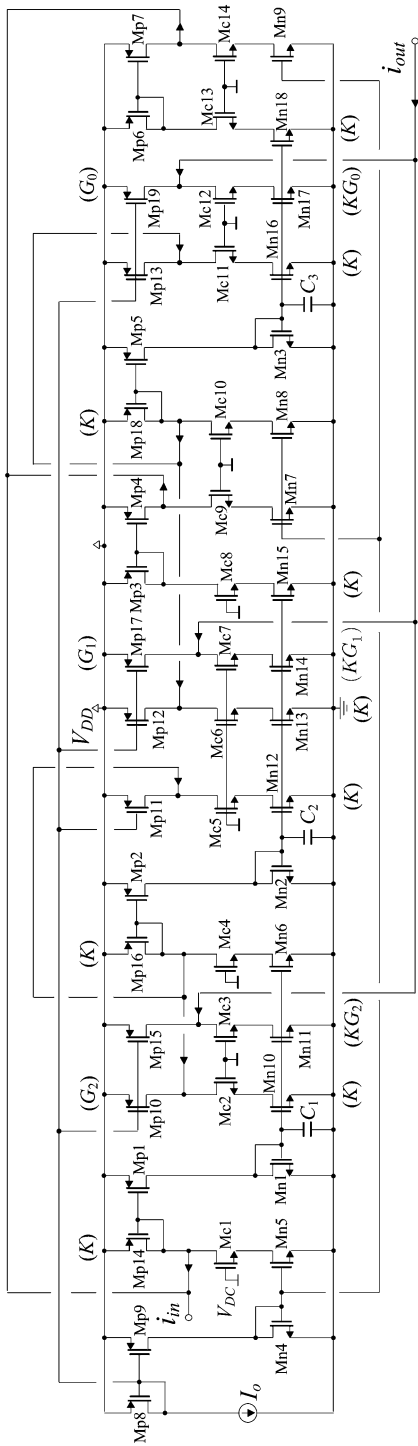


Fig. 3.8 Realization of fractional-order low-pass filter of order $1 + \alpha$, using current-mirrors with large time-constants

3.4 Simulation and Comparison Results

3.4.1 First-Order Filter Using Current Mirrors with Large Time-Constants

The performance of the filter in Fig. 3.3 has been evaluated using the Analog Design Environment of the Cadence software and the Design kit provided by the TSMC 180 nm CMOS process. The employed dc bias voltage scheme was $V_{DD} = 0.5$ V and $V_{DC} = 300$ mV, while the dc bias current was $I_o = 3$ nA which corresponds to a transconductance level equal to 88.7 nS. In order to realize a low-pass filter with cutoff frequency $f_o = 10$ Hz, the required capacitor value will be equal to 1.41 nF, which is a nonrealistic value from the integration point of view.

The utilization of the proposed solution where a scaling factor $\kappa = 30$ is achieved, the required time-constant could be realized by considering a capacitor equal to 47.1 pF. The aspect ratios of transistors were $10 \mu\text{m}/5 \mu\text{m}$ for M_{n1} , $20 \mu\text{m}/5 \mu\text{m}$ for M_{n3} , and $5.6 \mu\text{m}/2 \mu\text{m}$ for M_{p2} . The distribution of dc current has been performed using nMOS and pMOS current mirrors with aspect ratio $5 \mu\text{m}/5 \mu\text{m}$ and $10 \mu\text{m}/5 \mu\text{m}$, respectively.

The simulated results of the first-order filter in Fig. 3.3 for bias current being tuned at values $I_o = 1.5, 3,$ and 6 nA are demonstrated in Fig. 3.9.

The derived cutoff frequencies were 5.04 Hz, 9.6 Hz, and 18.7 Hz, respectively, which are very close to the corresponding theoretical values 5 Hz, 10 Hz, and 20 Hz.

The linear performance of the filter in Fig. 3.3 is obtained through the Periodic Steady State (PSS) analysis of the Analog Design Environment, while the noise was integrated through the passband of the filter. In addition, the sensitivity of the frequency characteristics of the filter, with respect to the MOS transistor

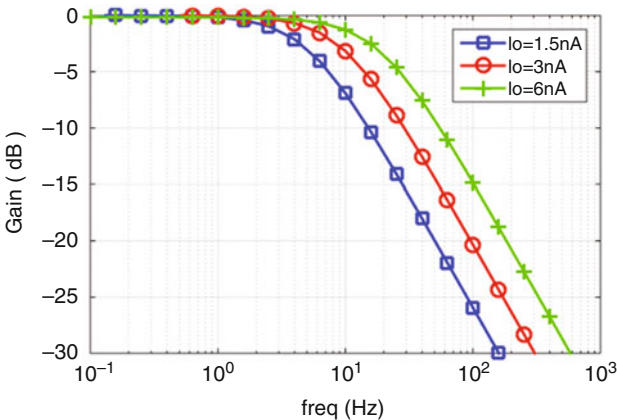


Fig. 3.9 Frequency response of the first-order low-pass filter in Fig. 3.3

Table 3.1 Performance factors for the filter in Fig. 3.3 and compared with that in Fig. 3.1

Performance factor	Fig. 3.1	Fig. 3.3 ($\kappa = 30$)
Power (nW) @ $V_{DD}V_{DD} = 0.5$ V	3	3.05
Cutoff frequency f_o (Hz)	9.4	9.6
Amplitude (nA) @ THD 2%	2.96	2.91
Input referred noise (pA)	0.47	1.2
Dynamic Range (dB)	73	64.7
Transistor area (μm^2)	300	2072.2
Capacitor area (μm^2)	670,884	22,363
Standard deviation of gain	12.4 m	29.3 m
Standard deviation of f_o (Hz)	0.17	0.34

mismatching and process variations, has been evaluated through the Monte Carlo analysis offered by the Analog Design Environment.

The obtained results showing the total performance of the filter in Fig. 3.3 are summarized in Table 3.1, where the corresponding factors for the filter in Fig. 3.1 are also given. It should be mentioned at this point that the power dissipation for the scheme derived from the solution in Fig. 3.3 would be 49.5 nA and this makes its employment not attractive in low-power applications. According to the derived results, the proposed solution offers the benefits of significant reduction (about 27 times) of the total silicon area in comparison with that required in the case of the topology in Fig. 3.2.

The price paid is that the dynamic range of the filter has been reduced due to the increased rms value of the noise; in addition, the sensitivity of the circuit has been also increased.

3.4.2 Fractional-Order Circuits Using Current Mirrors with Large Time-Constants

As a first step, a differentiator with order $\alpha = 0.5$ and unity gain frequency $f_o = 10$ Hz will be designed. This will be achieved by using the topologies in Figs. 3.1, 3.3, and 3.4 in order to realize the FBD in Fig. 2.1a. The resulted topology is that demonstrated in Fig. 3.7. There should be mentioned that the proposed topology is able to realize also fractional-order lossless and lossy integrators of order α , just by calculating the appropriate design equations given in Tables 2.1 and 2.2, combined with Eq. (3.4).

Considering that $I_o = 300$ pA, then using the design equations provided in Tables 2.1 and 2.2, and Eq. (3.4) for $\kappa = 6$, the values of capacitors have been calculated as $C_1 = 2.36$ pF and $C_2 = 47.2$ pF. In addition, the scaling factors G_i ($i = 0, 1, 2$) were $G_2 = 5$, $G_1 = 1$, and $G_0 = 0.2$. Considering MOS transistors biased at the subthreshold region, the power supply voltage was $V_{DD} = 0.5$ V, while the dc voltage required for biasing the cascade transistors was $V_{DC} = 350$ mV. The

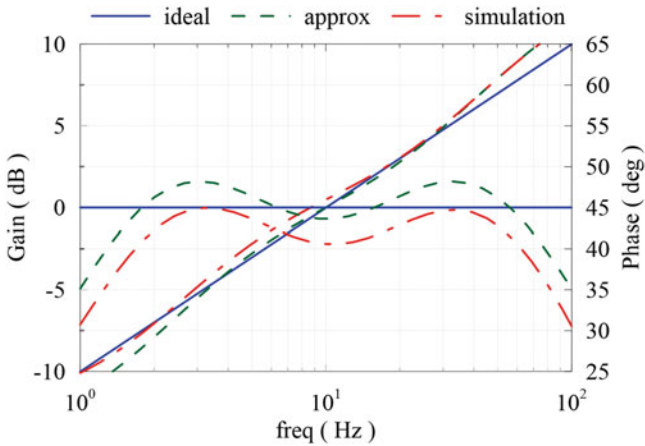


Fig. 3.10 Magnitude and phase responses of a fractional-order differentiator ($\alpha = 0.5$) derived by the topology in Fig. 3.7

aspect ratios of transistors are $5 \mu\text{m}/10 \mu\text{m}$ for $M_{n1}-M_{n5}$, $4 \mu\text{m}/10 \mu\text{m}$ for $M_{n6}-M_{n10}$, $10 \mu\text{m}/1 \mu\text{m}$ for $M_{c1}-M_{c14}$, $2 \mu\text{m}/4 \mu\text{m}$ for $M_{p1}-M_{p8}$, and $4 \mu\text{m}/5 \mu\text{m}$ for $M_{p9}-M_{p14}$.

The simulated magnitude and phase responses are given in Fig. 3.10, where the corresponding theoretically predicted plots (dashed lines) are also provided. The unity-gain frequency was 8.8 Hz. According to these plots, the differentiator approximates the ideal response with a phase error smaller than 5° within the bandwidth $\text{BW} = 62.7 \text{ Hz} - 1.7 \text{ Hz} = 61 \text{ Hz}$. The dc power dissipation of the differentiator was $P = 2.98 \text{ nW}$.

Thus, the normalized power dissipation, defined as $P_{\text{norm}} = P/(f_o \cdot \text{BW})$, will be equal to 4.88 pJ . Taking into account that the corresponding Sinh-Domain counterpart introduced in [5] has power dissipation equal to 8.33 nW and $\text{BW} = 162.50 \text{ Hz} - 1.27 \text{ Hz} = 161.23 \text{ Hz}$ (at an accuracy level smaller than 5°), the corresponding value of P_{norm} will be equal to 5.16 pJ .

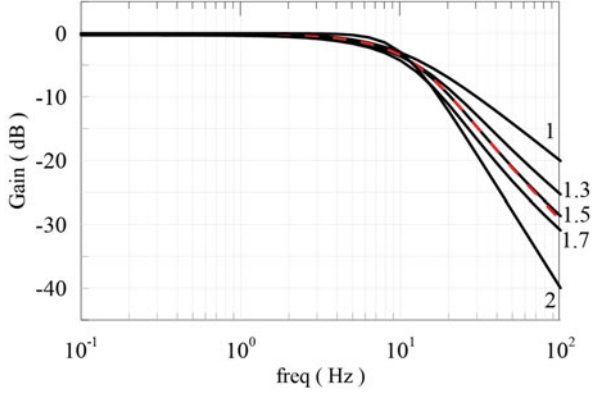
Consequently, the proposed fractional-order differentiator offers a more power efficient design than that introduced in [5]. In addition, the total capacitance for the proposed differentiator was 49.56 pF , while for that in [5] 400 pF . Thus, another important feature offered by the proposed topology is the significant reduction of the total occupied silicon area.

The realization of the FBD in Fig. 2.3a using the aforementioned concept is demonstrated in Fig. 3.8, which will be employed for realizing low-pass filter functions, of order $n + \alpha = 1.3, 1.5,$ and 1.7 , with Butterworth (all-pole) frequency characteristics. Assuming cutoff frequency $f_o = 10 \text{ Hz}$ and bias current $I_o = 105 \text{ pA}$, the values of capacitors, calculated according to (3.4), and (2.40) for $K = 2.5$, are given in Table 3.2. Also, the scaling factors according to Table 2.8 using the approximation in (1.6) are given in Table 3.2. The aspect ratios of MOS transistors of the filter in Fig. 3.8 are $5 \mu\text{m}/10 \mu\text{m}$ for $M_{n1}-M_{n3}$, $4 \mu\text{m}/10 \mu\text{m}$ for $M_{n4}-M_{n9}$, $10 \mu\text{m}/1 \mu\text{m}$ for $M_{c1}-M_{c14}$, $2 \mu\text{m}/4 \mu\text{m}$ for $M_{p1}-M_{p7}$, and $4 \mu\text{m}/5 \mu\text{m}$ for $M_{p8}-M_{p13}$.

Table 3.2 Values of capacitances and scaling factors for the $1 + \alpha$ order FLPF in Fig. 3.8, derived according to the approximation in (1.6)

	$\alpha = 0.3$	$\alpha = 0.5$	$\alpha = 0.7$
G_2	0.117	0.07	0.033
G_1	0.7	0.61	0.515
G_0	1.010	1.005	1
C_1 (pF)	5.8	6.94	7.68
C_2 (pF)	18.1	17.2	17.2
C_3 (pF)	74.7	65.2	58.8

Fig. 3.11 Simulated frequency responses of the low-pass filter ($n + \alpha = 1.3, 1.5, \text{ and } 1.7$)



The obtained frequency responses are demonstrated in Fig. 3.11. The cutoff frequency was 8.97, 9, and 8.5 Hz at orders 1.3, 1.5, and 1.7, respectively. The corresponding values of the slope of the stopband attenuation were -7.3 (-24.2), -8.6 (-28.6), and -9.23 (-30.7) dB/oct (dB/dec), while the theoretically predicted values were -7.8 (-26), -9 (-30), and -10.2 (-34) dB/oct (dB/dec), respectively.

The linear performance of the topology in Fig. 3.8 has been evaluated in the case that $n = 1.5$. For this purpose, a stimulus with 0.1 Hz frequency and variable amplitude has been utilized. The total harmonic distortion (THD) was equal to 2% at an input level equal to 112pA. The noise has been integrated within the passband of the filter and the rms value of the input referred noise was 0.55pA. Thus, the value of the Dynamic Range (DR) of the filter will be 43.1 dB.

The sensitivity of the filter with respect to the effect of MOS transistor parameters mismatching as well as the process parameters variations has been evaluated through the Monte Carlo analysis offered by the analog Design Environment. The obtained statistical results about the standard deviation of low-frequency gain, cutoff frequency, and slope of the stopband attenuation, for a number $N = 100$ runs, were 0.1, 1.2 Hz, and 0.36 dB/oct, respectively.

The power efficiency of the proposed fractional-order low-pass filter could be further enhanced through the utilization of the FBD as given in Fig. 3.5, which corresponds into a pseudo class-AB circuit topology. It is constructed from a current-splitter topology and two identical class-A paths. A current-splitter topology is depicted in Fig. 3.6; the output currents are given by (3.6) and (3.7), respectively.

Table 3.3 Performance evaluation results of the proposed fractional-order ($n + \alpha = 1.5$) low-pass filter topologies

Performance factor	[5]	Fig. 3.8 (Class-A)	Fig. 3.8 (Class-AB)
Power (nW) @ $V_{DD} = 0.5$ V	5.80	0.82	2.05
Total capacitance (pF)	180	90	180
Low-frequency gain	0.94	0.98	0.98
Total active silicon area (μm^2)	13,213	1531	6502
Total passive silicon area (μm^2)	84,884	42,442	84,884
Cutoff frequency f_o (Hz)	11	9	9.5
Slope (dB/oct)	-9.7	-8.6	-8.8
Amplitude (pA) @ THD 2%	897	112	1710
Input referred noise (pA)	0.34	0.55	0.29
Dynamic Range (dB)	65.40	43.15	72.4
FoM (pJ)	0.21	0.38	0.03
St.d of low-frequency gain	0.05	0.1	0.13
St.d of cutoff frequency (Hz)	1.5	1.2	0.75
St.d of slope (dB/oct)	0.34	0.36	0.26

Considering that the splitter operates under $V_{DD} = 0.5$ V and $V_{DC} = 350$ mV power supply voltages and dc bias current $I_{o,s} = 105$ pA, the aspect ratios of MOS transistors are $5 \mu\text{m}/10 \mu\text{m}$ for M_{n1} – M_{n3} , $4 \mu\text{m}/10 \mu\text{m}$ for M_{n4} – M_{n9} , $10 \mu\text{m}/1 \mu\text{m}$ for M_{c1} – M_{c14} , $2 \mu\text{m}/4 \mu\text{m}$ for M_{p1} – M_{p7} , and $4 \mu\text{m}/5 \mu\text{m}$ for M_{p8} – M_{p13} . The obtained frequency response for the class-AB realization of the low-pass filter of order 1.5 is also provided in Fig. 3.11 (red dash line), where the cutoff frequency and the slope of the stopband attenuation were 9.5 Hz and -8.8 dB/oct, respectively. The obtained performance results are summarized in Table 3.3. In order to estimate the power efficiency of the designs under comparison, the Figure of Merit (FoM) defined by (3.8) has been utilized.

$$\text{FOM} = \frac{P}{nf_o(DR)} \quad (3.8)$$

According to the obtained results, it is concluded that in terms of power dissipation and/or total silicon area, the proposed class-A filter is the best choice. In the case that the power efficiency is the most important performance factor, then the proposed class-AB fractional-order filter should be employed at the expense of the total required silicon area.

3.5 Summary

A new scheme was introduced, which offers the capability of realizing current-mirror filters with large-time constants. This has been achieved through a linear compression and expansion of the input signal without affecting the

transconductance value. Compared with the conventional current-mirror filter structure, the price paid was the reduction of the dynamic range and the sensitivity performance. Nevertheless, it constitutes an attractive technique for implementing systems with on-chip capacitors, especially for biomedical applications.

The aforementioned technique has been utilized in order to realize fractional-order blocks, including differentiators, lossy and lossless integrators, as well as filters of order $1 + \alpha$ ($0 < \alpha < 1$). The benefit offered by these schemes is the low-voltage operation and reduced circuit complexity compared to the corresponding companding counterparts. The ultra-low voltage operation is performed through the employment of MOS transistors biased in the subthreshold region, while the reduction of circuit complexity is achieved through the utilization of current-mirrors as active elements which are very simple structures. Finally, the power efficiency of the proposed topologies has been further enhanced by utilizing a pseudo class-AB topology.

References

1. Solís-Bustos, S., Silva-Martínez, J., Maloberti, F., Sánchez-Sinencio, E.: A 60-dB dynamic-range CMOS sixth-order 2.4-Hz low-pass filter for medical applications. *IEEE Trans. Circuits Syst. II*. **200**(47), 1391–1398 (2000)
2. Aguado-Ruiz, J., Hernández-Alvídrez, J., López-Martín, A., Carvajal, R., Ramírez-Angulo, J.: Programmable capacitance scaling scheme based on operational transconductance amplifiers. *Electron. Lett.* **45**(3), 159–161 (2009)
3. Aguado-Ruiz, J., López-Martín, A., Ramírez-Angulo, J.: Three novel improved CMOS C-multipliers. *Int. J. Circuit Theory Appl.* **40**, 607–616 (2012)
4. Laoudias, C., Psychalinos, C.: *Integrated Filters for Short Range Wireless and Biomedical Applications*. Springer, Dordrecht (2012)
5. Tsiromokou, G., Laoudias, C., Psychalinos, C.: 0.5V fractional-order companding filters. *Int. J. Circuit Theory Appl.* **43**(9), 1105–1126 (2015)

Chapter 4

Voltage-Mode Fractional-Order Filters

4.1 Introduction

Fractional-order filters have been already introduced in discrete component form in [1–12]. The used active elements were op-amps, CCIIs, and CFOAs. Due to the employment of passive resistors, the realized time-constants have the form $\tau = RC$ and, consequently, an additional automatic tuning circuitry is required for compensating the deviations from the desired frequency response. Another important drawback is the absence of programmability, making these structure not compatible with the now days trend for realizing programmable analog filters. Alternative fractional-order filters that do not suffer from the aforementioned drawbacks have been introduced in [13–15].

The proposed structures using OTAs as active building block offer the following attractive characteristics:

- Realization of lowpass, highpass, bandpass, allpass, or bandstop filter functions by the same topology
- Electronic adjustment of their frequency characteristics as well as of their order
- Resistorless realizations, and
- Employment of only grounded capacitors.

4.2 Basic Building Blocks

The OTA, which is utilized, is that demonstrated in Fig. 4.1. A benefit of that scheme is its enhanced linearity [16].

Considering that the MOS transistors operate in subthreshold region, the expression of their small-signal transconductance is $g_m = I_o/nV_T$, where V_T is the thermal voltage (26 mV @ 27 °C), I_o the bias current, and n the subthreshold slope factor of

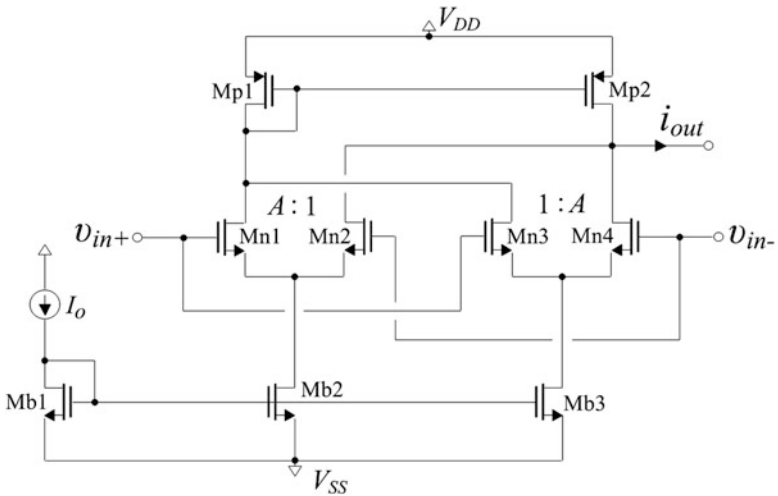


Fig. 4.1 OTA structure with enhanced linearity

an MOS transistor. Taking into account that transistors M_{n1} – M_{n2} and M_{n3} – M_{n4} have aspect ratios $A:1$ and $1:A$, respectively, the value of the transconductance of the OTA is then given by

$$g_m = g_{mo} \frac{4A}{(1+A)^2} \quad (4.1)$$

where g_{mo} is the transconductance of OTA in the case that $A = 1$. That is, $g_m = I_o / nV_T$.

The scaling factor A is used to increase the linearity of the active cell and has been chosen equal to five in order to maximize the differential input range for a THD level equal to 2% and, simultaneously, achieving a monotonic increase of THD level with the increase of the input amplitude.

4.3 Fractional-Order Generalized Filters

In order to realize fractional-order low-pass, high-pass, and all-pass filters of order α using the voltage mode technique, the FBD in Fig. 2.1b will be utilized. Thus, the resulted topology derived according to the approximation in (1.6) and using OTAs as active elements is demonstrated in Fig. 4.2. The lower left OTA is a multiple output element, where the noninverting output and inverting output are used for realizing the fractional-order low-pass, fractional-order high-pass functions, and fractional-order all-pass function, respectively. This could be easily performed using an appropriate switching scheme.

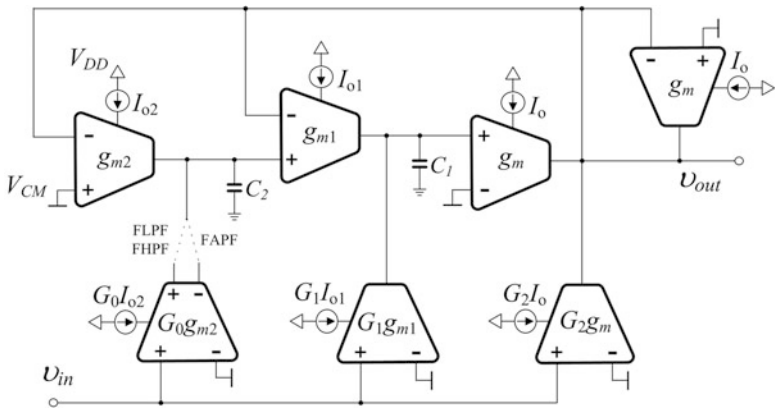


Fig. 4.2 OTA-C realization of fractional low-pass, high-pass, all-pass filter functions of order α

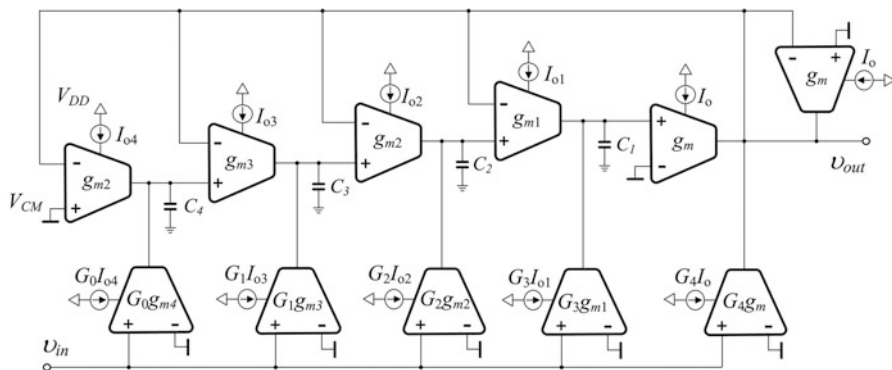


Fig. 4.3 OTA-C realization of low-pass, high-pass, band-pass, and band-stop filter functions of order $\alpha + \beta$

In order to realize a fractional-order band-pass of order α , the topology in Fig. 2.2b could be used where the building blocks $H_1(s)$, and $H_2(s)$ are those depicted in Fig. 4.2.

The corresponding topology for implementing fractional-order low-pass, high-pass, band-pass, and band-stop filter functions of order $\alpha + \beta$ is demonstrated in Fig. 4.3, where the FBD in Fig. 2.4b is utilized.

The main benefits offered by these topologies are the following:

- Different filter functions are realized by the same core, which is very important from the flexibility point of view.
- The realizations are resistorless due to the employment of OTAs as active elements.
- Their frequency characteristics and order could be electronically adjusted by an appropriate dc current.
- Only grounded capacitors are utilized and this is very important especially in high frequency applications.

4.4 Simulation Results

The behavior of the proposed generalized filter structures is evaluated through simulation results, where the most important factors have been considered. Thus, the performance is evaluated using the Analog Design Environment of the Cadence software and the Design Kit provided by the AMS 0.35 μm CMOS process. The employed bias scheme was $V_{DD} = 1.5 \text{ V}$ and $V_{CM} = 0.75 \text{ V}$. The aspect ratios of the transistors of the OTA in Fig. 4.1 were $60 \mu\text{m}/10 \mu\text{m}$ for M_{b1} – M_{b3} , $25 \mu\text{m}/1 \mu\text{m}$ for M_{n1} , M_{n4} , $5 \mu\text{m}/1 \mu\text{m}$ for M_{n2} , M_{n3} , and $10 \mu\text{m}/15 \mu\text{m}$ for M_{p1} – M_{p2} . Assuming that the desired pole frequency is $f_o = 100 \text{ Hz}$ and both capacitors have the same value equal to $C_1 = C_2 = 50 \text{ pF}$, the values of bias currents I_{oi} and scaling factors are summarized in Table 4.1.

Firstly, the filter topology given in Fig. 4.2 will be evaluated through simulation results. Using (4.1) it is readily obtained that the realized time-constants of (2.19) will be given as shown in (4.2) from which is obvious that they could be electronically controlled.

$$\tau_i = \frac{C_i n V_T}{I_{oi}} \cdot \frac{(1 + A)^2}{4A} \quad (4.2)$$

where ($i = 1, 2$) is the number of integrator.

The derived frequency response is given in the plots of Fig. 4.4, where with dashed lines the corresponding theoretically predicted responses are also provided.

In the next, the behavior of fractional filters of order $\alpha + \beta$ will be evaluated, utilizing the same design considerations. The values of bias currents I_{oi} are summarized in Table 4.2.

The layout design that has been performed in order to be taken into account the parasitic capacitances and resistances of the topology is demonstrated in Fig. 4.5. The obtained frequency responses with the corresponding theoretically predicted are simultaneously given in Fig. 4.6.

The electronic tuning capability of the proposed generalized fractional-order filters is demonstrated in the case of $\alpha + \beta$ order FBPF. The corresponding values

Table 4.1 Values of scaling factors, and bias currents for fractional filters of order α in Fig. 4.2, derived according to the approximation in (1.6)

$f_o = 100 \text{ Hz}$ $C = 50 \text{ pF}$	LP ($\alpha = 0.5$)	HP ($\alpha = 0.5$)	AP ($\alpha = 0.5$)	BP $j = 1$ ($\alpha = 1, \beta = 0.5$)	BP $j = 2$ ($\alpha = 1, \beta = 0.5$)
G_2	0.167	0.833	0.667	0	5
G_1	0.5	0.5	0	0.5	1
G_0	0.833	0.167	−0.667	1	0.2
I_o	6.37 nA	6.37 nA	6.37 nA	3.82 nA	19.1 nA
I_{o1}	6.37 nA	6.37 nA	6.37 nA	3.82 nA	19.1 nA
I_{o2}	573.4 pA	573.4 pA	573.4 pA	955 pA	955 pA

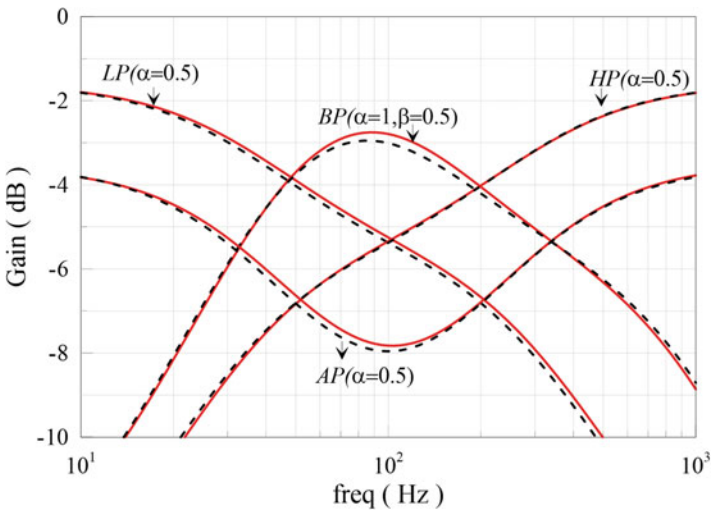


Fig. 4.4 Frequency response of the fractional generalized filter of order α in Fig. 4.2

Table 4.2 Values of scaling factors, and bias currents for fractional filters of order $\alpha + \beta$ in Fig. 4.3, derived according to the approximation in (1.6)

$f_o = 100$ Hz $C = 50$ pF	LP $\alpha = 1, \beta = 0.5$	HP $\alpha = 0.5, \beta = 1$	BS $\alpha = 1, \beta = 0.5$	BP $\alpha = 1, \beta = 0.5$
G_4	0	0.8333	1	0
G_3	0.0476	0.5556	0.7619	0.2381
G_2	0.2973	0.3438	0.5946	0.4054
G_1	0.5556	0.0476	0.5926	0.4074
G_0	0.8333	0	0.8333	0.1667
I_o	8.03 nA	8.6 nA	8.03 nA	8.03 nA
I_{o1}	8.03 nA	8.6 nA	8.03 nA	8.03 nA
I_{o2}	3.37 nA	2.26 nA	3.18 nA	3.37 nA
I_{o3}	1.39 nA	1.25 nA	1.47 nA	1.39 nA
I_{o4}	424.7 pA	455 pA	424.7 pA	424.7 pA

of bias currents and scaling factors for tuning α and β are given in Table 4.3, while the obtained frequency responses are demonstrated in Fig. 4.7. Using these plots, the obtained frequency characteristics of the filters are summarized in Table 4.4, where the corresponding theoretically predicted values are given in parentheses.

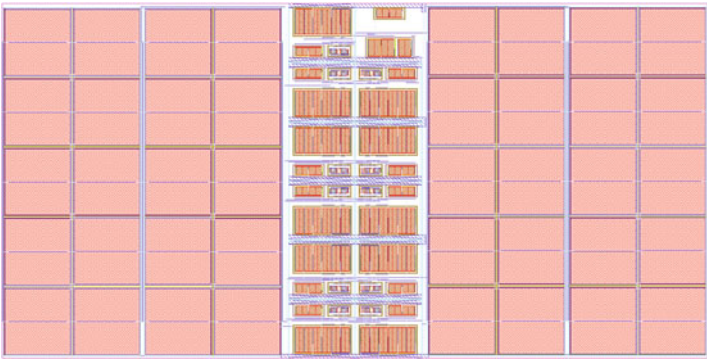


Fig. 4.5 Layout design of the fractional generalized filter of order $\alpha + \beta$ in Fig. 4.3

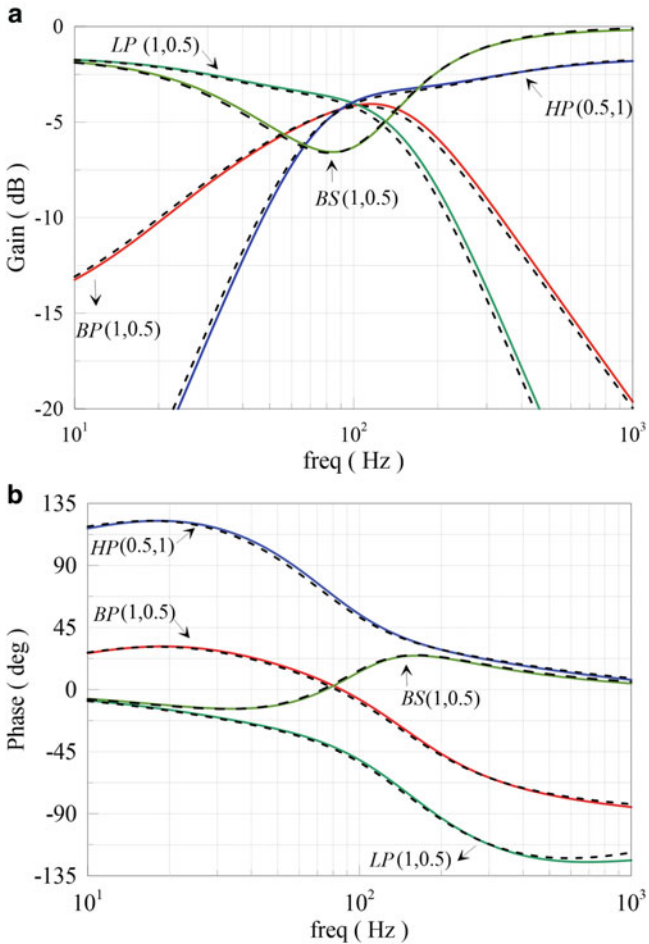


Fig. 4.6 (a) magnitude, and (b) phase response of the fractional generalized filter of order $\alpha + \beta$

Table 4.3 Bias currents and scaling factors for tuning the order α and β of an FBPF

$f_o = 100 \text{ Hz}, C = 50 \text{ pF}$	$\alpha = 0.7, \beta = 0.5$	$\alpha = 0.8, \beta = 0.7$	$\alpha = 0.9, \beta = 0.9$
G_4	0.0771	0.0453	0.0196
G_3	0.2979	0.3156	0.3333
G_2	0.4200	0.4425	0.4759
G_1	0.3654	0.3501	0.3333
G_0	0.1643	0.0780	0.0196
I_o	9.89 nA	8.1 nA	6.63 nA
I_{o1}	9.89 nA	8.1 nA	6.63 nA
I_{o2}	3.25 nA	2.95 nA	2.65 nA
I_{o3}	1.24 nA	1.30 nA	1.37 nA
I_{o4}	368.6 pA	443.7 pA	550.4 pA

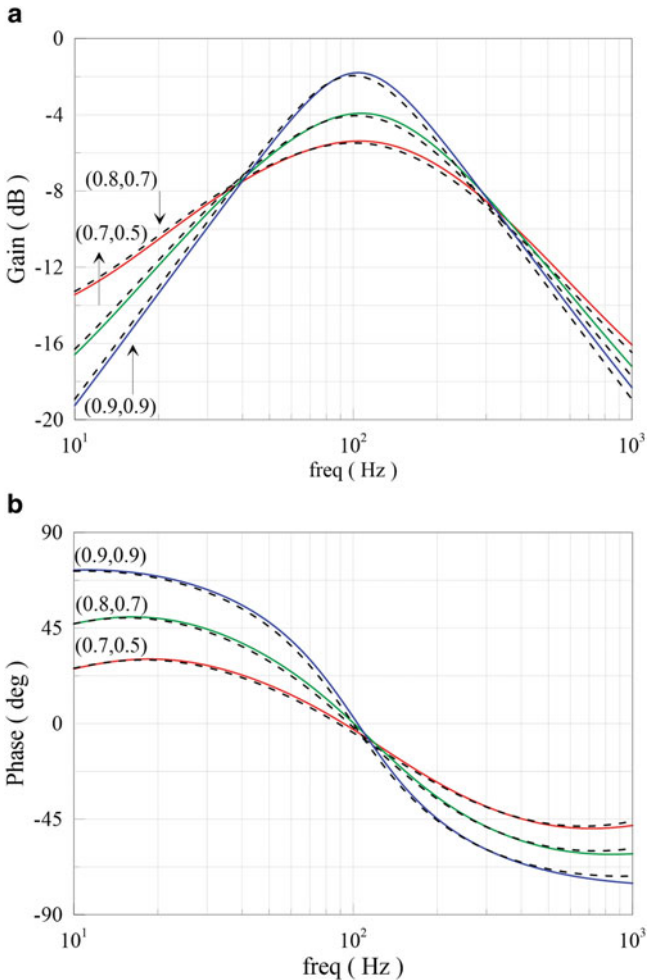
**Fig. 4.7** Electronic tunability of the order $\alpha + \beta$ of the FBPF (a) magnitude and (b) phase response

Table 4.4 Frequency characteristics of the FBPFs

FBPF	$\alpha = 0.7, \beta = 0.5$	$\alpha = 0.8, \beta = 0.7$	$\alpha = 0.9, \beta = 0.9$	$\alpha = 1, \beta = 0.5$
f_{peak} (Hz)	104.7 (100)	104.7 (100)	104.7 (100)	106.8 (100)
Gain(max) (dB)	-5.6(-5.7)	-4.1 (-4.2)	-1.8 (-1.9)	-4.7 (-4.9)
f_{h1} (Hz)	30.3(28.5)	42.19 (39.95)	55.78 (53.13)	33.03 (31.01)
f_{h2} (Hz)	304.4 (293.8)	250.6 (242.7)	194 (188.2)	257.1 (248.7)
Slope at upper stopband (dB/oct)	-3.96 (-4)	-4.9 (-5)	-5.8 (-5.8)	-5.9 (-5.9)
Slope at lower stopband (dB/oct)	3 (3)	4.5 (4.4)	5.9 (5.8)	3 (3)

4.5 Summary

A generalized voltage-mode filter topology is introduced in this Chapter, using OTAs as active elements. Different types of filter functions could be realized without modifying its core, which is very important from the design flexibility point of view. In addition their frequency characteristics could be electronically programmed through appropriate bias currents. The performance of the filters has been evaluated through postlayout simulations results, which proves that they could be considered as attractive candidates in several applications, especially when high performance is required.

References

- Freeborn, T., Maundy, B., Elwakil, A.: Field programmable analogue array implementation of fractional step filters. *IET Circ. Dev. Syst.* **4**(6), 514–524 (2010)
- Radwan, A., Soliman, A., Elwakil, A.: First-order filters generalized to the fractional domain. *J. Circ. Syst. Comput.* **17**(1), 55–66 (2008)
- Radwan, A., Elwakil, A., Soliman, A.: On the generalization of second-order filters to the fractional-order domain. *J. Circ. Syst. Comput.* **18**(2), 361–386 (2009)
- Maundy, B., Elwakil, A., Freeborn, T.: On the practical realization of higher-order filters with fractional stepping. *Signal Process.* **91**(3), 484–491 (2011)
- Ahmadi, P., Maundy, B., Elwakil, A., Belostotski, L.: High-quality factor asymmetric-slope band-pass filters: a fractional-order capacitor approach. *IET Circ. Dev. Syst.* **6**(3), 187–197 (2012)
- Soltan, A., Radwan, A., Soliman, A.: Fractional-order filter with two fractional elements of dependant orders. *Microelectron. J.* **43**(11), 818–827 (2012)
- Radwan, A., Salama, K.: Fractional-order RC and RL circuits. *Circ. Syst. Signal Process.* **31**(6), 1901–1915 (2012)
- Radwan, A.: Resonance and quality factor of the RLaCa fractional circuit. *IEEE J. Emerging Sel. Top. Circ. Syst.* **3**(3), 377–385 (2013)
- Ali, A., Radwan, A., Soliman, A.: Fractional-order Butterworth filter: active and passive realizations. *IEEE J. Emerging Sel. Top. Circ. Syst.* **3**(3), 346–354 (2013)

10. Tripathy, M., Biswas, K., Sen, S.: A design example of a fractional-order Kerwin–Huelsman–Newcomb biquad filter with two fractional capacitors of different order. *Circ. Syst. Signal Process.* **32**(4), 1523–1536 (2013)
11. Soltan, A., Radwan, A.G., Soliman, A.M.: Fractional order Sallen–Key and KHN filters: stability and poles allocation. *Circ. Syst. Signal Process.* **34**(5), 1461–1480 (2015)
12. Tripathy, M., Mondal, D., Biswas, K., Sen, S.: Experimental studies on realization of fractional inductors and fractional-order bandpass filters. *Int. J. Circ. Theory Appl.* **43**(9), 1183–1195 (2015)
13. Tsirimokou, G., Psychalinos, C.: Ultra-low voltage fractional-order differentiator and integrator topologies: an application for handling noisy ECGs. *Analog Integr. Circ. Sig. Process.* **81**(2), 393–405 (2014)
14. Tsirimokou, G., Laoudias, C., Psychalinos, C.: 0.5V fractional-order companding filters. *Int. J. Circ. Theory Appl.* **43**(9), 1105–1126 (2015a)
15. Tsirimokou, G., Psychalinos, C.: Ultra-low voltage fractional-order circuits using current-mirrors. *Int. J. Circ. Theory Appl.* **44**(1), 109–126 (2016)
16. Tsirimokou, G., Psychalinos, C., Elwakil, A.: Emulation of a constant phase element using operational transconductance amplifiers. *Analog Integr. Circ. Sig. Process.* **85**(3), 413–423 (2015)

Chapter 5

Emulation of Fractional-Order Capacitors (CPEs) and Inductors (FOIs)

5.1 Introduction

Fractional-order impedances are, as has been already mentioned, the generalized form of conventional circuit impedances and are essential for accurate and realistic circuit models in a wide range of applications [1]. A fractional derivative for order α described by the Caputo derivative [2] is that already given in (1.1). Assuming zero initial conditions, it is then possible to define a general electrical impedance described through the following expression

$$Z(s) = \kappa s^\alpha = (\kappa\omega)^\alpha e^{j\left(\frac{\alpha\pi}{2}\right)} = (\kappa\omega)^\alpha \left(\cos\left(\frac{\alpha\pi}{2}\right) + j\sin\left(\frac{\alpha\pi}{2}\right) \right) = |z| \angle \vartheta \quad (5.1)$$

where $\vartheta = \alpha\pi/2$.

The impedance $Z(s)$ in (5.1) is capable for representing different types of elements, the nature of which is depended on value of variables (κ, α) . Thus, in case that $(\kappa, \alpha) = (R, 0)$, then the $Z(s)$ represents a resistor. Also, if $(\kappa, \alpha) = (L, 1)$, then it represents an inductor, while for $(\kappa, \alpha) = (1/C, -1)$, it represents a capacitor. In the range $(0 < \alpha < 1)$, this element may generally be considered to represent a fractional-order inductor. For any $(-1 < \alpha < 0)$, it may be considered to represent a fractional-order capacitor. Thereafter, when $\alpha \neq \pm 1$, those elements could be termed as fractional-order inductors and fractional-order capacitors with frequency-dependent losses [3].

However, inspecting expression (5.1), there should be mentioned that in order not to be inconsistent in the units of L , and C , the constant κ is called pseudo-inductance and pseudo-capacitance, where L_β and C_α are the corresponding associated symbols. As a consequence, the impedance for a fractional-order capacitor is given in (5.2)

$$Z_{C_\alpha, \alpha}(s) = \frac{1}{C_\alpha s^\alpha} \quad (5.2)$$

where C_α is the normalized capacitance and has the units of Farad/sec^{1- α} .

From now onwards, taking into account that the impedance of a fractional-order capacitor, also known as a Constant-Phase Element (CPE), is that given by (6.2), then the phase angle is where $\vartheta = -\alpha\pi/2$, and the order α is in the range ($0 < \alpha < 1$). The value (in Farad) of the frequency-dependent capacitance (C) of a fractional-order capacitor will be then calculated as

$$C = \frac{C_\alpha}{\omega^{1-\alpha}}. \quad (5.3)$$

In addition, the impedance for a fractional-order inductor is that given in (5.4)

$$Z_{L_\beta, \beta}(s) = L_\beta s^\beta \quad (5.4)$$

where L_β is the normalized inductance and has the units of Henry/sec^{1- β} .

Also, taking into account that the impedance of a fractional-order inductor, called as Fractional-Order Inductor (FOI), is that given by (5.5), then the phase angle is $\vartheta = \beta\pi/2$, and the order β is in the range ($0 < \beta < 1$). Therefore, the relationship between inductance and pseudo-inductance is

$$L = \frac{L_\beta}{\omega^{1-\beta}} \quad (5.5)$$

Taking into account that fractional order capacitors and inductors are a set of the most important elements in several applications especially in order to emulate biological tissues, there should be mentioned that there is need for developing both voltage and current-excited elements [4, 5]. The necessity of such systems relies on the fact that not only potentiostatic (voltage-excited), but also galvanostatic (current-excited) measurements are required for characterizing these elements. As a result, the aforementioned schemes will be extended developed and presented in the next sessions.

5.2 Proposed Emulation Scheme for Voltage Exited CPE and FOI

Inspecting the general form of electrical impedance given in (5.1), there can be easily seen that the realization of fractional-order capacitor/inductor emulators could be achieved using a fractional-order differentiator/integrator of order α/β with unity gain frequency $\omega = 1/\tau$, along with an appropriate voltage-to-current converter. The functional block diagram for emulating a fractional-order capacitor

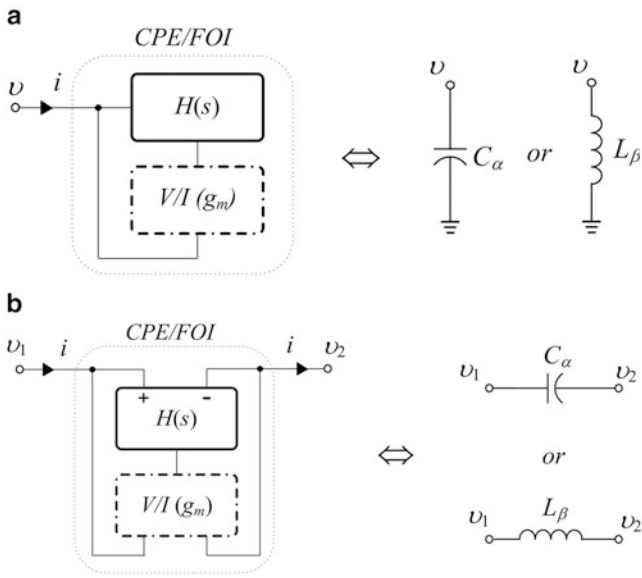


Fig. 5.1 Emulation schemes for the voltage-excited (a) grounded and (b) floating fractional-order capacitor/inductor

or inductor is shown in Fig. 5.1. The corresponding scheme for the floating element has been easily derived using a two-input differentiator/integrator and a multiple output voltage-to-current converter as demonstrated in Fig. 5.1b. The equivalent impedance, either for grounded capacitor/inductor ($Z_{\text{eq}} \equiv v/i$) or for floating ($Z_{\text{eq}} \equiv v_1 - v_2/i$), is given by the expression.

$$Z_{\text{eq}} = \frac{1}{g_m H(s)} \quad (5.6)$$

where $H(s)$ could be equal to (τs^α) or $1/(\tau s^\beta)$, and $R = 1/g_m$ is the equivalent impedance in (Ω) at a given frequency.

The frequency dependence of equivalent impedance is clearly demonstrated using the following forms:

$$Z_{\text{eq}}(\text{CPE}) = \frac{1}{g_m} \left(\frac{\omega_0}{\omega} \right)^\alpha \quad (5.7)$$

$$Z_{\text{eq}}(\text{FOI}) = \frac{1}{g_m} \left(\frac{\omega}{\omega_0} \right)^\beta \quad (5.8)$$

Using (5.2), (5.4), and (5.6), it is obtained that

$$C_\alpha = g_m \tau^\alpha \quad (5.9)$$

$$L_\beta = \tau^\beta / g_m \quad (5.10)$$

Also, using (5.3) and (5.5), the expressions for (5.9) and (5.10) could be written as

$$C = \frac{g_m}{\omega_o^\alpha \omega^{1-\alpha}} \quad (5.11)$$

$$L = \frac{1}{g_m \omega_o^\alpha \omega^{1-\alpha}} \quad (5.12)$$

Selecting $\omega = \omega_o$, from (5.11) and (5.12), it is derived that the value of the de-normalized capacitance/inductance will be

$$C = \frac{g_m}{\omega_o} \quad (5.13)$$

$$L = \frac{1}{g_m \omega_o} \quad (5.14)$$

Inspecting the above equations, it can be easily observed the fact that the time-constant τ is chosen through the unity gain frequency ω_o of the differentiator/integrator, while the equivalent impedance, and as a consequence the capacitance value C_α , is determined through the transconductance (g_m) of the voltage-to-current converter.

The two-input fractional-order differentiator/ integrator block denoted as $H(s)$ in Fig. 5.1, could be realized using the functional block diagram given in Fig. 2.1b, where the second-order approximation of the CFE has been utilized. The realization of the corresponding scheme could be realized using OTAs as active elements and is that demonstrated in Fig. 5.2. In case that a grounded element is needed, then this could be achieved by setting v_{in-} equal to V_{CM} . Thus, the only input voltage v is that

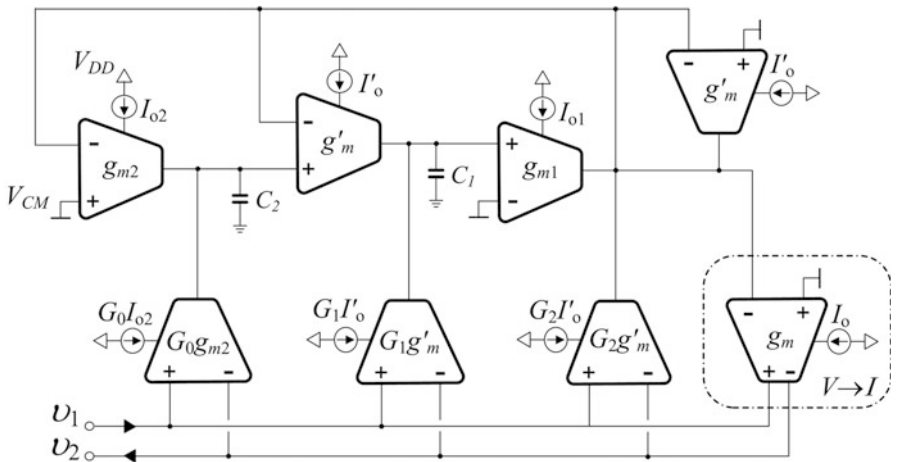


Fig. 5.2 Emulation scheme for the fractional-order capacitor ($I'_o = I_{o2}$)/inductor ($I'_o = I_{o1}$) using OTAs

Table 5.1 Design equations for the emulated fractional-order capacitors and inductors around a center frequency $\omega_o = 1/\tau$

Design parameters	CPE	FOI
τ_1	$\left(\frac{\alpha^2 - 3\alpha + 2}{-2\alpha^2 + 8}\right) \cdot \tau$	$\left(\frac{\beta^2 + 3\beta + 2}{-2\beta^2 + 8}\right) \cdot \tau$
τ_2	$\left(\frac{\alpha^2 + 3\alpha + 2}{-2\alpha^2 + 8}\right) \cdot \tau$	$\left(\frac{-2\beta^2 + 8}{\beta^2 - 3\beta + 2}\right) \cdot \tau$
G_2	$\left(\frac{\alpha^2 + 3\alpha + 2}{\alpha^2 - 3\alpha + 2}\right)$	$\left(\frac{\beta^2 - 3\beta + 2}{\beta^2 + 3\beta + 2}\right)$
G_1	1	1
G_0	$\left(\frac{\alpha^2 - 3\alpha + 2}{\alpha^2 + 3\alpha + 2}\right)$	$\left(\frac{\beta^2 + 3\beta + 2}{\beta^2 - 3\beta + 2}\right)$

denoted as v_{in+} . The transfer function $H(s)$ has been already described in Chap. 2 with (2.3), and (2.5). Thus, the resulted equivalent impedance using the second-order approximation of CFE is described by (5.15).

$$Z_{eq} = \frac{1}{g_m} \cdot \frac{G_2 s^2 + \frac{G_1}{\tau_1} s + \frac{G_0}{\tau_1 \tau_2}}{s^2 + \frac{1}{\tau_1} s + \frac{1}{\tau_1 \tau_2}} \quad (5.15)$$

The design equations are already given in Tables 2.1 and 2.2, from which can be readily obtained that the time-constants τ_1 and τ_2 as well as the gain factors G_j are dependent on the order of the CPE/FOI (α/β). For the sake of completeness, the design equations derived according to the approximation (1.6) are summarized in Table 5.1.

There should be mentioned that the required voltage scaling factors G_j can be easily implemented by OTAs with appropriate transconductance values (i.e., $G_j = g_{mj}/g_m$). From the resulted design equations, it is obviously clear that the order (α/β) of the fractional-order differentiator/integrator and as a consequence the order of fractional-order capacitor/inductor emulator is determined through appropriate values of time-constants τ_i and gain factors G_j .

As it has been already mentioned, the capacitance value (in Farad) is determined through the transconductance g_m of the voltage-to-current converter. In other words, the order α/β at a given frequency ω_o is orthogonal to the equivalent impedance Z_{eq} . As a result, having available these equations, the utilization of any type of circuit design, which is able to realize the FBD shown in Fig. 2.1b along with an appropriate $V \rightarrow I$ converter (g_m), offers the capability of realizing the transfer function given in (5.15).

Taking into account that MOS transistors of OTAs that depicted in Fig. 4.1 are biased in subthreshold region, the transconductance g_m is that given by (5.16)

$$g_m = \frac{I_o}{nV_T} \cdot \frac{4A}{(1+A)^2} \quad (5.16)$$

Thus, the realized time-constants of (5.15) will be given as

$$\tau_i = \frac{C_i n V_T}{I_{oi}} \cdot \frac{(1+A)^2}{4A} \cdot \frac{1}{\tau}, (i = 1, 2) \quad (5.17)$$

where τ is the desired unity gain frequency of the differentiator/integrator, and A is set equal to 5 for enhanced linearity.

Inspecting expressions given in (5.13) and (5.14) combined with that in (5.16), it is easily obtained the fact that not only the order of the CPE/FOI (α/β), but also the equivalent capacitance/inductance could be electronically controlled through the appropriate bias currents I_o of the $V \rightarrow I$ converters. Summarizing, the corresponding equations for the bias currents of the differentiator are the following:

$$I_{o1} = C_1 n V_T \cdot \frac{(1+A)^2}{4A} \cdot \left(\frac{-2\alpha^2 + 8}{\alpha^2 - 3\alpha + 2} \right) \cdot \frac{1}{\tau} \quad (5.18)$$

$$I_{o2} = C_2 n V_T \cdot \frac{(1+A)^2}{4A} \cdot \left(\frac{\alpha^2 + 3\alpha + 2}{-2\alpha^2 + 8} \right) \cdot \frac{1}{\tau} \quad (5.19)$$

while for the integrator

$$I_{o1} = C_1 n V_T \cdot \frac{(1+A)^2}{4A} \cdot \left(\frac{-2\beta^2 + 8}{\beta^2 + 3\beta + 2} \right) \cdot \frac{1}{\tau} \quad (5.20)$$

$$I_{o2} = C_2 n V_T \cdot \frac{(1+A)^2}{4A} \cdot \left(\frac{\beta^2 - 3\beta + 2}{-2\beta^2 + 8} \right) \cdot \frac{1}{\tau} \quad (5.21)$$

In addition, the equivalent capacitance/inductance is electronically controlled through the bias current of the $V \rightarrow I$ converter using

$$I_{oC} = C n V_T \cdot \frac{(1+A)^2}{4A} \cdot \frac{1}{\tau} \quad (5.22)$$

$$I_{oL} = \frac{1}{L} n V_T \cdot \frac{(1+A)^2}{4A} \cdot \tau \quad (5.23)$$

Owing to the nature of the employed approximation, the bandwidth of the CPE is $[\omega_o/10, 10\omega_o]$. Due to the fact that the unity-gain frequency of the differentiator/integrator is $\omega_o = 1/\tau$, then from the expressions about the time-constants in Table 5.1 and (5.17) it is concluded that the bandwidth is also electronically controlled through the appropriate bias currents given in (5.20), (5.21), and (5.22). There should be mentioned that the bias current noted as I_o' in Fig. 5.2, is set equal to I_{o2} in case of a fractional-order differentiator and equal to I_{o1} in case of a fractional order integrator. Summarizing, the order of emulated capacitor/inductor and the equivalent impedance could be electronically adjusted through bias

The transfer function, which is able to represent the operation of fractional-order differentiator/integrator of order (α/β) with unity gain frequency $\omega_o = 1/\tau$, is implemented and described in detail in previous section. The OTA-C realization is that depicted in Fig. 5.2.

Taking into account that a low impedance node for admitting the input current is required, the leftmost OTA in Fig. 5.3a is capable for performing this implementation. Assuming that the impedance of the $H(s)$ block is infinite, then $i = i_1 + i_2 - i_3$.

5.4 Chip Fabrication and Experimental Results

The utilization of the already studied methods in previous sections for emulating fractional-order capacitors and inductors will be used for fabricating these elements for the first time in the literature. The equivalent capacitance and inductance could be electronically adjusted using a single bias current and two external capacitors, which are responsible for selecting the bandwidth of operation. Each CPE/FOI has been implemented using the circuit given in Fig. 5.2, where OTAs were used as active elements, in order to realize the proposed topology given in Fig. 5.1. The corresponding impedances, which are able to be realized using these emulators, by utilizing the second-order approximation of CFE, are the following

$$Z_{\text{CPE}} = \frac{1}{g_m} \cdot \frac{(\alpha^2 + 3\alpha + 2)(\tau s^2) + (-2\alpha^2 + 8)(\tau s) + (\alpha^2 - 3\alpha + 2)}{(\alpha^2 - 3\alpha + 2)(\tau s^2) + (-2\alpha^2 + 8)(\tau s) + (\alpha^2 + 3\alpha + 2)} \quad (5.24)$$

$$Z_{\text{FOI}} = \frac{1}{g_m} \cdot \frac{(\beta^2 - 3\beta + 2)(\tau s^2) + (-2\beta^2 + 8)(\tau s) + (\beta^2 + 3\beta + 2)}{(\beta^2 + 3\beta + 2)(\tau s^2) + (-2\beta^2 + 8)(\tau s) + (\beta^2 - 3\beta + 2)} \quad (5.25)$$

The transconductance g_m is capable for being electronically programmed through bias current I_o as shown in (5.26).

$$g_m = \frac{5}{9} \cdot \frac{I_o}{nV_T} \quad (5.26)$$

where n is the MOS transistor subthreshold slope factor ($n \approx 1.3$), and V_T is the thermal voltage ($V_T \approx 26$ mV).

As a result, the equivalent capacitance/inductance values are determined through the following equations

$$C_{\text{eq}} = \frac{5}{9} \cdot \frac{I_o}{nV_T} \cdot \tau_u \text{ (CPE)} \quad (5.27)$$

$$L_{\text{eq}} = \frac{9}{5} \cdot \frac{nV_T}{I_o} \cdot \tau_u \text{ (FOI)} \quad (5.28)$$

where $\tau_u = 1/\omega_o$ is the unity gain frequency of the differentiator/integrator.

The topology of OTA that has been utilized is depicted in Fig. 4.1, while the aspect ratios of transistors are $10 \mu\text{m}/10 \mu\text{m}$ for $M_{b1}-M_{b3}$, $50 \mu\text{m}/1 \mu\text{m}$ for $M_{n1}-M_{n4}$, $10 \mu\text{m}/1 \mu\text{m}$ for $M_{n2}-M_{n3}$, and $60 \mu\text{m}/10 \mu\text{m}$ for $M_{p1}-M_{p2}$.

The design of the chips has been performed under the following considerations:

- CPEs and FOIs with fixed order will be fabricated. More specifically in the first chip will be included CPEs with orders 0.3, 0.4, 0.5, 0.6, and 0.7, while in the second CPES and FOIs with orders 0.2, 0.5, and 0.8.
- External capacitors with equal value, i.e., $C_1 = C_2 = C_{\text{ext}}$, will be used. As a result, the time-constant of the unity gain frequency will be calculated according to (5.29) and (5.30) for CPE of order α and FOI of order β , respectively.

$$\tau_u (\text{CPE}) = \frac{9}{5} \cdot \frac{C_{\text{ext}} n V_T}{I_o} \cdot \frac{\alpha^2 + 3\alpha + 2}{-2\alpha^2 + 8} \quad (5.29)$$

$$\tau_u (\text{FOI}) = \frac{9}{5} \cdot \frac{C_{\text{ext}} n V_T}{I_o} \cdot \frac{\beta^2 - 3\beta + 2}{-2\beta^2 + 8} \quad (5.30)$$

Thus, the appropriate bias currents I_{o1} and I_{o2} , as well as the design equations of gain factors G_i ($i = 0, 1, 2$), are summarized in Table 5.2.

- The same bias voltage scheme will be employed for all the emulators.

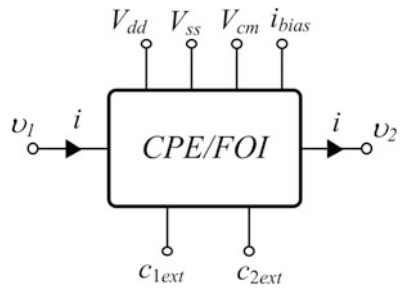
Only one dc current source with value I_o will be required for biasing the chip. This will be the current for biasing the $V \rightarrow I$ converter, which has a transconductance g_m . The realization of the required bias currents (I_o), as well as of their scaled replicas for each CPE/FOI, will be performed using appropriate current mirror stages. Please note that the order is fixed for every CPE/FOI and, therefore, static current mirrors have been used. Therefore, the symbol each of the designed CPE/FOI emulators is that demonstrated in Fig. 5.4.

Under the aforementioned conditions, there will be presented the effects of C_{ext} and I_o variations in the behavior of the emulators. In other words, the tuning capability will be investigated.

Table 5.2 Design equations for bias currents and gain factors shown in Fig. 5.2

Variable	CPE	FOI
I_{o1}	$\frac{(-2\alpha^2 + 8)^2}{(\alpha^2 + 3\alpha + 2)(\alpha^2 - 3\alpha + 2)} \cdot I_o$	$\frac{(-2\beta^2 + 8)^2}{(\beta^2 + 3\beta + 2)(\beta^2 - 3\beta + 2)} \cdot I_o$
I_{o2}	I_o	I_o
G_2	$\left(\frac{\alpha^2 + 3\alpha + 2}{\alpha^2 - 3\alpha + 2} \right)$	$\left(\frac{\beta^2 - 3\beta + 2}{\beta^2 + 3\beta + 2} \right)$
G_1	1	1
G_0	$\left(\frac{\alpha^2 - 3\alpha + 2}{\alpha^2 + 3\alpha + 2} \right)$	$\left(\frac{\beta^2 + 3\beta + 2}{\beta^2 - 3\beta + 2} \right)$

Fig. 5.4 Symbol of CPE/FOI emulator



5.4.1 Effects of Variation of the External Capacitors of the Chip

Assuming that the time-constant of the differentiator/integrator will be changed to a new value: $\tau' = \kappa\tau$ ($\kappa = C'_{\text{ext}}/C_{\text{ext}}$), where C'_{ext} is the new value of external capacitors, then according to (5.29) or (5.30) the unity-gain frequency $\omega_o = 1/\tau$ will be changed to a new value equal to ω_o/κ . As a result, the bandwidth of operation of the CPE/FOI that initially was equal to $[\omega_o/10, 10\omega_o]$ will be changed to $[\omega_o/(10\kappa), (10)/\kappa]$. Also, the impedance of both initial and tuned frequency remains the same.

5.4.2 Effects of Variation of the Bias Current of the Chip

In case that the time-constant of the differentiator/integrator is changed to a new value: $\tau' = \tau/n$ ($n = I'_o/I_o$), where I'_o is the new value of bias current, the unity-gain frequency $\omega_o = 1/\tau$ will be changed to a new value equal to $n\omega_o$. As a result, the bandwidth of operation of the CPE/FOI which initially was equal to $[\omega_o/10, 10\omega_o]$ will be changed to $[n\omega_o/10, 10n\omega_o]$. In addition, the value of transconductance g_m of the $V \rightarrow I$ converter is changed to $g'_m = ng_m$. Finally, the realized impedances of CPE and FOI will be scaled by a factor $n^{1-\alpha}$ and $1/n^{1+\beta}$, respectively.

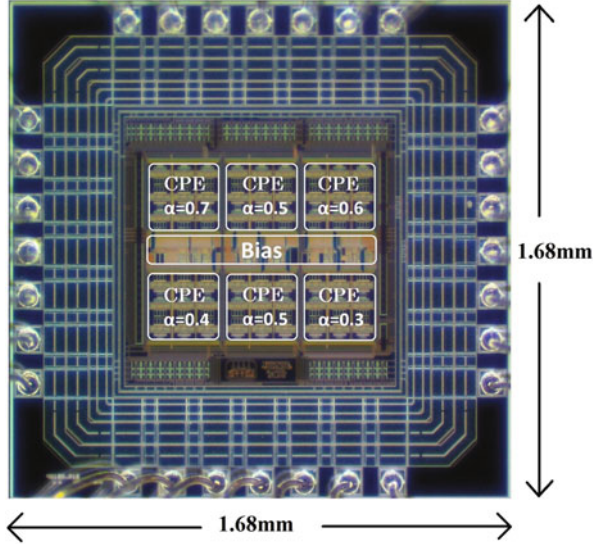
5.4.3 Effects of Variation of both the Bias Current (I_o) and External Capacitors (C_{ext}) of the Chip

Let us consider that $n = \kappa$ (i.e., $I'_o/I_o = C'_{\text{ext}}/C_{\text{ext}}$). Then, according to (5.29) or (5.30), the time-constant of the differentiator/integrator and, consequently, the unity-gain frequency remain unchanged. Therefore, the bandwidth of operation of the CPE/FOI $[\omega_o/10, 10\omega_o]$ is not affected. The value of the transconductance g_m of the $V \rightarrow I$ converter is changed to $g'_m = ng_m$ due to the change of I_o . From the

Table 5.3 Expressions for calculating values of C_α , L_β , C_{eq} , L_{eq} according to the variation of the bias current (I_o) and/or external capacitors (C_{ext})

$\tau' = \kappa\tau, \left(\kappa = \frac{C'_{ext}}{C_{ext}} \right)$	$\tau' = \frac{\tau}{n}, \left(n = \frac{I'_o}{I_o} \right)$	$\kappa = n, \frac{I'_o}{I_o} = \frac{C'_{ext}}{C_{ext}}$
$C'_\alpha = C_\alpha \cdot \kappa^\alpha$	$C'_\alpha = C_\alpha \cdot n^{1-\alpha}$	$C'_\alpha = nC_\alpha$
$L'_\beta = L_\beta \cdot \kappa^\beta$	$L'_\beta = \frac{L_\beta}{n^{1+\beta}}$	$L'_\beta = \frac{L_\beta}{n}$
$C'_{eq} = C_{eq} \cdot \kappa$	$C'_{eq} = C$	$C'_{eq} = nC_{eq}$
$L'_{eq} = L_{eq} \cdot \kappa$	$L'_{eq} = \frac{L}{n^2}$	$L'_{eq} = \frac{L_{eq}}{n}$

Fig. 5.5 Die photo of the integrated fractional-order capacitors with fixed orders $\alpha = 0.3, 0.4, 0.5, 0.6, 0.7$



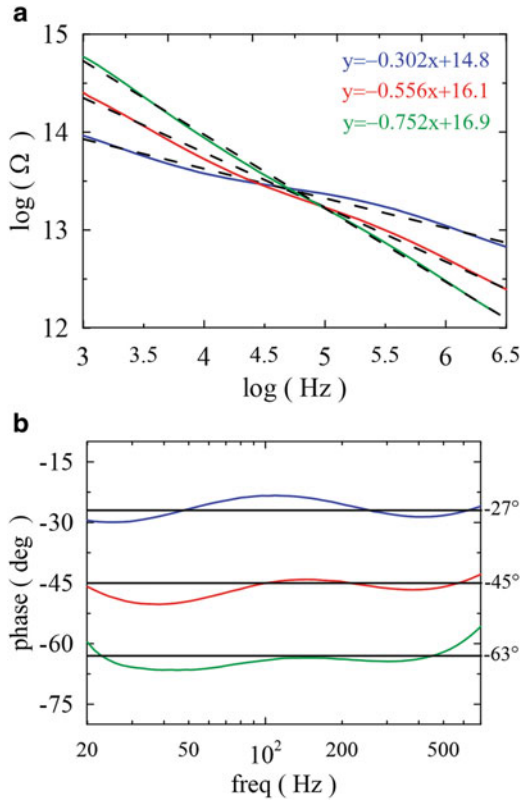
above, it is readily concluded that this tuning scheme allows the scaling of impedances without affecting the bandwidth of operation.

Summarizing, it is derived that the new values of capacitances and inductances using (5.11), (5.12), (5.13), and (5.14) are given in Table 5.3.

Both designs are fabricated in AMS 0.35 μm C35B4C3 CMOS technology, and the total occupied is 2.82 mm^2 . The first chip named *kpproj1* includes CPEs with orders 0.3, 0.4, 0.5, 0.6, and 0.7 where nano-Farad pseudo-capacitances could be achieved. A die photo of the aforementioned work is shown in Fig. 5.5. The possible values of bias current I_o were found to be in general around [40–200 nA] offering reasonable results, where magnitude and phase error offered is less than 10% within this range.

The evaluation of circuits is realized using the HIOKI 3522 HiTESTER LCR meter applying a differential input voltage 20 mV. A typical value of bias current I_o was chosen equal to 95 nA. The employed power supply voltages were set as $V_{DD} = -V_{SS} = 0.75$ V, and $V_{CM} = 0$ V.

Fig. 5.6 Experimental results of (a) magnitude and (b) phase for CPEs of order $\alpha = 0.3, 0.5, \text{ and } 0.7$ with $C_{eq} = 2.5 \text{ nF @ } 100 \text{ Hz}$



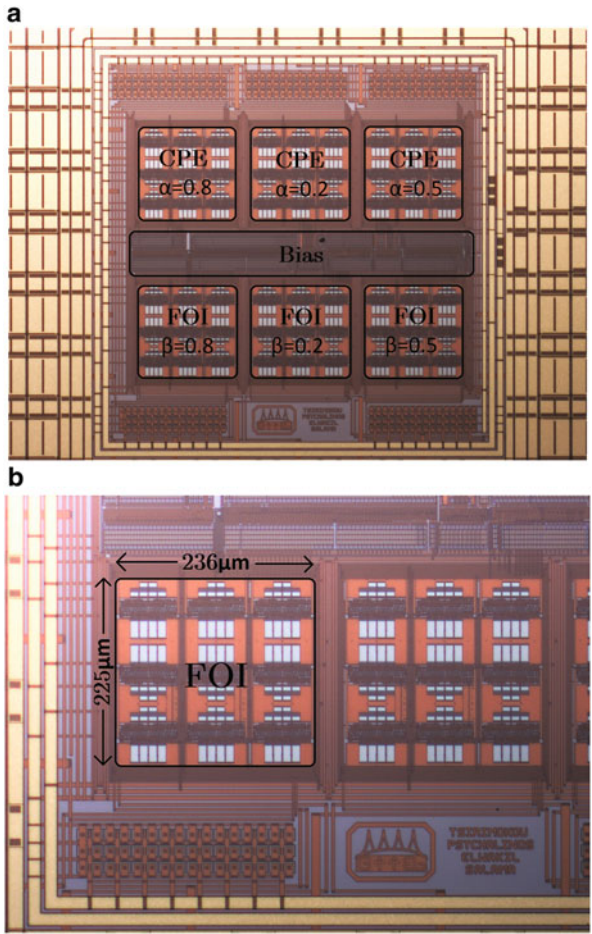
Thus, selecting a center frequency $\tau_u = 1/200\pi \text{ rad/sec}$ (i.e., 100 Hz), and using appropriate values for external capacitors being calculated from (5.29), the magnitude impedances for CPEs of order $\alpha = 0.3, 0.5, 0.7$ are shown in Fig. 5.6a.

The bestfit straight lines in the log-log scale for all orders show slopes of $-0.3, -0.44, -0.56, -0.64,$ and -0.75 which are very close to the desired ideal values, respectively.

The measured pseudo-capacitances C_α were calculated as $209.63\text{nF/sec}^{0.7}, 130.78\text{nF/sec}^{0.6}, 60.83\text{nF/sec}^{0.5}, 31.86\text{nF/sec}^{0.4},$ and $15.26\text{nF/sec}^{0.3}$, while the theoretical predicted values are $227\text{nF/sec}^{0.7}, 119\text{nF/sec}^{0.6}, 62.6\text{nF/sec}^{0.5}, 32.9\text{nF/sec}^{0.4},$ and $17.3\text{nF/sec}^{0.3}$, respectively. Figure 5.6b shows the measured impedance phase for the same CPEs compared with their theoretical phase angles of $-27^\circ, -45^\circ, -63^\circ$, respectively. Due to the limitations of the second-order approximation particularly as the fractional order increases, the phase error increases beyond 700 Hz. However, in the range 10–600 Hz, the phase error does not exceed 5° for all CPEs.

The second chip named *kpproj2* includes CPEs and FOIs with orders 0.2, 0.5, and 0.8 where kilo-Henry pseudo-inductances could be achieved. A die photo of

Fig. 5.7 (a) Die photo of the integrated fractional-order capacitors with fixed orders $\alpha = 0.2, 0.5, 0.8$, and fractional-order inductors with fixed orders $\beta = 0.2, 0.5, 0.8$. (b) die photo zoom on a single fractional-order inductor

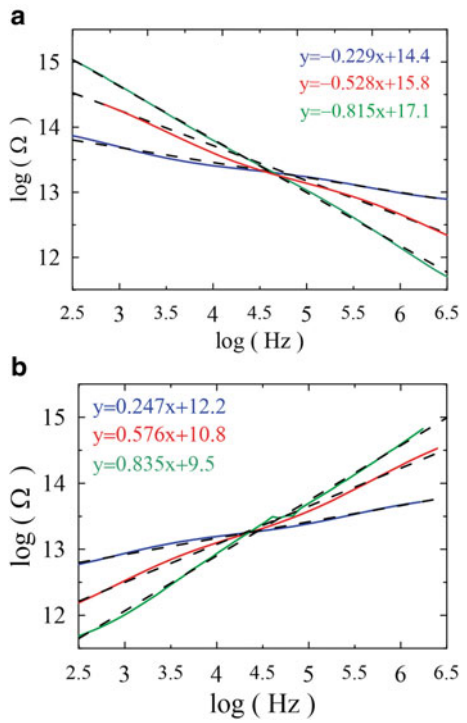


this work is shown in Fig. 5.7a, where each inductor emulator as shown in Fig. 5.7b measures $236 \mu\text{m} \times 225 \mu\text{m}$.

The employed power supply voltages were set as $V_{DD} = -V_{ss} = 0.75 \text{ V}$, and $V_{CM} = 0 \text{ V}$. Thus, selecting a center frequency $\tau_u = 1/200\pi \text{ rad/s}$ (i.e., 100 Hz), and using appropriate values for external capacitors being calculated from (5.29) and (5.30), when a typical value of bias current I_o equal to 95 nA was selected, the magnitude impedances for CPEs of order $\alpha = 0.2, 0.5, 0.8$, and FOIs of order $\beta = 0.2, 0.5, 0.8$ are shown in Fig. 5.8. The best fit straight lines in the log-log scale for all orders show slopes of $-0.23, -0.53$, and -0.81 for CPEs and of $0.25, 0.57$, and 0.84 for FOIs, which are very close to the desired ideal values, respectively.

The measured pseudo-capacitances C_α were calculated as $456.1 \text{ nF/sec}^{0.8}$, $67 \text{ nF/sec}^{0.5}$, $9.3 \text{ nF/sec}^{0.2}$, while the theoretical predicted values are $433 \text{ nF/sec}^{0.8}$,

Fig. 5.8 Experimental results of magnitude for (a) CPEs of order $\alpha = 0.2, 0.5,$ and 0.8 with $C_{eq} = 2.5$ nF @ 100 Hz, and (b) FOIs of order $\beta = 0.2, 0.5,$ and 0.8 with $L_{eq} = 1.014$ kH @ 100 Hz



62.6nF/sec^{0.5}, 9.1nF/sec^{0.2}, respectively. Also, the measured pseudo-inductances L_β were calculated as 164 kH/sec^{0.8}, 25.42 kH/sec^{0.5}, 4.1 kH/sec^{0.2}, while the theoretical predicted values are 175 kH/sec^{0.8}, 25.4 kH/sec^{0.5}, 3.7 kH/sec^{0.2}, respectively. Figure 5.9a shows the measured impedance phase for the same CPEs compared with their theoretical phase angles of $-18^\circ, -45^\circ, -72^\circ$, while Fig. 5.9b shows the measured impedance phase for the same FOIs compared with their theoretical phase angles of $18^\circ, 45^\circ, 72^\circ$.

Due to the limitations of the second-order approximation particularly as the fractional order increases, the phase error increases beyond 800 Hz. However, in the range 10–600 Hz, the phase error does not exceed 5° for all emulators. The investigation of tunability using different values of bias current for a fixed order is shown in Fig. 5.10. The variation of pseudo-inductances and phase for a fixed order $\beta = 0.5$ is readily obtained by applying bias currents (80 nA, 95 nA, 120 nA) and measured as $L_\beta = (32.14 \text{ k}, 25.42 \text{ k}, 18.91 \text{ k}) \text{ H/sec}^{0.5}$, which are very close to the theoretically predicted values (33.13 k, 25.4 k, 18.03 k) H/sec^{0.5}.

Fig. 5.9 Experimental results of phase for (a) CPEs of order $\alpha = 0.2, 0.5,$ and 0.8 with $C_{eq} = 2.5$ nF @ 100 Hz, and (b) FOIs of order $\beta = 0.2, 0.5,$ and 0.8 with $L_{eq} = 1.014$ kH @ 100 Hz

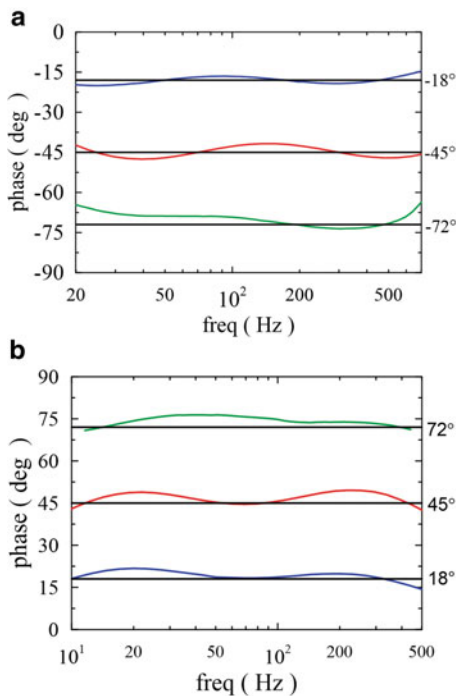
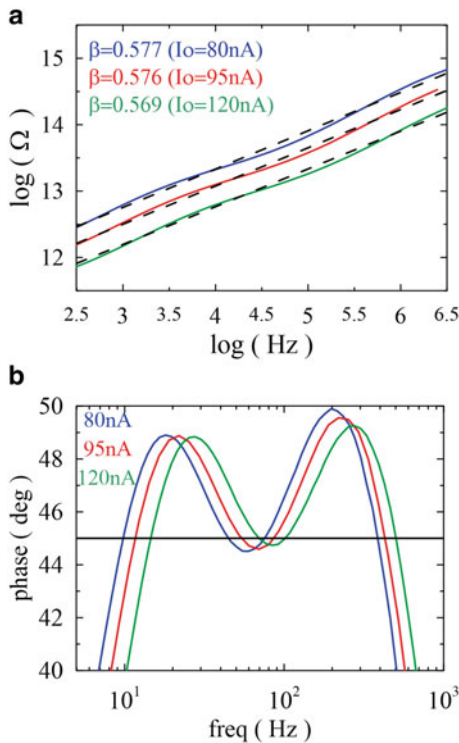


Fig. 5.10 Effect of tuning of bias current in the (a) magnitude and (b) phase of FOI of order $\beta = 0.5,$ and bias current $I_o = 80$ nA, 95 nA, and 120 nA



5.5 Fractional-Order Resonators Using Emulated CPEs and FOIs

Fractional-order-capacitors and inductors have been already mentioned as very important building blocks for several applications. The realization of a parallel resonance network using the already building blocks could result in one of the most simple and sensitive sensors. The behavior of the aforementioned network is essentially the same as a fractional-order band-pass filter as shown in Fig. 5.11. In case that the characteristics of building blocks could be easily tuned, then the proposed system could be used for precise calibration/measurement of an unknown fractional-order element. Thus, an attractive benefit of this topology is the capability of the fully characterization of the parameters (C_α , L_β , α , β) by solving two nonlinear equations. This could be achieved just through collecting data from a single ac frequency response.

In order to be completely described the mathematical background of a fractional-order parallel resonance, the topology ($RL_\beta C_\alpha$) of Fig. 5.11 will be analyzed. The realized transfer function of the aforementioned scheme is given in (5.31)

$$H(s) = \frac{\frac{1}{RC_\alpha} s^\beta}{s^{\alpha+\beta} + \frac{1}{RC_\alpha} s^\beta + \frac{1}{L_\beta C_\alpha}} \quad (5.31)$$

which could be alternatively expressed as

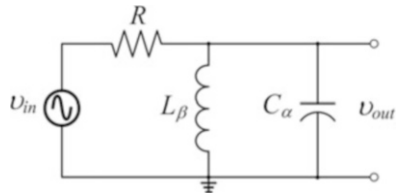
$$H(j\omega) = \text{Re}\{H(j\omega)\} + j\text{Im}\{H(j\omega)\} \quad (5.32)$$

where

$$\text{Re}\{H(j\omega)\} = \frac{\frac{1}{RC_\alpha} \omega^\beta \left[\omega^{(\alpha+\beta)} \cos\left(\frac{\alpha\pi}{2}\right) + \frac{1}{RC_\alpha} \omega^\beta \cos\left(\frac{\beta\pi}{2}\right) + \frac{1}{L_\beta C_\alpha} \right]}{\left[\omega^{(\alpha+\beta)} \cos\left(\frac{(\alpha+\beta)\pi}{2}\right) + \frac{1}{RC_\alpha} \omega^\beta \cos\left(\frac{\beta\pi}{2}\right) + \frac{1}{L_\beta C_\alpha} \right]^2 + \left[\omega^{(\alpha+\beta)} \sin\left(\frac{(\alpha+\beta)\pi}{2}\right) + \frac{1}{RC_\alpha} \omega^\beta \cos\left(\frac{\beta\pi}{2}\right) \right]^2} \quad (5.33a)$$

and

Fig. 5.11 $RL_\beta C_\alpha$ parallel resonator



$$\text{Im}\{H(j\omega)\} = \frac{\frac{1}{RC_a} \omega^\beta \left[-\omega^{(\alpha+\beta)} \cos\left(\frac{\alpha\pi}{2}\right) + \frac{1}{L_\beta C_a} \sin\left(\frac{\beta\pi}{2}\right) \right]}{\left[\omega^{(\alpha+\beta)} \cos\left(\frac{(\alpha+\beta)\pi}{2}\right) + \frac{1}{RC_a} \omega^\beta \cos\left(\frac{\beta\pi}{2}\right) + \frac{1}{L_\beta C_a} \right]^2 + \left[\omega^{(\alpha+\beta)} \sin\left(\frac{(\alpha+\beta)\pi}{2}\right) + \frac{1}{RC_a} \omega^\beta \cos\left(\frac{\beta\pi}{2}\right) \right]^2} \quad (5.33b)$$

The magnitude and phase responses of $H(j\omega)$ are, respectively, given by (5.34) and (5.35), respectively. An analysis of the magnitude response proves that the stop-band attenuation is asymmetric. More specific, the slope at high frequencies is $-6\cdot\alpha$ dB/oct, while at low frequencies is $+6\cdot\beta$ dB/oct. In addition, new critical frequencies have been added, compared to the conventional case of an integer-order resonance.

$$\begin{aligned} |H(j\omega)| &= \sqrt{\text{Re}\{H(j\omega)\}^2 + \text{Im}\{H(j\omega)\}^2} \\ &= \frac{\frac{1}{RC_a} \omega^\beta}{\sqrt{\omega^{2(\alpha+\beta)} + \left(\frac{\omega^\beta}{RC_a}\right)^2 + \frac{2\omega^{(\alpha+2\beta)}}{RC_a} \cos\left(\frac{\alpha\pi}{2}\right) + \frac{2\omega^\beta}{RL_\beta C_a^2} \omega^\beta \cos\left(\frac{\beta\pi}{2}\right) + \frac{2\omega^{(\alpha+\beta)}}{L_\beta C_a} \cos\left(\frac{(\alpha+\beta)\pi}{2}\right) + \left(\frac{1}{L_\beta C_a}\right)^2}} \end{aligned} \quad (5.34)$$

$$\begin{aligned} \angle H(j\omega) &= \tan^{-1} \left(\frac{\text{Im}\{H(j\omega)\}}{\text{Re}\{H(j\omega)\}} \right) \\ &= \tan^{-1} \left[\frac{-\omega^{(\alpha+\beta)} \sin\left(\frac{\alpha\pi}{2}\right) + \frac{1}{L_\beta C_a} \sin\left(\frac{\beta\pi}{2}\right)}{\omega^{(\alpha+\beta)} \cos\left(\frac{\alpha\pi}{2}\right) + \frac{1}{L_\beta C_a} \cos\left(\frac{\beta\pi}{2}\right) + \frac{1}{RC_a} \omega^\beta} \right] \end{aligned} \quad (5.35)$$

The definitions of these frequencies are the following

- Pure real frequency denoted as ω_{pr} at which the imaginary part of the transfer function becomes equal to zero (i.e., $\text{Im}\{H(j\omega)\} = 0$) and is given by

$$\omega_{\text{pr}} = \left(\frac{\sin\left(\frac{\beta\pi}{2}\right)}{L_\beta C_a \sin\left(\frac{\alpha\pi}{2}\right)} \right)^{\frac{1}{\alpha+\beta}} \quad (5.36)$$

It is important to be mentioned that when $\alpha = \beta = 1$ the above expression is simplified to $\omega_{\text{pr}} = \omega_r = \sqrt{1/LC}$, which is the well-known resonance frequency of

an integer-order resonator. Also, according to (5.35) the phase response at ω_{rp} is equal to 0 or π .

- The peak frequency (ω_p) at which the magnitude response has a maximum and is obtained by solving the equation $\frac{d}{d\omega}|H(j\omega)| = 0$. As a result, the peak frequency can be obtained by solving the following nonlinear equation

$$\alpha\omega_p^{2(\alpha+\beta)} + \frac{\alpha}{RC_a}\omega_p^{\alpha+2\beta}\cos\left(\frac{\alpha\pi}{2}\right) - \frac{\beta}{RL_\beta C_a^2}\omega_p^\beta\cos\left(\frac{\beta\pi}{2}\right) - \frac{\beta-a}{L_\beta C_a}\omega_p^{\alpha+\beta}\cos\left(\frac{(\alpha+\beta)\pi}{2}\right) - \frac{\beta}{(L_\beta C_a)^2} = 0. \quad (5.37)$$

It is obvious that in general, the peak frequency is different from the resonance frequencies either ω_{pr} or ω_r . Nevertheless, all the above frequencies are equalized only in case $\alpha = \beta = 1$. Then $\omega_p = \omega_{pr} = \omega_r = \sqrt{1/LC}$.

- Pure imagine frequency denoted as ω_{pi} at which the real part of the transfer function becomes equal to zero (i.e., $\text{Re}\{H(j\omega)\} = 0$) and is given by (5.38)

$$\omega_{pi}^{(\alpha+\beta)}\cos\left(\frac{\alpha\pi}{2}\right) + \frac{1}{RC_a}\omega_{pi}^\beta + \frac{1}{L_\beta C_a}\cos\left(\frac{\beta\pi}{2}\right) = 0 \quad (5.38)$$

Note that according to (5.35), the phase has a value equal to $\pm\pi/2$. This frequency exists only if the circuit has two elements at least, but at least one of them should be a fractional-order element.

- Half-power frequencies ω_h at which the power drops to half the passband power, i.e., $|H(j\omega)|_{\omega=\omega_h} = |H(j\omega)|_{\omega=\omega_p}/\sqrt{2}$, where ω_{h2} and ω_{h1} are the upper and lower half-power frequencies, respectively.

Assuming that a frequency scan is performed, using the magnitude and phase response can be easily measured the most important frequencies. Considering that there are four different equations that describe the most critical frequencies, then it is a trivial procedure for finding the four unknown parameters (C_α , L_β , α , β) of a fractional-order capacitor, and a fractional-order capacitor. In case that the inductor is not fractional, then the required equations are limited to be two, as there are only two unknown parameters (C_α , α), and only two measurements are required.

Considering the parallel resonator given in Fig. 5.11, there will be presented experimental results using the fabricated chip named *kpproj2*. Taking into account that in this project both fractional-order capacitors and inductors of order 0.2, 0.5, 0.8 are available, the evaluation of a fractional-order resonator could be easily verified. As a first step the impedance of the parallel resonator $L_\beta C_\alpha$ is tested using the same LCR meter.

A typical value of bias current I_o was chosen equal to 95 nA. Thus, selecting a center frequency $\tau_u = 1/200\pi$ rad/sec (i.e., 100 Hz), the resonator was tested for $C_\alpha = (433\text{n}, 62.6, 9.07)$ nF/sec $^{1-\alpha}$, and $L_\beta = (175.6, 25.4, 3.7)$ kH/sec $^{1-\beta}$ for orders

Fig. 5.12 (a) Magnitude and (b) phase measurements for the $L_\beta C_\alpha$ parallel resonator with $C_{\text{eq}} = 2.5$ nF, and $L_{\text{eq}} = 1.014$ kH @ 100 Hz, for various orders

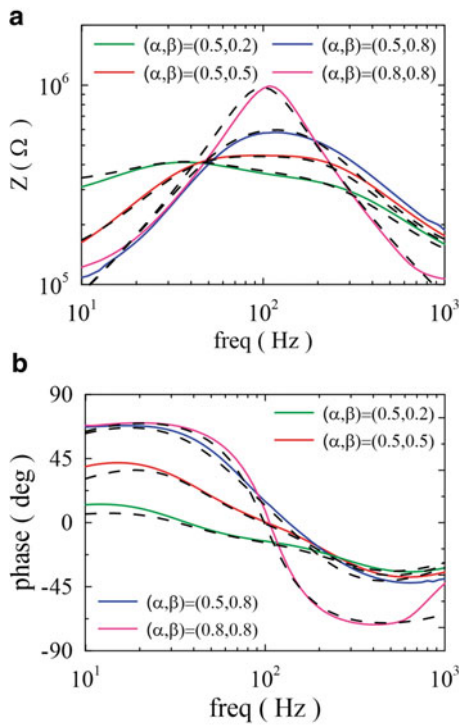


Table 5.4 Frequency characteristics of the $L_\beta C_\alpha$ resonator with $C_{\text{eq}} = 2.5$ nF, and $L_{\text{eq}} = 1.014$ kH @ 100 Hz

	$(\alpha, \beta) = (0.5, 0.2)$	$(\alpha, \beta) = (0.5, 0.5)$	$(\alpha, \beta) = (0.5, 0.8)$	$(\alpha, \beta) = (0.8, 0.8)$
f_p (Hz)	36.7 (38.2)	92.84 (100)	116 (121.3)	107.7 (100)
$ Z(j2\pi f_p) $ (Ω)	411.2 k (408.8 k)	444.5 k (439.8 k)	580.5 k (600.6 k)	991.7 k (984.8 k)
f_{pr} (Hz)	38.1 (33.4)	103 (100)	134 (130)	105 (100)

0.2, 0.5, and 0.8, respectively. Applying a differential input signal 20 mV, the magnitude and phase responses for various cases of (α, β) are shown in Fig. 5.12. The obtained results are summarized in Table 5.4, where the corresponding theoretical predicted values are also given between parentheses.

Concerning the affection of bias current in the magnitude and phase of the resonator for a fixed order $\alpha = \beta = 0.5$ is demonstrated in Fig. 5.13. The derived experimental results are given in Table 5.5. As a result, the affection of bias current is in accordance with the study already given in previously.

After that, the circuit of Fig. 5.11 is tested, which is essentially a fractional-order band-pass filter, using different values of R . As a first step, fixing $R = 1$ M Ω , and using the already tested $L_\beta C_\alpha$ setup with $C_{\text{eq}} = 2.5$ nF and $L_{\text{eq}} = 1.014$ kH @ 100 Hz, the obtained results of fractional-order bandpass filter of order $\alpha = \beta = 0.5$ are demonstrated in Fig. 5.14.

Fig. 5.13 (a) Magnitude and (b) phase measurements for the $L_{0.5}C_{0.5}$ parallel resonator with order 0.5 at bias currents (80 nA, 95 nA, 120 nA)

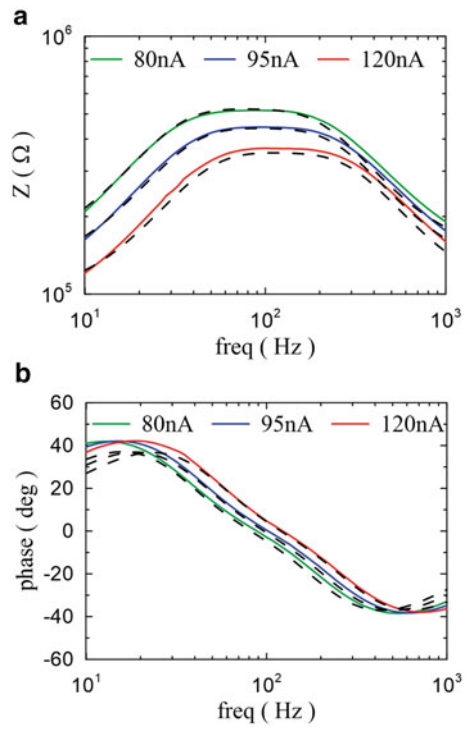


Table 5.5 Frequency characteristics of the fractional-order $L_{0.5}C_{0.5}$ resonator with $C_{eq} = 2.5$ nF, and $L_{eq} = 1.014$ kH @ 100 Hz for three different bias currents

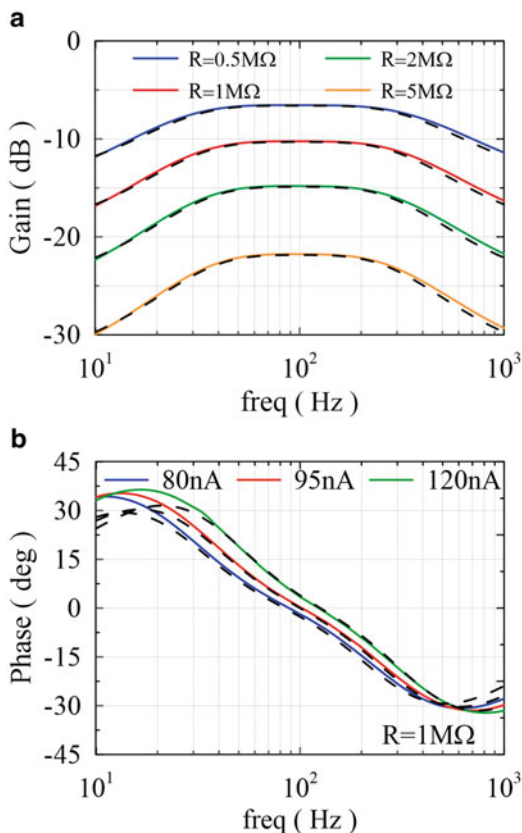
$(\alpha = \beta = 0.5)$	$I_o = 80$ nA	$I_o = 95$ nA	$I_o = 120$ nA
f_p (Hz)	80 (83.69)	92.84 (100)	100 (125.3)
$ Z(j2\pi f_p) $ (Ω)	516.3 (525.1 K)	444.5 K (439.8 K)	368.3 K (350.1 K)
f_{pr} (Hz)	89.5 (83.5)	103 (100)	123 (125.3)

In addition, a comparison of the magnitude response for different cases ($R = 0.5, 1, 2, 5$) $M\Omega$, with bias current being fixed at 95 nA, is simultaneously given. The gain at f_p was measured (-6.54 dB, -10.24 dB, -14.81 dB, -21.76 dB), respectively.

5.6 Summary

A fractional-order capacitor and inductor emulator is fully integrated, the right operation of which has been verified through experimental results. The basic building blocks are g_m -cells with MOS transistors operating in the subthreshold

Fig. 5.14 (a) Magnitude and (b) phase measurements for the $RL_{0.5}C_{0.5}$ parallel resonator at $I_o = 95$ nA with $R = (0.5, 1, 2, 5)$ M Ω



region offering electronic tunability through bias current. Having available those emulators, an $L_{\beta}C_{\alpha}$ parallel resonator, as well as a fractional-order bandpass filter, is possible to be realized. The experimental results prove that the fabricated circuit offers a good accuracy, when compared to theoretical values. The main benefit of this resonator is that it can be operated in a low frequency operation, which is a very difficult procedure using the circuits already reported in the literature [7, 8].

References

1. Elwakil, A.S.: Fractional-order circuits and systems: an emerging interdisciplinary research area. *IEEE Circ. Syst. Mag.* **10**(4), 40–50 (2010)
2. Oldham, K.B.: *The Fractional Calculus*. Elsevier, London (1974)
3. Westerlund, S., Ekstam, L.: Capacitor theory. *IEEE Trans. Dielectr. Electr. Insul.* **1**(5), 826–839 (1994)
4. Yufera, A., Rueda, A., Munoz, J.M., Doldan, R., Leger, G., Rodriguez-Villegas, E.O.: A tissue impedance measurement chip for myocardial ischemia detection. *IEEE Trans. Circ. Syst. I: Regul. Pap.* **2**(12), 2620–2628 (2005)

5. Rodriguez, S., Ollmar, S., Waqar, M., Rusu, A.: A battery sensor ASIC for implantable bio-impedance applications. *IEEE Trans. Biomed. Circ. Syst.* **10**(3), 533–544 (2016)
6. Tripathy, M., Mondal, D., Biswas, K., Sen, S.: Experimental studies on realization of fractional inductors and fractional-order bandpass filters. *Int. J. Circ. Theory Appl.* **2014**, 98 (2014)
7. Freeborn, T.J., Maundy, B., Elwakil, A.S.: Field programmable analogue array implementation of fractional step filters. *IET Circ. Dev. Syst.* **4**(6), 514–524 (2010)
8. Adhikary, A., Sen, S., Biswas, K.: Practical realization of tunable fractional order parallel resonator and fractional order filters. *IEEE Trans. Circ. Syst. I: Fundam. Theory. Appl.* **63**(8), 1142–1151 (2016)

Chapter 6

Applications of Fractional-Order Circuits

6.1 Introduction

Fractional-order calculus consists one of the most important mathematical tools, which offer attractive features when applied in several applications. The most important features are highlighted especially when compared with the corresponding integer-order counterparts. The first topology that utilizes and proves this feature is using a fractional-order differentiator in the preprocessing chain for detecting the QRS complexes according to the Pan-Tompkins algorithm, where the efficiency of handling signals in a noisy environment has been achieved and proved through simulation results. A fully tunable impedance model using the already proposed fractional-order capacitors and inductor emulators will be realized and verified through simulation results. This emulator is capable of emulating models representing the impedance of many types of biological tissues. The characterization of fractional-order circuits is an important procedure, which in general requires expensive equipment. Thus, appropriate experimental setups are introduced, which are very simple and cost-effective alternative using operational amplifier-based circuits. Finally, the design and evaluation of a fractional-order oscillator is introduced proving that fractional-order oscillators have a unique advantage when compared to their integer-order counterparts. That is the capability of producing higher frequencies for the same inductance and capacitance values as a result of the existence of one or more fractional-order differential equations.

6.2 A Preprocessing Stage Suitable for Implementation of the Pan-Tompkins Algorithm

Fractional-order differentiators and integrator topologies, which are the most important building blocks, are designed by employing the concept of the Sinh-Domain filtering. Companding technique offers the benefits of resistorless realizations with potential for adjusting their frequency characteristics through appropriate DC currents. In addition, they are capable for operating in an ultralow-power supply environment, which is very important from the nowadays trend point of view. The performance of the proposed blocks has been evaluated through the Analog Design Environment of the Cadence software, using MOS transistor models provided by the TSMC 180 nm process.

The distinct characteristic of the technique is that, it is the large-signal transfer function of the circuit that is linearized, not the individual transconductance or active resistive elements as would be the case in conventional circuit design techniques. In addition, the frequency characteristics could be electronic adjusted through bias currents. The absence of passive resistors and the employment of only grounded capacitors constitute attractive features making them efficient blocks for realizing high performance circuit topologies. Also, the realization of companding filters using MOS transistors biased in the weak inversion offers the capability of operation in an ultralow-voltage environment [1–8]. The general topology of a linear system, the principle of which is that the input current is compressed into a voltage in order to be processed from the core of the system and then the output voltage expanded into a linear current at the output of the system, is given in Fig. 6.1.

Taking into account that MOS transistors operating in the subthreshold region will be employed, the proposed topologies are able to operate in ultra low-voltage environment with reduced power consumption. Thus, the preservation of the linear operation of the system has been achieved through the utilization of the following set of complementary operators

$$\hat{v}_{in} = [\sinh^{-1}(i_{in})] \equiv V_{DC} + nV_T \cdot \sinh^{-1}\left(\frac{i_{in}}{2I_B}\right) \quad (6.1)$$

$$i_{out} = [\sinh(\hat{v}_{out})] \equiv 2I_B \cdot \sinh\left(\frac{\hat{v}_{out} - V_{DC}}{nV_T}\right) \quad (6.2)$$

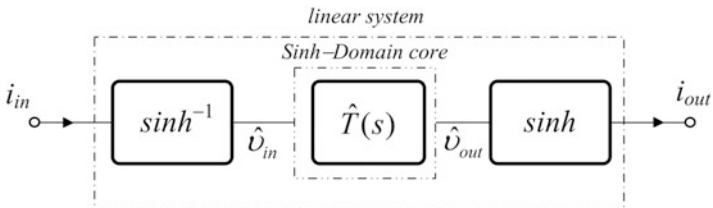


Fig. 6.1 Realization of a linear system using companding technique in Sinh-Domain

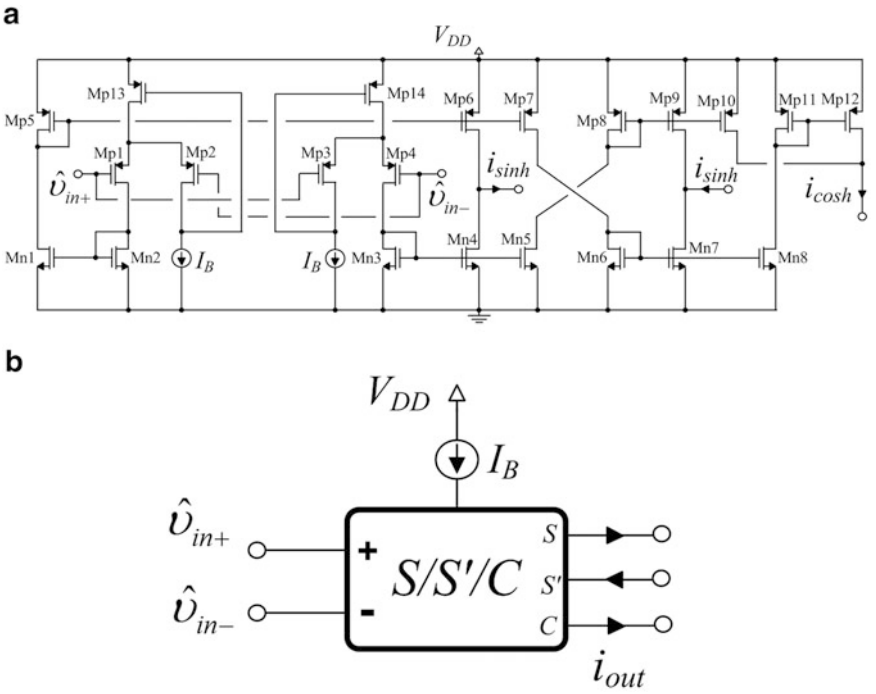


Fig. 6.2 Multiple-output nonlinear transconductor cell (a) circuitry and (b) associated symbol

where I_B is a bias current, n is the subthreshold slope factor ($1 < n < 2$), V_T is the thermal voltage (≈ 26 mV at 27°C), \hat{v}_{in} and \hat{v}_{out} are the compressed input and output voltages, and i_{in} , i_{out} are the linear input and output currents, respectively.

The conversion of the linear input current into a compressed voltage is described through the $[\sinh^{-1}]$ operator in (6.1), while the conversion of the compressed output voltage into a linear current through the $[\sinh]$ operator in (6.2). The fundamental elements for realizing Sinh-Domain circuits are nonlinear transconductor cells, known as S and C cells [4, 7–12]. A typical multiple-output cell is depicted in Fig. 6.2. Thus, following this consideration, the expressions of output currents are given by Eqs. (6.3) and (6.4), where \hat{v}_{in+} and \hat{v}_{in-} are the voltages at the non-inverting and inverting inputs, respectively.

$$i_{\sinh} = \sinh(\hat{v}) \equiv 2I_B \cdot \sinh\left(\frac{\hat{v}_{in+} - \hat{v}_{in-}}{nV_T}\right) \quad (6.3)$$

$$i_{\cosh} = \cosh(\hat{v}) \equiv 2I_B \cdot \cosh\left(\frac{\hat{v}_{in+} - \hat{v}_{in-}}{nV_T}\right) \quad (6.4)$$

Additional replicas of the output currents could be derived through the formation of extra current mirrors.

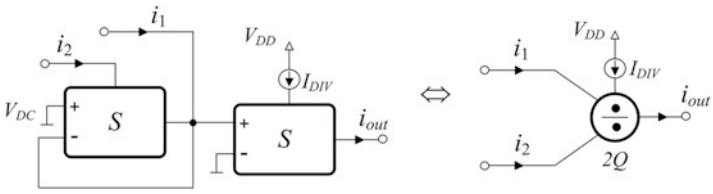


Fig. 6.3 Two-quadrant divider realization (a) using S cells and (b) associated symbol

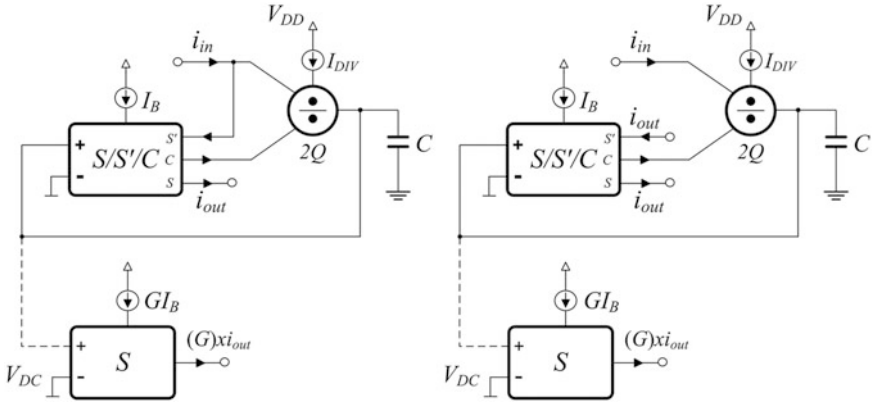


Fig. 6.4 General schemes of Sinh-Domain (a) lossless and (b) lossy integrators

Another useful building block for realizing Sinh-Domain integrators is the two-quadrant divider. That topology is realized using appropriately configured S cells as it is demonstrated in Fig. 6.3 with the associated symbol.

The input–output relationship is given by the formula $i_{out} = I_{DIV} \cdot (i_1/i_2)$, where i_1 and i_2 are the corresponding input currents, and I_{DIV} is the bias current of divider [8].

Using the aforementioned cells, the general topology of a Sinh-Domain lossless integrator is demonstrated in Fig. 6.4. The current that flows through the capacitor is derived as

$$i_c = C \frac{d\hat{v}_{out}}{dt} = 2I_{DIV} \cdot \frac{2I_B \cdot \sinh\left(\frac{\hat{v}_{in} - V_{DC}}{nV_T}\right)}{2I_B \cdot \cosh\left(\frac{\hat{v}_{out} - V_{DC}}{nV_T}\right)} \quad (6.5)$$

Taking into account that the input–output current relationship of the two-quadrant divider is $i_{out} = I_{DIV}(i_1/i_2)$, then using (6.2) the expression in (6.5) could be written as

$$\tau \cdot \frac{d}{dt} [\sinh(\hat{v}_{out})] = [\sinh(\hat{v}_{in})] \Leftrightarrow \tau \cdot \frac{d}{dt} i_{out} = i_{in} \quad (6.6)$$

Thus, the derived transfer function of lossless integrator is proved and given as

$$H(s) = \frac{1}{\tau \cdot s} \quad (6.7)$$

where the time constant (τ) is given by (6.8)

$$\tau = \frac{CnV_T}{I_{DIV}} \quad (6.8)$$

In case that a scaled output is also needed, the enhanced topology is also depicted in Fig. 6.4a. This has been achieved through adding an extra S cell, which is biased at a current $G \cdot I_B$. The modified output current of this S cell is given by (6.9), while using (6.3), (6.7), and (6.9) the transfer function is given by (6.10)

$$i_{out(\times G)} = 2GI_B \cdot \sinh\left(\frac{\hat{v}_{in+} - \hat{v}_{in-}}{nV_T}\right) \quad (6.9)$$

$$H(s)_{(\times G)} = \frac{G}{\tau \cdot s} \quad (6.10)$$

Taking into account that the required time constants are realized through the bias current of the divider (I_{DIV}) [13], the electronic adjustment of the gain factor (G) of the transfer function is realized through DC bias current of the corresponding nonlinear transconductor without disturbing the time constant of the filter.

Following a similar procedure, the corresponding lossy integrator is demonstrated in Fig. 6.4b. The realized transfer functions will be given by (6.11) and (6.12), while the time constant is still given by Eq. (6.8).

$$H(s) = \frac{1}{\tau \cdot s + 1} \quad (6.11)$$

$$H(s)_{(\times G)} = \frac{G}{\tau \cdot s + 1} \quad (6.12)$$

Taking into account that the expression of the time constant in Eq. (6.8) is depended on the bias current I_{DIV} , the range of the input signals which could be handled by the integrator is not limited by the value of the bias current which is employed for biasing the nonlinear $S/S'/C$ cell. As a result, the topologies in Fig. 6.4 offer the capability for realizing large time constants without affecting the level of input currents, i.e., they behave as capacitor multipliers with scaling factor equal to $2I_B/I_{DIV}$ [13].

Another important block for realizing circuits in Sinh-Domain is a multiple-output summation block with a scaled output. The proposed topology is depicted in Fig. 6.5, where according to (6.1), the voltage could be written as given in (6.13). The two S cells at the right of the figure are biased at currents I_B and $G \cdot I_B$, and their

Fig. 6.5 Realization of summation in the Sinh-Domain

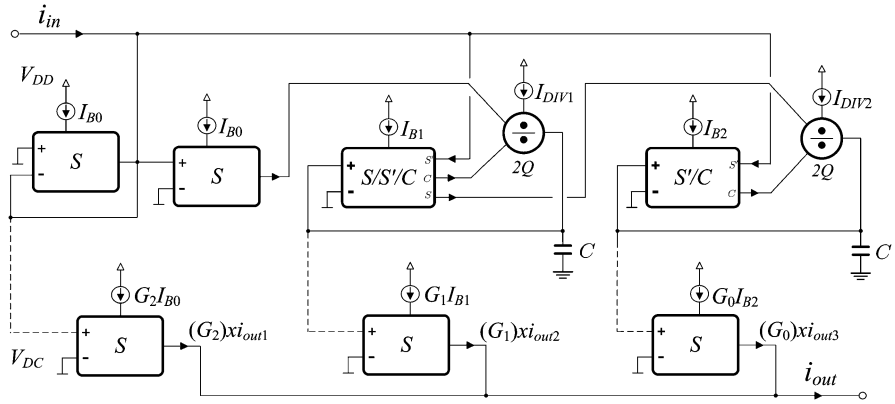
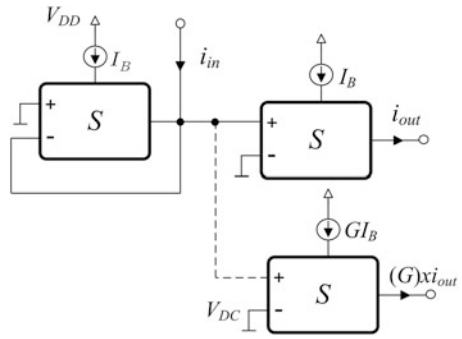


Fig. 6.6 Sinh-Domain realization of the fractional-order differentiator of order α , using the second-order approximation in (1.6)

corresponding outputs could be expressed, using (6.3), as $i_{out} = (i_1 + i_2)$ and $i_{out(\alpha G)} = G \cdot (i_1 + i_2)$.

$$\hat{v}_{in} = V_{DC} + nV_T \cdot \sinh^{-1} \left(\frac{i_1 + i_2}{2I_0} \right) \quad (6.13)$$

The realization of a fractional-order differentiator/integrator blocks will be performed using the procedure presented in Chap. 2. The transfer function given in (2.6) is capable for approximating a fractional-order differentiator, a fractional-order lossless and lossy integrator using the same topology without any modification. Assuming that companding is a current mode technique, the realization of this topology could be derived using the FBD given in Fig. 2.1a.

Thus, the Sinh-Domain realization is that depicted in Fig. 6.6. For the sake of completeness the expressions of gain values G_j ($j = 0, 1, 2$) and time constants τ_j ($i = 1, 2$) using the second-order approximation given in (1.6), are summarized in Table 6.1.

Table 6.1 Values of scaling factors G_j , τ_i , and bias currents for realizing fractional-order differentiator, lossless, and lossy integrator of order α , using the second-order approximation in (1.6)

Design parameters	$H(s) = (\tau \cdot s)^\alpha$	$H(s) = \frac{1}{(\tau \cdot s)^\alpha}$	$H(s) = \frac{1}{(\tau \cdot s)^\alpha + 1}$
G_2	$\left(\frac{\alpha^2 + 3\alpha + 2}{\alpha^2 - 3\alpha + 2}\right)$	$\left(\frac{\alpha^2 - 3\alpha + 2}{\alpha^2 + 3\alpha + 2}\right)$	$\left(\frac{\alpha^2 - 3\alpha + 2}{2\alpha^2 + 4}\right)$
G_1	1	1	0.5
G_0	$\left(\frac{\alpha^2 - 3\alpha + 2}{\alpha^2 + 3\alpha + 2}\right)$	$\left(\frac{\alpha^2 + 3\alpha + 2}{\alpha^2 - 3\alpha + 2}\right)$	$\left(\frac{\alpha^2 + 3\alpha + 2}{2\alpha^2 + 4}\right)$
τ_1	$\left(\frac{\alpha^2 - 3\alpha + 2}{-2\alpha^2 + 8}\right) \cdot \tau$	$\left(\frac{\alpha^2 + 3\alpha + 2}{-2\alpha^2 + 8}\right) \cdot \tau$	$\left(\frac{\alpha^2 + 2}{-2\alpha^2 + 8}\right) \cdot \tau$
τ_2	$\left(\frac{-2\alpha^2 + 8}{\alpha^2 + 3\alpha + 2}\right) \cdot \tau$	$\left(\frac{-2\alpha^2 + 8}{\alpha^2 - 3\alpha + 2}\right) \cdot \tau$	$\left(\frac{-2\alpha^2 + 8}{\alpha^2 + 2}\right) \cdot \tau$
I_{DIV1}	$\kappa_1 \kappa_2 n C V_T \omega_o \left(\frac{-2\alpha^2 + 8}{\alpha^2 - 3\alpha + 2}\right)$	$\kappa_1 \kappa_2 n C V_T \omega_o \left(\frac{-2\alpha^2 + 8}{\alpha^2 + 3\alpha + 2}\right)$	$\kappa_1 \kappa_2 n C V_T \omega_o \left(\frac{-2\alpha^2 + 8}{\alpha^2 + 2}\right)$
I_{DIV2}	$\kappa_1 \kappa_2 n C V_T \omega_o \left(\frac{\alpha^2 + 3\alpha + 2}{-2\alpha^2 + 8}\right)$	$\kappa_1 \kappa_2 n C V_T \omega_o \left(\frac{\alpha^2 - 3\alpha + 2}{-2\alpha^2 + 8}\right)$	$\kappa_1 \kappa_2 n C V_T \omega_o \left(\frac{\alpha^2 + 2}{-2\alpha^2 + 8}\right)$

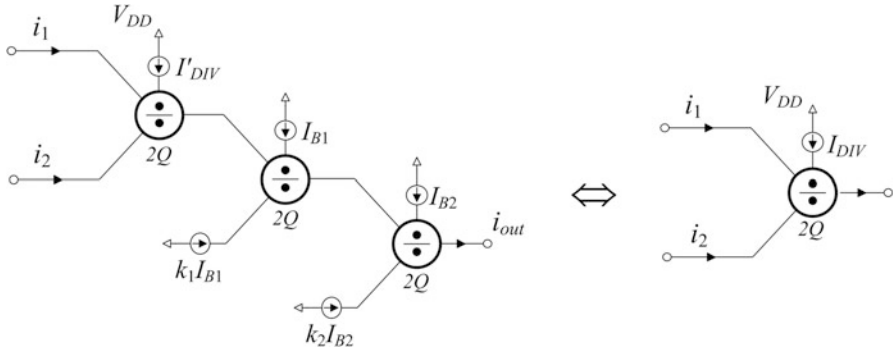


Fig. 6.7 Enhanced version of a two-quadrant divider

Due to the large spread of values of DC bias current of divider observed at the realization of various orders of fractional-order topologies, the enhanced version of the two-quadrant divider as that given in Fig. 6.7 will be employed. The bias current that has been achieved using two more extra stages than the conventional counterpart is $I_{DIV} = I'_{DIV}/(\kappa_1 \cdot \kappa_2)$, giving an additional degree of freedom in the implementation point of view. Thus, the resulted design equations for the appropriate bias currents are also given in Table 6.1.

The electrocardiogram (ECG) is a powerful tool for noninvasively diagnosing cardiac diseases. An important research subject is the detection of QRS complex in an ECG. The Pan-Tompkins algorithm is one of the most popular methods for detecting the QRS complexes [14, 15]. The QRS detection task is difficult due to the time-varying morphology of ECG, the physiological variability of the QRS

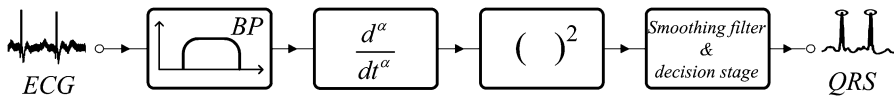


Fig. 6.8 Block diagram for implementing the Pan-Tompkins algorithm using fractional-order differentiator of order α

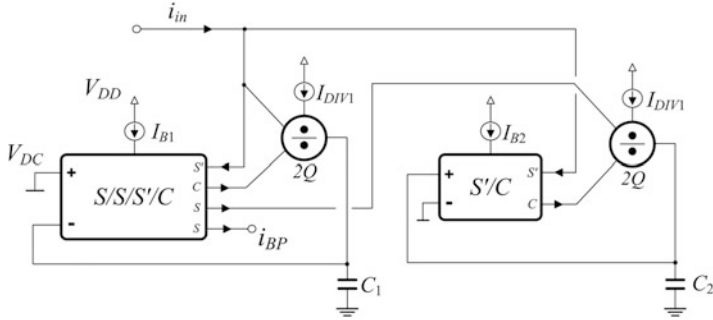


Fig. 6.9 Sinh-Domain realization of the second-order bandpass filter

complexes, and the noise presented in ECG signals. The main noise sources are muscular activity, movement artifacts, power line interference, and baseline wandering [16, 17]. Fractional-order differentiation is an attractive mathematical tool for features extraction from noisy signals, especially when compared to the conventional integer-order calculus. Fractional-order operators accumulate, in a weighted form, the whole information of the signal [18, 19, 20].

A typical preprocessing chain of the Pan-Tompkins algorithm consists of a typical bandpass filter, a differentiator, and squarer. The bandpass filter is responsible for the selection of frequencies between QRS complex of the ECG signal. Thereafter, the differentiator finds the high slopes of the signal, and finally the squarer is used in order to emphasize the higher frequency content of the signal, which is unique characteristic of QRS complex compared to the other ECG waves. The modified chain using the fractional-order differentiator is that given in Fig. 6.8.

The BP filter has been realized through a two-integrator loop as that demonstrated in Fig. 6.9; the transfer function is the following

$$H(s) = \frac{\frac{\omega_0}{Q} \cdot s}{s^2 + \frac{\omega_0}{Q} \cdot s + \omega_0^2} \quad (6.14)$$

The resonance frequency ω_0 and the Q factor are defined by (6.15) and (6.16)

$$\omega_0 = \frac{1}{\sqrt{\tau_1 \tau_2}} \quad (6.15)$$

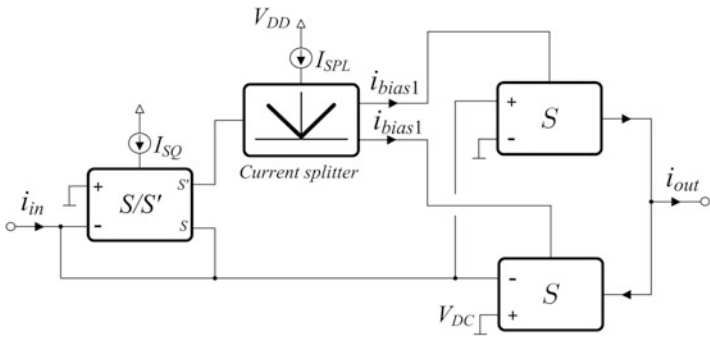


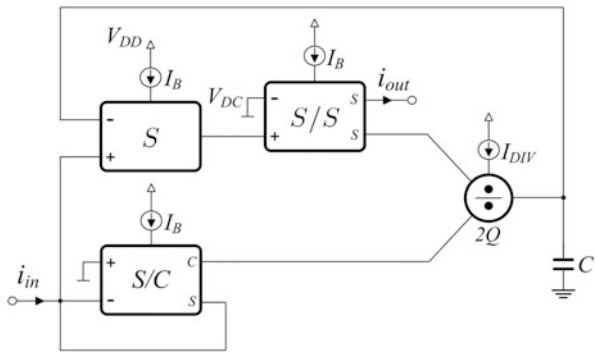
Fig. 6.10 Sinh-Domain realization of the current squarer

$$Q = \sqrt{\frac{\tau_1}{\tau_2}} \quad (6.16)$$

where the time constants τ_i ($i = 1, 2$) are given by the expression $\tau = nCV_T/I_{DIV}$. Considering that the bias scheme is $V_{DD} = 0.5$ V, $V_{DC} = 200$ mV, $I_{B1} = I_{B2} = 50$ pA, and $I_{DIV1} = I_{DIV2} = 100$ pA, the capacitor values for realizing a bandpass filter function with cutoff frequencies 5 and 15 Hz were $C_1 = 47$ pF and $C_2 = 62.6$ pF. The simulated values of cutoff frequencies were 5.1 Hz and 14.6 Hz, respectively. The required current squaring operation has been realized by the topology given in Fig. 6.10, which is actually a four-quadrant multiplier [12, 21, 22]. The circuitry of the current splitter is shown in Fig. 3.6, and the realized expression for the output current is $i_{out} = i_{in}^2/I_{SQ}$, where I_{SQ} is a DC bias current. The aspect ratios of the MOS transistors, for a bias current $I_{SQ} = I_{SPL} = 200$ pA, are $34 \mu\text{m}/15 \mu\text{m}$ for M_{p1} – M_{p4} , $40 \mu\text{m}/10 \mu\text{m}$ for M_{p5} – M_{p6} , $4 \mu\text{m}/10 \mu\text{m}$ for M_{p7} – M_{n9} , and $10 \mu\text{m}/15 \mu\text{m}$ for M_{n1} – M_{n4} .

In order to be evident the efficiency of the proposed topology, Pan-Tompkins algorithm will be also studied for the integer-order differentiator. The Sinh-Domain of an integer-order differentiator is that depicted in Fig. 6.11 [23]. Thus, all the intermediate blocks are ready for being utilized in order to perform the Pan-Tompkins algorithm. As a first step, the ECG signal should be applied at the input of the system. A noiseless ECG, which is derived through the MATLAB toolbox available in [24] is given in Fig. 6.12a. A noisy ECG, obtained through the addition of Gaussian noise (*awgn* command of MATLAB) with signal-to-noise ratio (SNR) equal to 0 dB. The aforementioned signal is depicted in Fig. 6.12b. Therefore, the obtained waveforms, which have been performed at transistor level, using the time-domain analysis tool provided by the Analog Design Environment of the Cadence software are realistic. The waveform at the output of the bandpass filter for both systems is depicted in Fig. 6.12c. The waveforms after the integer-order and fractional-order differentiation with unity gain frequency 10 Hz are demonstrated in Fig. 6.12d, e, respectively. It is obvious that the noise at the output of the

Fig. 6.11 Sinh-Domain realization of the integer-order differentiator



fractional-order differentiator is significantly suppressed. As a result, the output waveform in Fig. 6.12g is less noisy than that of Fig. 6.12f.

Consequently, the proposed fractional-order differentiator that has been utilized offers more efficient results than that of integer-order realization.

6.3 A fully Tunable Implementation of the Cole-Cole Model

Fractional-order capacitors have been already mentioned as very important building blocks in several applications especially in the field of bioimpedance, which measures the passive electrical properties of biological materials. These measurements give information about the electrochemical process in tissues and can be used to characterize the tissue or monitor for physiological changes. In the field of bioimpedance measurements the Cole impedance model, introduced by Kenneth Cole in 1940 [25], is widely used for characterizing biological tissues and biochemical materials. The Cole-impedance model is widely popular to biology and medicine [26], due to its simplicity and good fit with measured data, illustrating the behavior of impedance as a function of frequency.

The single-dispersion Cole model, shown in Fig. 6.13, is composed of three hypothetical circuit elements: (i) a high-frequency resistor R_∞ , (ii) a low-frequency resistor R_0 , and (iii) a fractional-order capacitor (C_α, α). The impedance of the Cole-model is given by (6.17).

$$Z(s) = R_\infty + \frac{R_0 - R_\infty}{1 + (\tau s)^\alpha} \quad (6.17)$$

where

$$s^\alpha = (\omega)^\alpha \left[\cos\left(\frac{\alpha\pi}{2}\right) + j \sin\left(\frac{\alpha\pi}{2}\right) \right]$$

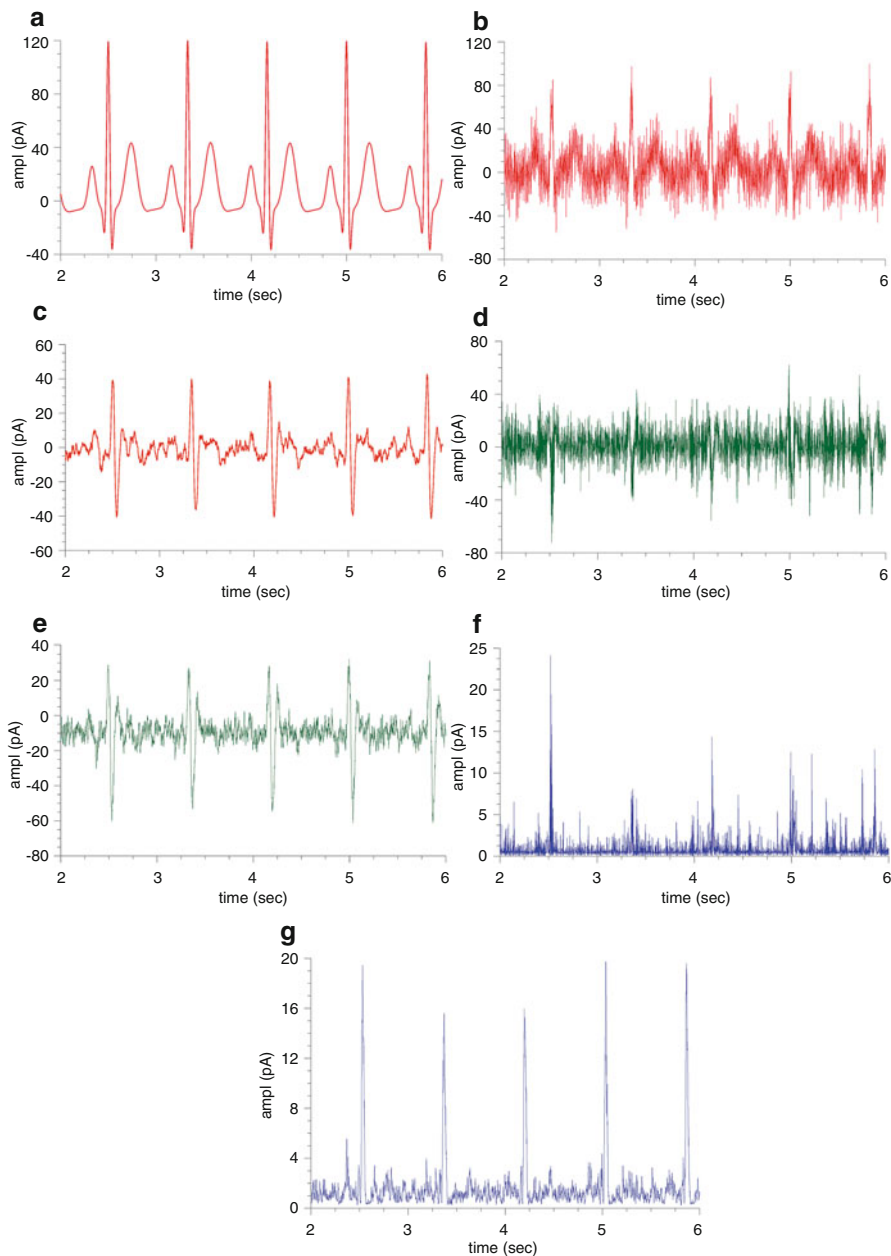


Fig. 6.12 Simulated waveforms for (a) noiseless ECG, (b) noisy ECG, (c) output of the bandpass filter, (d) output of the integer-order differentiator, (e) output of the fractional-order differentiator, (f) output of the squarer after an integer-order differentiation, and (g) output of the squarer after a fractional-order differentiation

Fig. 6.13 Theoretical Cole-impedance model

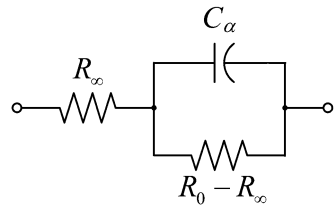


Fig. 6.14 OTA structure realization for emulating a floating resistor

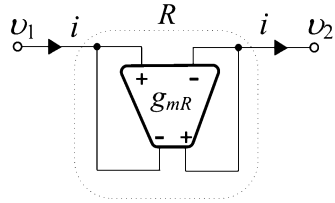


Table 6.2 Cole-impedance parameters extracted from an apple and plumb

Parameter	Apple	Plumb
α	0.696	0.64
R_∞ (Ω)	195 k	42.4 k
R_0 (Ω)	2.414 M	1.02 M
C_α ($F/sec^{1-\alpha}$)	511 p	2.09 n

Table 6.3 Bias currents and scaling factors for the emulation of the Cole-impedance model parameters of the apple and plumb model described in Table 6.2

Parameter	Apple	Plumb
I_{o1}	1.84 μA	1.33 μA
$I'_{o} = I_{o2}$	67.6 nA	54.5 nA
G_2	11.53	8.843
G_1	1	1
G_0	0.087	0.113
$I_{R0} - I_{R\infty}$	27.4 nA	61 nA
I_{R0}	312 nA	1.4 μA

A fully-tunable Cole-impedance emulator can be realized using the proposed current excited fractional-order capacitor given in Fig. 5.3 and replacing the passive resistors by appropriately configured OTAs, the topology of which is that given in Fig. 6.14, where the transconductance value is given as $g_m = 1/R$.

In order to demonstrate a complete model, the Cole-impedance model parameters previously extracted from an apple and plumb in [27] are used.

These parameters, which are scaled by a factor of 100 in order to be able emulated by this design, are summarized in Table 6.2. The appropriate values for bias currents and scaling factors are given in Table 6.3 for both models which are calculated using the design equations given in Table 5.1 and (5.16–5.17).

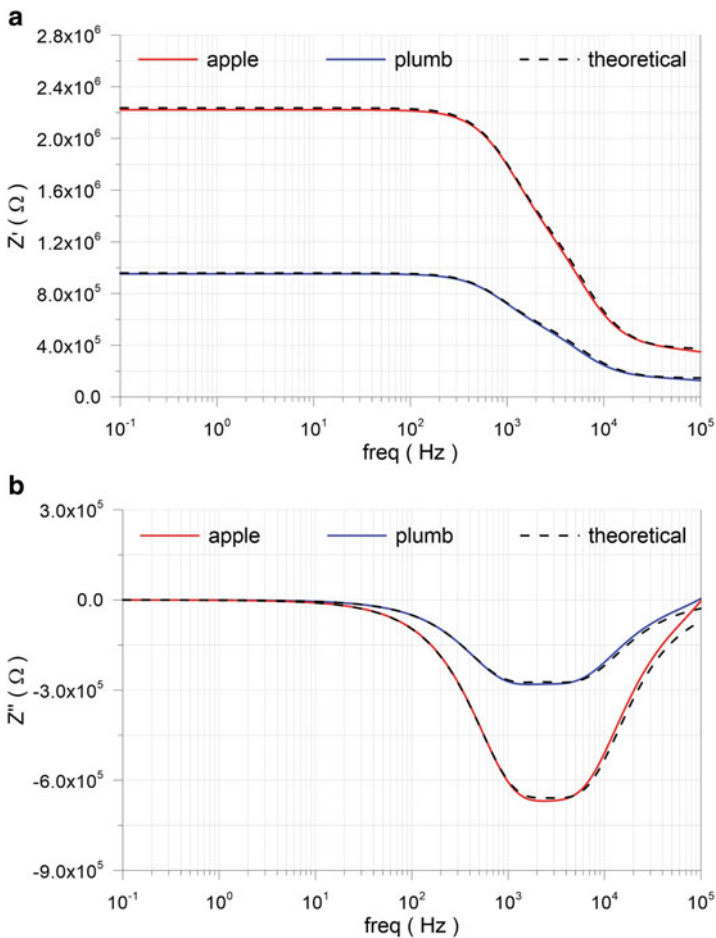


Fig. 6.15 Post-layout simulation results of the (a) real and (b) imaginary part of Cole-impedance model for the apple and plumb model parameters

The MOS transistor aspect ratios for the OTAS emulating floating resistors are $10\ \mu\text{m}/10\ \mu\text{m}$ for $M_{b1}-M_{b3}$, $50\ \mu\text{m}/1\ \mu\text{m}$ for $M_{n1}-M_{n4}$, $10\ \mu\text{m}/1\ \mu\text{m}$ for $M_{n2}-M_{n3}$, and $60\ \mu\text{m}/10\ \mu\text{m}$ for $M_{p1}-M_{p2}$.

The real $Z'(\Omega)$ and imaginary part $Z''(\Omega)$ of impedance derived using post-layout simulation results are given in Fig. 6.15, where the corresponding theoretical simulations (dashed lines) are also given. In addition, the Nyquist plot of the emulated Cole-impedances is given in Fig. 6.16, while the corresponding theoretical simulations are also given. The well-known form of the semicircle is presented using this format, while the maximum and minimum values of impedances for both apple and plumb are given in Table 6.4. From these results it is obvious that the

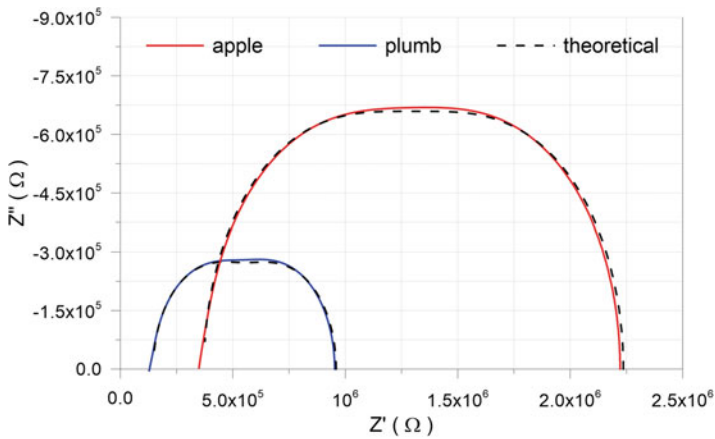


Fig. 6.16 Post-layout Nyquist impedance plots of the two emulated Cole-impedances

Table 6.4 Cole-impedance parameters extracted from an apple and plumb

Performance factors	Apple		Plumb	
	Simulation	Theoretical	Simulation	Theoretical
$Z'_{\min} (\Omega)$	391 k	372 k	127.9 k	147.9 k
$Z'_{\max} (\Omega)$	2.15 M	2.236 M	952.7 k	959.2 k
$Z''_{\min} (\Omega)$	-669.1 k	-659.1 k	-281.1 k	-274.5 k
$f@Z''_{\min} (Hz)$	2384	2329	2970	2344

proposed design is in a very good agreement within the frequency range that the fractional-order capacitor approximation offers a good performance.

Summarizing, the proposed emulation of the Cole-impedance based on the OTA topology is very good at capturing this behavior. This emulation scheme can be used to emulate the behavior of biological tissues with potential applications for self-test or emulated systems for bioimpedance measurements.

6.4 Simple Non-impedance-Based Measuring Technique for Supercapacitors

Supercapacitors are electrical devices which are used to store energy and offer high power density that is not possible to achieve with traditional capacitors. Thus, they bridge the gap between electrolytic capacitors and rechargeable batteries.

Nowadays, supercapacitors have many industrial applications and are used wherever a high current in a short time is needed. They are able to store or yield a lot of energy in a short period of time. According to IEC standard 62391-1 four

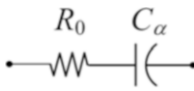
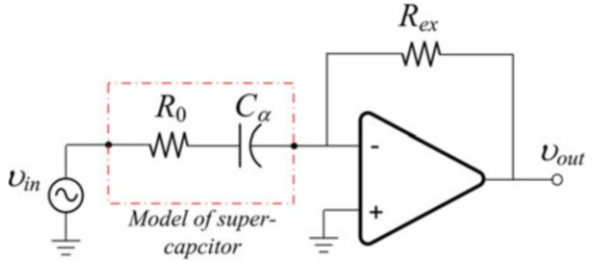


Fig. 6.17 Model representing the impedance of a supercapacitor

Fig. 6.18 Proposed topology for extracting parameters of a supercapacitor using R_0 - C_α model



application classes for supercapacitors are identified depending on their charge capacitance and time response: (i) memory backup, (ii) energy storage, (iii) power applications in propulsion systems, and (iv) pulse/instantaneous power. These power sources can be found in diverse technological domains ranging from energy storage for wind turbines [28] and other renewable energy sources [29], hybrid and electric vehicles [30], biomedical sensors [31] to wireless sensor nodes [32]. The typical working frequency range of supercapacitors varies from a fraction of 1 Hz to 1 kHz [33].

In terms of modeling, the impedance measurement of supercapacitors usually shows a frequency-dependent behavior that cannot be described by usual electric components. It is rather explained by a capacitance-dispersion phenomenon due to distributed surface reactivity, inhomogeneity, fractal/rough geometry, and porosity in terms of a CPE. Among the different models used to for supercapacitor characterization [34, 35], the simplest and most widely used is that shown in Fig. 6.17. The total impedance of the model is given by (6.18).

Standard LCR meters, which are designed with the assumption that $\alpha = 1$, are commonly used to measure capacitance. However, some supercapacitors exhibit appreciable deviation from ideality with the increased frequency [36]. This indicates that it would be incorrect to assume a behavior that is typical of a normal capacitor when measuring the electric properties of a supercapacitor. Furthermore, in some supercapacitors, (C_α, α) show a frequency-dependent behavior with their respective values significantly changing from near DC frequency (mHz range) to low-frequency range (Hz range) to medium frequency range (kHz range). A suitable topology that has been proposed in order to characterize the electric parameters of a supercapacitor R_0 - C_α is that given in Fig. 6.18. The resulted transfer function is given by (6.19) as

$$Z(s) = R_0 + \frac{1}{C_\alpha \cdot s^\alpha} \quad (6.18)$$

$$H(s) = -\frac{R_{ex}}{R_0} \cdot \frac{\omega_o^\alpha}{s^\alpha + \omega_o^\alpha} \quad (6.19)$$

where R_{ex}/R_0 is the high-frequency gain, and ω_o is the pole frequency given by

$$\omega_o = \frac{1}{(R_0 C_\alpha)^{1/\alpha}} \quad (6.20)$$

The magnitude response and phase response are given by (6.21).

$$|H(j\omega)| = \frac{(R_{ex}/R_0) \cdot \omega^\alpha}{\sqrt{\left(\frac{\omega}{\omega_o}\right)^{2\alpha} + 2\left(\frac{\omega}{\omega_o}\right)^\alpha \cos\left(\frac{\alpha\pi}{2}\right) + 1}} \quad (6.21)$$

$$\angle H(j\omega) = \pi + \alpha\pi/2 - \tan^{-1} \left(\frac{\left(\frac{\omega}{\omega_o}\right)^\alpha \sin\left(\frac{\alpha\pi}{2}\right)}{\left(\frac{\omega}{\omega_o}\right)^\alpha \cos\left(\frac{\alpha\pi}{2}\right) + 1} \right) \quad (6.22)$$

The resulted transfer function corresponds also to a fractional-order high-pass filter whose half-power frequency to pole frequency ratio is that in (6.23a), while the corresponding phase at this frequency is that given in (6.23b)

$$\omega_h = \omega_o \left[\sqrt{1 + \cos^2\left(\frac{\alpha\pi}{2}\right)} + \cos\left(\frac{\alpha\pi}{2}\right) \right]^{1/\alpha} \quad (6.23a)$$

$$\angle |H(j\omega)|_{\omega=\omega_h} = \pi + \alpha\pi/2 - \tan^{-1} \left(\frac{\sin\left(\frac{\alpha\pi}{2}\right)}{2 \cos\left(\frac{\alpha\pi}{2}\right) + \sqrt{1 + \cos^2\left(\frac{\alpha\pi}{2}\right)}} \right) \quad (6.23b)$$

The procedure that can be followed in order to measure the characteristics of a supercapacitor is the following:

1. Assuming that a typical value for R_0 is [5–100Ω], a reasonable choice is 500Ω. Thus, applying an input voltage 50 mV and monitoring output voltage while frequency is gradually increased, then, and noting that then the value R_0 could be calculated using (6.24), and the fact that the high frequency gain is R_{ex}/R_0

$$R_0 = R_{ex} \frac{|V_{in}|}{|V_{out}|_{\max}} \quad (6.24)$$

where $|V_{in}| = 50$ mV, and $|V_{out}|_{\max}$ is the stabilized maximum value of output voltage at a high-frequency value. The voltage power supply for the op amp is set equal to ± 9 V.

2. Taking into account that the phase angle between input and output (high-pass nature of setup) at very low frequencies is $\pi + (\alpha\pi/2)$, the order α could be easily determined.
3. In addition, the pole frequency can be calculated, by measuring the frequency (ω_h) at which there is 0.707 drop of the maximum output gain, i.e., $V_{\text{out}} = V_{\text{outmax}}/\sqrt{2}$, and then using (6.23a). Finally, the value of the pseudo-capacitance is calculated using (6.20).

A commercial NEC/TOKIN 5.5 V supercapacitor rated as 1 F (part# FGR0H105ZF) was selected for testing. The datasheet indicates that the nominal capacitance when charging is 1F and it is 1.3F when discharging; both measured at frequency very close to DC. Characterization of the electrical properties of the supercapacitor were carried out using

1. Standard precision LCR meters (Tisley LCR-6401 data-bridge and Thurlby Thandar Inst. LCR-400).
2. A Biologic VSP-300 electrochemical workstation equipped with an impedance analyzer operating in the 10 μHz to 7 MHz frequency range. With this instrument the supercapacitor parameters were investigated using both potentiostatic electrochemical impedance spectroscopy (PEIS) and galvanostatic electrochemical impedance spectroscopy (GEIS) in the two frequency ranges: (1 kHz–10 Hz) and (100–2.5 mHz) each with 10 points per decade. A least-square fitting algorithm was used in order to estimate (R_0 , C_α).
3. The proposed topology given in Fig. 6.18.

The utilization of the first way resulted into measuring a capacitance of 5476 μF and 730 μF respectively at 100 Hz and 1 kHz. The series resistance was $R_0 = 6 \Omega$ in both cases. Thus, the values of measured capacitances are totally different from the rated value of 1F.

Impedance spectroscopy measurements using the electrochemical station in the frequency range (1 kHz–10 Hz) (100–2.5 mHz) are shown in Fig. 6.19a and Fig. 6.19b, respectively. Using the aforementioned fitting algorithm, the obtained values of parameters (R_0 , C , α) in the frequency range (1 kHz–10 Hz) was (7.6 Ω , 0.214F/sec $^{1-\alpha}$, 0.29) and (7.7 Ω , 0.2 F/sec $^{1-\alpha}$, 0.33) using GEIS and PEIS, respectively. Also, in the frequency range (100–2.5 mHz) was (15.6 Ω , 0.533F/sec $^{1-\alpha}$, 0.90). As a result, it is obvious that C_α is far away from the rated value in low and medium frequencies, making this type of measurement unreliable for characterizing supercapacitors. Inspecting Fig. 6.19b, it is evident that only very close to DC can a circuit designer rely on the datasheet values of a supercapacitor. In the practical range for most circuit design applications, the supercapacitor is far from being an ideal capacitor with as low as 0.3 from GEIS measurements. Therefore, a circuit designer needs a simple test circuit, like the one proposed here in Fig. 6.18, to extract practical supercapacitor parameters at his targeted application frequency.

Applying a 50mVpp input signal, and increasing the frequency until output voltage stabilizes at a maximum value, the high frequency gain is achieved at approximately 60 Hz. Thus, the output voltage was measured 3.74 V as shown in Fig. 6.20a. As a result, the value of R_0 was calculated using (6.24), and knowing that

Fig. 6.19 Nyquist plots in the frequency ranges (a) 1 kHz to 10 Hz and (b) 100–2.5 mHz of supercapacitor

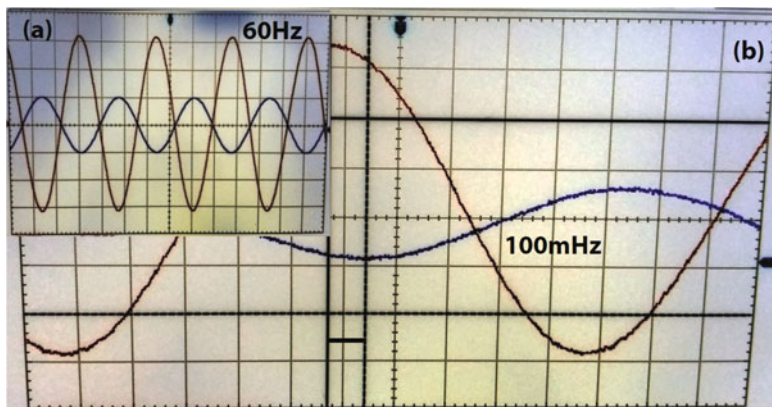
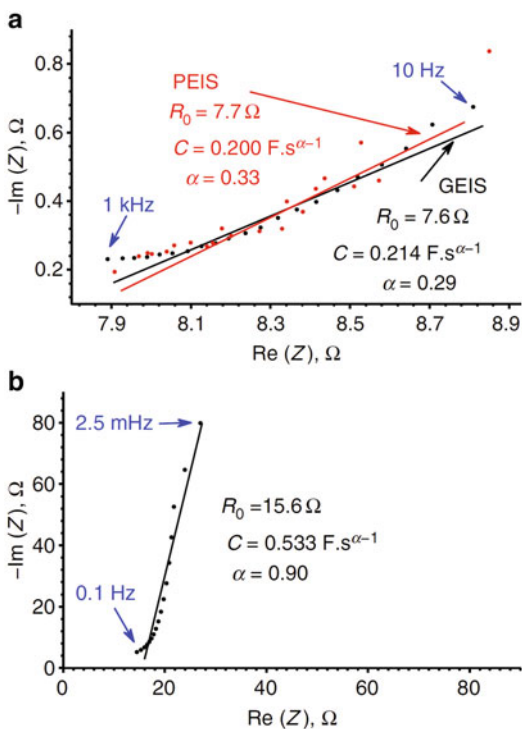


Fig. 6.20 Experimental observation from the setup in Fig. 6.18 at (a) 60 Hz, (b) 100 mHz

R_{ex} was selected as 500Ω , 6.7Ω . The obtained value is very close to that measured using EIS. The source frequency was then reduced until $V_{\text{out}} = 2.65 \text{ V}$, which corresponds to the half-power frequency and occurred at 1 Hz. Finally, the source frequency was reduced to 100 mHz as shown in Fig. 6.20b.

The value of order was calculated $\alpha \approx 0.3$, by measuring the phase difference between V_{in} and $-V_{out}$. The obtained value is very close to that given by EIS data. A second measuring of phase difference was made at 30 mHz, which yielded $\alpha \approx 0.29$. Therefore, using (6.23a) the pole frequency is calculated to be $f_o \approx 0.0935$ Hz, while using (6.20) the capacitance value is found to be $C \approx 0.174$ F/sec $^{1-\alpha}$; close enough to the value given by EIS (0.200 and 0.214 using PEIS and GEIS, respectively).

Concluding, the electric characterization of a commercial supercapacitor, assumed to behave as R_0 - C_α equivalent circuit is performed using LCR meters, EIS, and a simple nonimpedance-based technique using an op amp. In the frequency range of interest for supercapacitor applications (1 Hz–1 kHz), LCR results show a large deviation from the actual EIS data, as the former is not designed to take into account the frequency-dispersion capacitance of the device. Although in the DC range data from both measuring devices converge, it is not of practical interest to a circuit designer. Thus, instead of using an LCR meter or an expensive EIS workstation, a very simple electric circuit using an op amp can be made successfully extract the (R_0, C_α, α) parameters with minimum computational effort and good level of accuracy.

6.5 Design and Evaluation of a Fractional-Order Oscillator

Fractional-order oscillators were first introduced in [37] where a classical Wien-bridge oscillator was studied when its two ideal capacitors are replaced by two identical fractional-order capacitors characterized by

$$i(t) = C_\alpha \frac{d^\alpha v(t)}{dt^\alpha} \quad (6.25)$$

where α is known as the dispersion coefficient or the order of the fractional capacitor ($0 \leq \alpha \leq 1$) and C_α is the pseudo-capacitance in units of F/sec $^{1-\alpha}$.

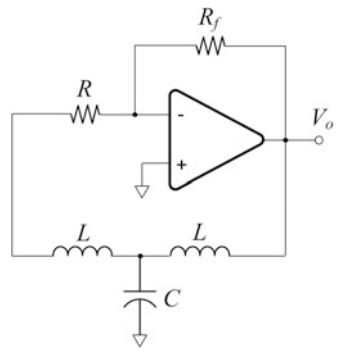
On the other hand, fractional-order inductors are characterized by the current-voltage relationship [38] given in (6.26)

$$v(t) = L_\beta \frac{d^\beta i(t)}{dt^\beta} \quad (6.26)$$

where β is the order of the inductor ($0 \leq \beta \leq 1$) and L_β is the pseudo-inductance in units of H/sec $^{1-\beta}$.

A fractional-order inductor can be realized from a fractional-order capacitor and generalized impedance converter setup [39]. An oscillator with fractional-order inductors has not been experimentally verified before, although such an oscillator was studied for example in [40]. Thus, the derivative of the classical Hartley oscillator relying on a T – Network composed of a grounded capacitor and two

Fig. 6.21 Hartley oscillator with an operational amplifier



inductors in three different cases is studied in detail. Firstly, the ideal capacitor is substituted with a fractional-order capacitor. In the next, ideal inductors are replaced with the corresponding fractional-order counterparts. The characteristic equation describing the oscillator is different in each case and as a consequence the oscillation frequency, too. Considering the oscillator circuit in Fig. 6.21, and assuming that the two inductors are similar with inductance L and internal parasitic resistance r , the characteristic equation of this oscillator will be given as

$$s^3 + as^2 + bs + c = 0 \quad (6.27)$$

where

$$\begin{aligned} a &= \frac{2r + R}{L} \\ b &= \frac{2}{LC} + \left(\frac{r}{L}\right)^2 + \frac{rR}{L^2} \\ c &= \frac{2r + R + R_f}{L^2C} \end{aligned} \quad (6.28)$$

Assuming that the oscillation start-up (marginal stability) condition is $ab = c$ then

$$R_f = 2r + R + \frac{rC}{L}(r + R)(2r + R) \quad (6.29)$$

Where in case that $R \gg r$, this condition becomes

$$k = \frac{R_f}{R} = 1 + \frac{rC}{L}R \quad (6.30)$$

For ideal inductors with $r \rightarrow 0$, the ideal start-up condition is $R_f = R$; that is, the op amp is operating as a unity gain inverting amplifier with $k = 1$. The oscillation frequency is then

$$\omega_o = \sqrt{\frac{2}{LC} + \frac{r^2 + rR}{L^2}} = \frac{\sqrt{2}}{\sqrt{LC}} \Big|_{r \rightarrow 0} \quad (6.31)$$

Now consider replacing the ideal capacitor C with a fractional-order whose impedance is $Z = 1/(j\omega)^\alpha C_\alpha$. The characteristic equation in this case becomes

$$s^{(2+\alpha)} + as^{(1+\alpha)} + bs + cs^\alpha + d = 0 \quad (6.32)$$

where

$$\begin{aligned} a &= \frac{2r + R}{L}, b = \frac{2}{LC_\alpha} \\ c &= \frac{r^2 + rR}{L^2}, d = \frac{2r + R + R_f}{L^2 C_\alpha} \end{aligned} \quad (6.33)$$

For simplicity, we consider the case of half-order capacitor with $\alpha = 0.5$. Noting that in this case

$$(j\omega)^\alpha = \omega^\alpha \left[\cos\left(\frac{\alpha\pi}{2}\right) + j \sin\left(\frac{\alpha\pi}{2}\right) \right] = \frac{\sqrt{\omega}}{\sqrt{2}} (1 + j) \Big|_{\alpha=0.5} \quad (6.34)$$

the oscillation start-up condition can be obtained by solving for R_f the Eq. (6.35) obtained by equating the real part of (6.32) to zero after substituting for $s^{0.5}$ from (6.34).

$$\omega^{2.5} + a\omega^{1.5} - c\omega^{0.5} - \sqrt{2}d = 0 \quad (6.35)$$

For ideal inductors with $r \rightarrow 0$ ($c \rightarrow 0$) the oscillation start-up condition becomes

$$k + 1 = \frac{L^2 C_{0.5}}{\sqrt{2}} \omega_o^{2.5} + \frac{LC_{0.5}}{\sqrt{2}} \omega_o^{1.5} \quad (6.36)$$

where ω_o is the oscillation frequency obtained as the solution to (6.37), which for $c \rightarrow 0$ simplifies to (6.38)

$$\omega_o^2 - a\omega_o - \sqrt{2}b\omega_o^{0.5} - c = 0 \quad (6.37)$$

$$\omega_o^{1.5} - \frac{R}{L}\omega_o^{0.5} - \frac{2\sqrt{2}}{LC_{0.5}} = 0 \quad (6.38)$$

Next we consider the case when one of the two inductors is fractional-order with impedance $Z = L_\beta (j\omega)^\beta$ while the other inductor remains to be an ideal inductor with impedance $Z = j\omega L$. Hence, assuming the capacitor is integer-order with impedance $Z_C = 1/j\omega C$, there are two possible cases depending on which inductor

is fractional order. The characteristic equations in the two cases are given by (6.39) and (6.40), respectively for a right-hand and a left-hand fractional inductor (see Fig. 6.21).

$$s^{(2+\beta)} + \frac{R}{L}s^{(1+\beta)} + \frac{1}{LC}s^\beta + \frac{1}{L_\beta C}s + \frac{R + R_f}{LL_\beta C} = 0 \quad (6.39)$$

$$s^{(2+\beta)} + \frac{R}{L_\beta}s^2 + \frac{1}{LC}s^\beta + \frac{1}{L_\beta C}s + \frac{R + R_f}{LL_\beta C} = 0 \quad (6.40)$$

For the case of half-order inductor ($\beta = 0.5$), we obtain the start-up condition as shown in (6.41) and (6.42), respectively for the two cases

$$k + 1 = \frac{L_{0.5}}{\sqrt{2}R}\omega_o^{0.5}(LC\omega_o^2 + RC\omega_o - 1) \quad (6.41)$$

$$k + 1 = \frac{L_{0.5}}{\sqrt{2}R}\omega_o^{0.5}\left(LC\omega_o^2 + \frac{\sqrt{2}RLC}{L_{0.5}}\omega_o^{1.5} - 1\right) \quad (6.42)$$

where ω_o is the oscillation frequency obtained as the solution to that given in (6.43) or (6.44), respectively.

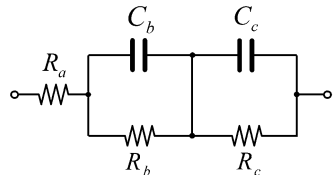
$$\omega_o^2 - \frac{R}{L}\omega_o - \frac{\sqrt{2}}{L_{0.5}C}\omega_o^{0.5} - \frac{1}{LC} = 0 \quad (6.43)$$

$$\omega_o^2 - \frac{\sqrt{2}}{L_{0.5}C}\omega_o^{0.5} - \frac{1}{LC} = 0 \quad (6.44)$$

The oscillation frequency was fixed 1 kHz in order to test all three cases. Also, the two inductors were fixed at $L = 800$ mH, and the fractional-order capacitor was emulated using the second-order network shown in Fig. 6.22 with $R_a = 160 \Omega$, $R_b = 485 \Omega$, $R_c = 3.3$ k Ω , $C_b = 173$ nF, and $C_c = 450$ nF for approximating $C_{0.5} \approx 16 \mu\text{F}/\text{sec}^{0.5}$ (i.e., $0.2 \mu\text{F}$ at f_o). Using (6.38) and (6.36) then $R = 2.8$ k Ω and $k \approx 11.4$. The observed oscillatory waveform is shown in Fig. 6.23a where the measured frequency was 0.93 kHz, which is very close to the targeted value of 1 kHz.

Firstly the right-hand inductor is fixed as 800 mH and fix $R = 1$ k Ω . Then, the fractional-order left-hand inductor value was selected $L_{0.5} = 63.4$ H/ $\text{sec}^{0.5}$ (equivalent approximately to 800 mH at the desired oscillation frequency). Solving (6.44)

Fig. 6.22 Second-order approximation of a fractional-order capacitor using RC network



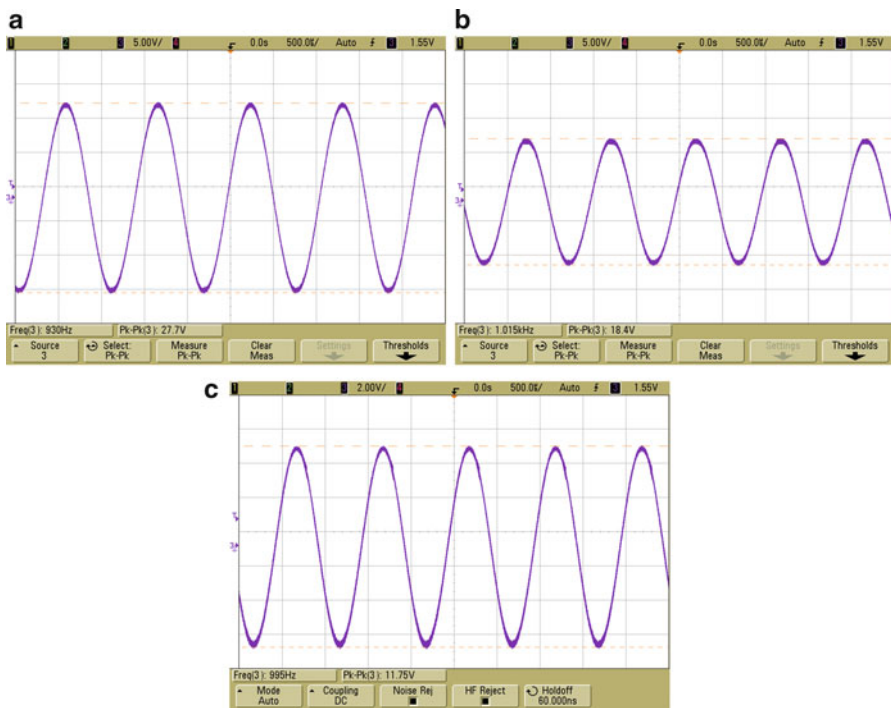


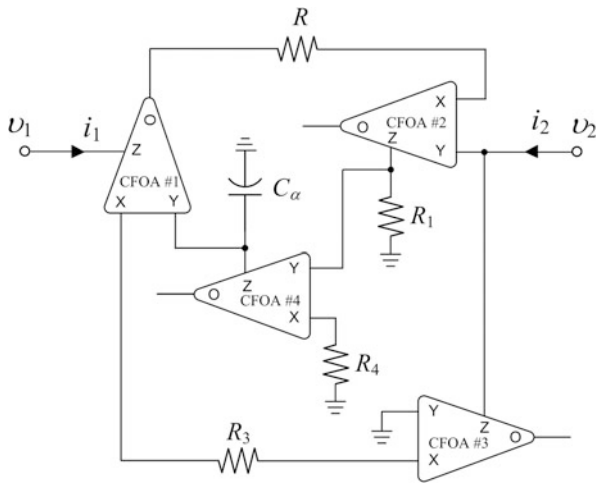
Fig. 6.23 Experimentally observed oscillations with $f_o = 1$ kHz, in the case of (a) fractional-order capacitor, (b) fractional-order left-hand inductor, and (c) fractional-order right-hand inductor

then yields $C = 76.5$ nF and then solving (6.42) results in $k = 6.4$. The floating fractional-order is realized by inserting a fractional-order capacitor $C_{0.5}$ in a GIC circuit realized using 4 CFOAs (AD844 chips), as shown in Fig. 6.24 and an equivalent impedance [41] given by (6.45) with all resistors equal to $10\text{k}\Omega$.

$$Z_{eq} = \frac{R_2 R_3 R_4}{R_1} C_{0.5} s^{0.5} \quad (6.45)$$

In order to obtain the desired value for $L_{0.5}$, the component values of the emulator in Fig. 6.22 are changed to $R_a = 4$ k Ω , $R_b = 12.2$ k Ω , $R_c = 83.3$ k Ω , $C_b = 6.9$ nF, and $C_c = 18$ nF. The observed sinusoidal waveform in this case is shown in Fig. 6.23b with a measured oscillation frequency of 1.01 kHz again very close to the designed value. Finally, the case where the right-hand inductor is fractional ($L_{0.5} = 63.4$ H/sec $^{0.5}$) and the left-hand inductor is fixed ($L = 800$ mH) was also tested having $R = 1$ k Ω and then using (6.43) to calculate $C = 95.4$ nF and (6.41) to obtain $k = 8.3$. Note that despite the fact that all fixed components have the same values as for the case of the left-hand fractional inductor, the necessary start-

Fig. 6.24 Realization of the floating fractional-order inductor using a fractional-order capacitor inside a GIC circuit



up gain here is higher and so is the needed value of C . The observed waveform in this case is shown in Fig. 6.23c with a measured oscillation frequency of 0.995 kHz.

Fractional-order oscillators have a unique advantage when compared to their integer-order counterparts. That is the capability of producing higher frequencies for the same inductance and capacitance values as a result of the existence of one or more fractional-order differential equations. This is clear in the Hartley oscillator studied here where in the integer-order case and assuming $L = 800$ mH and $C = 0.2$ μ F, (6.31) predicts the oscillation frequency of 563 Hz with a start-up gain $k = 1$. However, with a half-order fractional capacitor $C_{0.5} \approx 16$ μ F/sec^{0.5} having an equivalent capacitance of 0.2 μ F @ 1 kHz, the oscillator produced a waveform of twice the frequency approximately, that is, 1 kHz. Also, with a half-order inductor $L_{0.5} = 63.4$ H/sec^{0.5} (left-hand or right-hand) having an equivalent inductance of 800 mH @ 1 kHz, the same higher oscillation frequency was achieved. Of course, the boot in frequency will be significantly appreciated in the MHz or GHz frequency ranges if fractional-order capacitors or inductors operating at these frequencies become available. The cost, however, that has to be paid for achieving higher oscillation frequencies with fractional-order devices is in the start-up gain k . This is clear in the current study where for the integer-order oscillator $k = 1$, while it is $k = 11.4$ when C is replaced by $C_{0.5}$ and it is $k = 6.4$ and $k = 8.3$ respectively when L is replaced with $L_{0.5}$ in the left-hand and right-hand positions of the T - network.

Summarizing, a fractional-order Hartley oscillator has been studied and experimentally verified. The employment of fractional-order devices in the oscillator requires knowledge of the targeted oscillation frequency in order to identify which device from the original integer-order oscillator is better to replace.

References

1. Tsividis, Y.: Externally linear, time-invariant systems and their applications to companding signal processors. *IEEE Trans. Circ. Syst. II.* **44**(2), 65–85 (1997)
2. Frey, D.R.: Log-domain filtering: an approach to current-mode filtering. *IET Proc. Circ Dev. Syst. Pt.-G.* **140**(6), 406–416 (1996)
3. Serdijn, W., Kouwenhoven, M., Mulder, J., van Roermund, A.: Design of high dynamic range fully integratable translinear filters. *Analog Integr. Circ. Sig. Proc.* **19**(3), 223–239 (1999)
4. Katsiamis, A., Glaros, K., Drakakis, E.: Insights and advances on the design of CMOS sinh companding filters. *IEEE Trans. Circ. Syst. I.* **55**(9), 2539–2550 (2008)
5. Psychalinos, C.: Low-voltage complex log-domain filters. *IEEE Trans. Circ. Syst. I.* **55**(11), 3404–3412 (2008)
6. Psychalinos, C.: Log-domain SIMO and MISO low-voltage universal Biquads. *Analog Integr. Circ. Sig. Proc.* **67**(2), 201–211 (2011)
7. Kasimis, C., Psychalinos, C.: Design of Sinh-Domain filters using complementary operators. *Int. J. Circ. Theory Appl.* **40**(10), 1019–1039 (2012)
8. Kasimis, C., Psychalinos, C.: 1.2V BiCMOS Sinh-Domain filters. *Circ. Syst. Sig. Proc.* **31**(4), 1257–1277 (2012)
9. Mulder, J., Serdijn, W.A., van der Woerd, A.C., van Roermund, A.H.M.: “A syllabic companding translinear Filter”, *Proc. in IEEE International Symposium Circuits Systems (ISCAS), Hong Kong*, pp. 101–104 (1997)
10. Adams, R.W.: “Filtering in the log domain”, Preprint #1470, 63rd AES Conference, New York (1979)
11. Tsirimokou, G., Laoudias, C., Psychalinos C.: 0.5-V fractional-order companding filters. *Int. J. Circ. Theory Appl.* **43**(9), 1105–1126 (2015)
12. Tsirimokou, G., Laoudias, C., Psychalinos, C.: Tinnitus detector realization using sinh-domain circuits. *J. Low Power Electron.* **9**(4), 458–470 (2013)
13. Kafe, F., Psychalinos, C.: Realization of companding filters with large time-constants for biomedical applications. *Analog Integr. Circ. Sig. Process.* **78**(1), 217–231 (2014)
14. Pan, J., Tompkins, W.: A real-time QRS detection algorithm. *I.E.E.E. Trans. Biomed. Eng.* **32**(3), 230–236 (1985)
15. Hamilton, P., Tompkins, W.: Quantitative investigation of QRS detection rules using the MIT/BIH arrhythmia database. *IEEE Trans. Biomed. Eng.* **33**(12), 1157–1165 (1986)
16. Bailey, J., Berson, A., Garson, A., Horan, L., Macfarlane, P., Mortara, D., et al.: Recommendations for standardization and specifications in automated electrocardiography: bandwidth and digital signal processing. *J. Am. Heart Assoc. Circ.* **81**, 730–739 (1990)
17. Kligfield, P., Gettes, L., Bailey, J., Childers, R., Deal, B., Hancock, W., et al.: Recommendations for the standardization and interpretation of the electrocardiogram part I: the electrocardiogram and its technology. *Journal of the American Heart Association Circulation.* **115**, 1306–1324 (2007)
18. Ferdi, Y., Hebeuval, J., Charef, A., Boucheham, B.: R wave detection using fractional digital differentiation. *ITBMRBM.* **24**(5-6), 273–280 (2003)
19. Goutas, A., Ferdi, Y., Herbeuval, J.P., Boudraa, M., Boucheham, B.: Digital fractional order differentiation-based algorithm for P and T-waves detection and delineation. *Int. Arab. J. Inf. Technol.* **26**(2), 127–132 (2005)
20. Benmalek, M., Charef, A.: Digital fractional order operators for R-wave detection in electrocardiogram signal. *IET Sig. Process.* **3**(5), 381–391 (2009)
21. Sawigun, C., Serdijn, W.: Ultra-low-power, class-AB. CMOS four-quadrant current multiplier. *Electron. Lett.* **45**(10), 483–484 (2009)
22. Kasimis, C., Psychalinos, C.: 0.65 V class-AB current-mode four-quadrant multiplier with reduced power dissipation. *Int. J. Electron. Commun.* **65**(7), 673–677 (2011)
23. Tsirimokou, G., Psychalinos, C., Khanday, F.A., Shah N.A.: 0.5V Sinh-Domain Differentiator. *Int. J. Electron. Lett.* **3**(1), 34–44 (2015)

24. <http://www.physionet.org/physiotools/ecgsyn/>. Accessed 25 Aug 2014
25. Cole, K.S.: Permeability and impermeability of cell membranes for ions. *Proc. Cold Spring Harb. Lab. Symp. Quant. Biol.* **8**, 110–122 (1940)
26. Freeborn, T.J.: A survey of fractional-order circuits models for biology and biomedicine. *IEEE J. Emerging Sel. Top. Circ. Syst.* **3**(3), 416–424 (2013)
27. Maundy, B., Elwakil, A.S.: Extracting single dispersion Cole-Cole impedance model parameters using an integrator setup. *Analog Int. Circ. Sig. Process.* **71**(1), 107–110 (2012)
28. Abbey, C., Joos, G.: Supercapacitor energy storage for wind energy applications. *IEEE Trans. Ind. Appl.* **43**(3), 769–776 (2007)
29. Pegueroles-Queralt, J., Bianchi, F.D., Gomis-Bellmunt, O.: A power smoothing system based on supercapacitors for renewable distributed generation. *IEEE Trans. Ind. Electron.* **62**(1), 343–350 (2015)
30. Cao, J., Emadi, A.: A new battery/ultracapacitor hybrid energy storage system for electric, hybrid, and plug-in hybrid electric vehicles. *IEEE Trans. Power Electron.* **27**(1), 122–132 (2012)
31. Pandey, A., Allos, F., Hu A.P., et al.: “Integration of supercapacitors into wirelessly charged biomedical sensors”, in *Proc. Of Sixth IEEE Conference on Industrial Electronics and Applications (ICIEA)*, pp. 56–61 (2011)
32. Kim, S., No, K.S., Chou, P.H.: Design and performance analysis of supercapacitor charging circuits for wireless sensor nodes. *IEEE J. Emerging Sel. Top. Circ. Syst.* **1**(3), 391–402 (2011)
33. Du, C., Pan, N.: High power density supercapacitor electrodes of carbon nanotube films by electrophoretic deposition. *Nanotechnology.* **17**(21), 5314 (2006)
34. Mahon, P.J., Paul, G.L., Keshishian, S.M., Vassallo, A.M.: Measurement and modeling of the higher-power performance of carbon-based supercapacitors. *J. Power Sources.* **91**(1), 68–76 (2000)
35. Martynyuk, V., Ortigueira, M.: Fractional model of an electrochemical capacitor. *Signal Process.* **107**(2), 355–360 (2015)
36. Bondarenko, A., Ragoisha, G.: “Progress in Chemometrics Research” (Nova Science, New York, (<http://www.abc.chemistry.bsu.by/vi/>), 2005)
37. Ahmed, W., Elkhazali, R., Elwakil, A.S.: Fractional-order Wienbridge oscillator. *Electron. Lett.* **37**, 1110–1112 (2001)
38. Radwan, A., Salama, K.: Fractional-order RC and RL circuits. *Circuits, Systems and Signal Processing Journal.* **31**(6), 1901–1915 (2012)
39. Freeborn, T.J., Maundy, B.J., Elwakil, A.S.: Fractional resonance based filters. *Math. Probl. Eng.* **726721**, 1–10 (2013)
40. Radwan, A.G., Elwakil, A.S., Soliman, A.M.: Fractional-order sinusoidal oscillators: design procedure and practical examples. *IEEE Trans. Circ. Syst. I.* **55**, 2051–2063 (2008)
41. Pychalinos, C., Pal, K., Vlassis, S.: A floating generalized impedance converter with current feedback amplifiers. *Int. J. Electron. Commun. (AEU).* **62**, 81–85 (2008)

Chapter 7

Conclusions and Motivation for Future Work

7.1 Conclusions

Throughout this work the second-order approximation of the CFE is utilized in order to present a systematic way for describing the design equations of fractional-order generalized transfer functions. Thus, fractional-order transfer functions are approximated using integer-order transfer functions, which are easy to realize. The main active cells that are employed are current mirrors, nonlinear transconductance cells (known as S , C cells), and OTAs, which are very attractive building blocks offering the capability of implementing resistorless realizations with electronic tuning, where only grounded capacitors are employed. As a result, the designer has only to choose the appropriate values of DC bias currents in order to realize the desired transfer function. Taking into account that MOS transistors are biased in subthreshold region, these topologies are able to operate in a low-voltage environment with reduced power consumption, making them attractive candidates when they are utilized in biomedical applications.

Consequently, the following analog integrated implementations are realized:

- Fully integratable fractional-order differentiator/integrator topologies, as well as fractional-order generalized filters (i.e., low-pass, high-pass, bandpass), are designed, which are able to be realized using the same topology, while the frequency characteristics as well as the fractional-order (α) are capable to be easily electronically tuned, offering design flexibility and programmability.
- Fully integrated fractional-order (capacitor and inductor) emulators, offering the capability of electronic tuning of impedance magnitude, fractional order, and the bandwidth of operation. The proposed designs are fabricated in AMS 0.35 μm C35B4C3 CMOS technology the efficiency of which has been verified through experimental results. As design examples, the performance of an $L_\beta C_\alpha$ parallel resonator, as well as a fractional bandpass filter of order $\alpha + \beta$, is presented,

which proves that the fabricated designs offer attractive benefits and are able to be utilized in high performance systems.

- Also, some interesting applications of the aforementioned designs are presented. Firstly, a fractional-order differentiator is utilized in the Pan-Tompkins algorithm, in order to prove that fractional-order topologies are capable for handling ECG signals in a noisy environment. As a second example, a fully tunable biological tissue model is realized using appropriate fractional-order topologies (Cole-Cole model). The correct operation of the aforementioned applications has been verified through simulation and comparison results using the Analog Design Environment of the Cadence software. In addition, a very simple circuit topology is introduced for characterizing fractional-order elements. The proposed topology uses operational amplifiers, which are easy to find, and hence there is not required expensive equipment as in the corresponding already published solutions. The aforementioned setup is utilized in order to characterize a supercapacitor, where experimental results are obtained affirming the utility of the proposed circuit. Finally a fractional-order oscillator is realized using fractional-order elements. The topology that has been used in order to evaluate the efficiency of the oscillator is the already known Hartley oscillator, where the integer-order elements are substituted with fractional-order parts. The main attractive benefit that is offered is the achievement of higher-order frequencies for the same values of capacitances and inductances, which is very important for performing high performance analog circuit designs.

7.2 Motivation for Future Work

Taking into account that the utilization of the second-order approximation offers a limited bandwidth of operation, higher-order approximation of the variable $(\tau s)^\alpha$ could be utilized in order to achieve more efficient designs. In addition, other types of approximation methods could be studied, especially when the order of approximation is increased. For example, the utilization of Oustaloup method could be an alternative solution for this purpose.

Fractional-order capacitor and inductor emulators are as already mentioned the most important circuits in this field, and as a consequence other approaches could be realized. More efficient building blocks could be utilized in order to increase the quality of these emulators. In addition, CPEs and FOIs which are able to operate in a higher voltage environment are circuits that should be designed especially in case that they are going to be combined with circuits that operate in a high voltage environment. The proposed topologies could be realized in the sense that the frequency characteristics, as well as the fractional-order, are digitally programmed and the resulted designs are fully integrated. Nevertheless, the already designed fractional-order elements could be also used in several applications such as energy where supercapacitors are widely used, in control systems (PID controllers), and in modeling of different types of biological tissues.